ANSTO/E697

ANSTO/E697

ANSTO

PARTICLE INDUCED X-RAY EMISSION

by

DAVID D. COHEN

AUGUST 1991

REPORT E

ISBN 642 59912 2
ISSN 1030-7745

AUSTRALIAN NUCLEAR SCIENCE AND TECHNOLOGY ORGANISATION

LUCAS HEIGHTS RESEARCH LABORATORIES

ANSTO-E-697

PARTICLE INDUCED X-RAY EMISSION

BY

DAVID D COHEN

ABSTRACT

The accelerator based ion beam technique of Particle Induced X-ray Emission (PIXE) is discussed in some detail. This report pulls together all major reviews and references over the last ten years and reports on PIXE setups, applications, sensitivities, artifacts and costing.

National Library of Australia card number and ISBN 0 642 59912 2

The following descriptions have been selected from the INIS Thesaurus to describe the subject content of this report for information retrieval purposes. For further details please refer to IAEA-INIS-12 (INIS: Manual for Indexing) and IAEA-INIS-13 (INIS: Thesaurus) published in Vienna by the International Atomic Energy Agency.

Accelerators; Ansto; efficiency; emission; filter; ion beam; particle induced; interactions; PIXE; photons; protons; sensitivity; Si(Li) detectors; spectrum; technique; vacuum; Van de Graaff; X-rays; X-ray energy; X-ray yield.

EDITORIAL NOTE

The Australian Nuclear Science and Technology Organisation replaced the Australian Atomic Energy Commission on 27 April 1987. Reports issued after April 1987 have the prefix Ansto with no change of the symbol (E, M, S or C) or numbering sequence.

CONTENTS

1. INTRODUCTION

Particle Induced X-ray Emission or PIXE became popular in the mid 1970's following an excellent review on the analytical applications of PIXE by Johansson and Johansson [1]. As early as 1970 it had been demonstrated by Johansson et al [2] that a combination of X-ray excitation by protons and detection by a Si(Li) detector was a powerful multielemental surface analysis method of high sensitivity. It was not until the advent of the commercial Si(Li) detector late in the 1970's and early 1980's that the PIXE explosion took off. PIXE now has a world wide following with many small accelerator laboratories operating their own analytical facilities. There are currently over 100 laboratories in more than 30 different countries throughout the world operating PIXE systems. These tend to be on accelerators with terminal voltages between 1 and 5 MV (2 to 3 MV most popular) using mainly proton bombardment of a host of different target materials.

The very broad range of applications of the PIXE technique have been adequately summarised by the proceedings of 3 of the last 5 International Conferences on PIXE and its Analytical Applications [3-5]. They cover areas as diverse as aerosol pollution studies, mining, geological, archaeological, art and biomedical applications. The technique of using light ion beams from accelerators to induce X-rays characteristic of the surface being bombarded has been adequately reviewed over the years [6-10] and will not be treated in depth here.

The aim of this brief report is to bring together key references and data on PIXE and to discuss PIXE in vacuum and using external beams and to talk about the advantages, limitations, costs and types of studies that may be undertaken using an accelerator based ion beam technique such as PIXE.

2. ION BEAM INTERACTIONS

When a light ion such as a proton or helium ion from an accelerator interacts with an atom in the target material several reaction processes are possible. Some of these are shown in Fig. 1. Ion interactions with a target atom electron cloud produce ionisation (electron ejection) and subsequent photon emission. Nuclear interactions may scatter the incoming ion, produce gamma rays and/or other product particles. Ion interactions with several target atoms may break chemical bonds, produce light or UV, sputter atoms from the surface itself or, if the target has its own crystalline structure, even channel the incoming ion. The result of all these processes is the ion loses energy in the target material.

The PIXE technique utilizes the ion energy loss process of inner shell ionisation of the target atom. Electrons ejected from the K or L shell by the Coulomb interaction of the fast moving ion have their vacancies filled by other outer electron transitions into these shells and an X-ray photon is emitted to carry off the excess energy. The allowable X-ray transmissions for initial vacancies in the K and L shell of the target atom are shown in Fig. 2. Using the conventional Siegbahn notation these are generally referred to as Kalpha, Kbeta or Lalpha, Lbeta and Lgamma X-ray transitions depending in which shell the original vacancy occurred. Fig. 3 shows the typical X-ray energies for K, L and M shell X-rays versus target atomic number. Each target has a unique K,L or M X-ray signature and these X-ray energies fall into discreet bands, increasing monotonically with energy. For PIXE systems M X-rays are typically low energy (1-3 keV), L intermediate energy (1-20 keV) and K X-rays high energy (1-30 keV).

The X-ray signals produced by ion bombardment generate a unique fingerprint for that element. Figs. 4a and b show the K and L shell fingerprints of pure Cu and Pb targets respectively. These spectra were taken using a standard energy dispersive Si(Li) detector system discussed further below and they demonstrate the basic principle of the PIXE technique. That is the X-ray energy specifies the element present in the target and the number of X-rays produced specifies the amount of that element in the target. For targets containing several elements a detection system with sufficient resolution to detect each elemental signature is required.

A typical PIXE detection system may operate over the X-ray energy range 1-40 keV, and hence be capable of detecting K, L or M light X-rays. Fig. 5 is an X-ray spectrum obtained by the bombardment of 2.6 MeV protons onto a thin aerosol filter paper sample. It contains X-rays from many elements and several different X-ray bands. The filter paper sample had air drawn through it for several hours and the spectrum shows K X-rays for selected elements from Si to Br and L X-rays for Pb. This spectrum was acquired after just a few minutes of accelerator running time and shows X-ray peaks for a dozen different elements varying in height over 5 orders of magnitude. It represents elemental concentrations of a few percent by weight for Si to a few micrograms per gram for Cu and clearly demonstrates the power of the PIXE analytical technique. The increased background around 2 keV is secondary electron Bremsstrahlung background produced by deceleration of electrons generated by the ion in the target. This background falls by 2 orders of magnitude between 1 and 4 keV, being essentially zero above 8 keV. The lack of background in the X-ray region above several keV is the reason for the high sensitivity of PIXE compared to other X-ray analytical techniques.

3. PIXE SENSITIVITY

The diameter of a single atom is some 5 orders of magnitude larger than that of its nucleus and as such an ion flying past a target atom has a much higher probability of interacting with the target electrons than with its nucleus. The probability of ejecting an inner shell electron from a target atom depends on the energy of the incoming ion and how tightly that electron is bound to the target atom. The probability of ejection is called the ionisation cross section and is measured in barns (10^{-24} cm^2) and the electron binding energy U is measured in keV. Fig. 6 is a universal plot of this cross section times the binding energy squared versus the ion energy (MeV) normalised to the target atom binding energy. These theoretical cross sections were taken from Cohen and Harrigan [11] and the coefficients for the polynomial least squares fits to these are given in Cohen and Clayton [12] Table 1 for proton bombardment. The figure shows the higher probability of vacancy production for M than L than K shell with a broad peak around 1.5 MeV/keV dropping off very quickly for normalised ion energies below 0.1 MeV/keV. For K X-rays around Si U~ 2 keV and this peak corresponds to ion energies around 4 MeV. The physical interpretation of this peak in the cross section occurs where the velocity of the ion is comparable with the velocity of the inner shell electron being ejected. Hence this is called the velocity matching peak.

Cahill [13] shows that the ionisation cross sections are very sensitive to ion velocity and for 1-5 MeV protons scale as,

$$\sigma^I = f(Z_1^{\ 2}\ v_1^{\ 4}\ Z_2^{\ -12})$$

for ions of atomic number Z_1 and velocity v_1 on targets with atomic number Z_2. He points out that the rapid (Z_2^{-12}) dependence on Z_2 falls to about Z_2^{-6} for light elements. For a given target and for light ions the expression implies the cross section for ions heavier than protons scale as the square of the ion atomic number times the cross section for protons at the same value of (E/M). Hence helium ion cross sections are roughly 4 times proton cross sections at one quarter of the energy.

In practice the number of X-rays detected in a PIXE system is not only a function of the ionisation cross section but also of the X-ray detection efficiency. For energy dispersive systems based on Si(Li) detectors this efficiency tends to be low for X-rays below 5 keV and above 30 keV depending on the detector thickness. Fig. 7 shows the X-ray yield per millisteradian for 100 μC of protons (100 nA for 1000s) bombarding thick targets versus target atomic number for four proton energies up to 4 MeV.

The K shell X-rays cover the target atomic number range from 10 to 60 and the L shell from 50 to 90. For 4 MeV the K shell yield peak around 10^9 counts/100 μC/msr for targets between Ca and Zn, this is typical for most PIXE systems. The sharp low target atomic number cutoff below Z_2=10 is produced by low detection efficiency for K X-rays below 2 keV and the slower high target atomic number roll off above Z_2=40 for K and 90 for L is produced by the smaller ionisation cross sections for these more tightly bound inner shell electrons.

For a given target matrix and bombarding energy there is a Minimum Detectable Level (MDL), of each trace element. These depend on typical background levels in PIXE and can be derived from the data plotted in Fig. 7. Figure 8 is a plot of MDL's for two thick targets, oil shale and orchard leaves, for 50 μC charge of 2.5 MeV protons. A 0.26 mm perspex filter was placed in front of the detector to absorb low energy (< 3 keV) X-rays and increase sensitivity for trace elements above Ca (Z_2=20). This filter together with the detector efficiency accounts for the steep rise in the K shell MDL's for elements lighter than Cl. The plots of Fig. 8 show two main features of PIXE. Firstly trace element MDL's for different matrices have different values (or curves), this is brought about by the different background levels in the PIXE spectra. Secondly, for say MDL's around 10 $\mu g g^{-1}$ or better the PIXE technique covers most elements in the periodic table from Si upwards.

The minima for K and L series lines of Fig. 8 can be shifted to the left or right slightly ($Z_2 \pm 5$) by raising or lowering the ion energy (2 to 3 MeV) respectively.

Table 1 is a similar calculation of MDL's for trace elements in a quartz matrix together with an estimate of the error on these values. Again we see that MDLs less than 10 $\mu g g^{-1}$ are readily obtained for a wide range of trace elements.

TABLE 1 Minimum detectable concentrations for PIXE analysis of quartz

Element		Min Conc. ($\mu g g^{-1}$)	Expt Error (%)
Cl	17	44 ± 5	10-25
K	19	15 ± 1	10-25
Ca	20	11 ± 1	15-25
Ti	22	5.8 ± 0.6	15-30
Cr	24	3.5 ± 0.4	24-40
Fe	26	2.5 ± 0.4	15-25
Ni	28	2.2 ± 0.4	25-40
Zn	30	2.0 ± 0.4	25-40
Ge	32	1.9 ± 0.4	25-40
Rb	37	4.8 ± 0.5	25-40

Mitchell and Barfoot [6] produced a similar table but for theoretical sensitivities calculated for thicknesses (atoms cm^{-2}) of elements corresponding to 100 net X-ray counts on thin carbon backings for 1, 2 and 3 MeV protons of 1 μC charge and 10 msr solid angle. Parts of their table are reproduced in Table 2 for K and L shell X-rays for 3 MeV protons only. For elements from F to As 100 K X-ray counts occur for thicknesses around 10^{14} atoms / cm^2 or less. For elements between Sn and U thicknesses between $2x10^{13}$ and $8x10^{14}$ atoms/cm^2 respectively produce 100 L shell X-rays. When one considers that 10^{15} atoms/cm^2 is generally considered to be one monolayer of most pure materials these sensitivities are very good.

TABLE 2 Thin target thickness (atom/cm^2) for the production of 100 X-ray counts for 1 μC, 10 msr of 3 MeV protons.

	X-ray sensitivity for 100 net X-ray counts	
Element Z	K Shell (atoms/cm^2)	L Shell (atoms/cm^2)
Al 13	$2.02x10^{13}$	-
Ca 20	$4.17x10^{13}$	-
Fe 26	$9.08x10^{13}$	$2.19x10^{13}$
Zn 30	$2.19x10^{14}$	$1.28x10^{13}$
Zr 40	$1.92x10^{15}$	$1.12x10^{13}$
Sn 50	$1.89x10^{16}$	$2.05x10^{13}$
Nd 60	$2.63x10^{17}$	$4.44x10^{13}$
Ta 73	$5.75x10^{18}$	$1.27x10^{14}$
Hg 80	$2.40x10^{19}$	$2.38x10^{14}$
U 92	$3.57x10^{20}$	$7.58x10^{14}$

The PIXE technique is not only capable of producing data on trace element concentrations on the parts per million level but also at the same time can produce estimates of the bulk matrix composition. Fig. 9 taken from Cohen and Clayton [8] shows the measured PIXE concentrations versus the reference concentrations of hundreds of standard reference materials measured at our laboratories over the years. The concentrations cover six decades from $1\mu gg^{-1}$ to 100% and the solid line of least squares fit is given by (1.00±0.20). The standard reference materials cover an extremely broad range of matrices from biological to geological and demonstrate the real breadth of the PIXE analysis technique.

Table 3 is a summary of general uses, applications and limitations of PIXE and is taken from a review by Cahill [14]. It emphasises the power of the PIXE analytical technique which may also include the spatial resolution of better than 1 μm for microprobe systems and mass detection limits well below 1 nanogram.

TABLE 3

Particle-Induced X-Ray Emission

General Uses

- Nondestructive multielemental analysis of thin samples, sodium through uranium, to approximately 1 ppm or 10^{-9} g/cm^2
- Nondestructive multielemental analysis of thick samples for medium and heavy elements
- Semiquantitative analysis of elements versus depth
- Elemental analyses of large and/or fragile objects through external beam proton milliprobe
- Elemental analyses using proton microprobes, spatial resolution to a few microns, and mass detection limits below 10^{-16} g

Examples of Applications

- Analysis of air filters for a wide range of elements
- Analysis of atmospheric aerosols by particle size for source transport, removal, and effect studies
- Analysis of powdered plant materials and geological powders for broad elemental content
- Analysis of elemental content of waters, solute, and particulate phases, including suspended particles
- Medical analysis for elemental content, including toxicology and epidemeology
- Analysis of materials for the semiconductor industry and for coating technology
- Archaeological and historical studies of books and artifacts, often using external beams
- Forensic studies

Samples

- *Form*: Thin samples (generally no more than a 10-mg/cm^2 thick solid) are analyzed in vacuum, as are stabilized powders and evaporated fluids. Thick samples can be any solid and thickness, but proton beam penetration is typically 30 mg/cm^2 or approximately 0.15 mm (0.006 in.) in a geological sample
- *Size*: The sample area analyzed is on the order of millimeters to centimeters, except in microprobes, in which beam spot sizes approaching 1 μm are available
- *Preparation*: None for air filters and many materials. Powders and liquids must be stabilized, dried, and generally placed on a substrate, such as plastic. Thick samples can be pelletized

Limitations

- Access to an ion accelerator of a few mega electron volts is necessary
- Generally, no elements below sodium are quantified
- Elements must be present above approximately 1 ppm
- Sample damage is more likely than with some alternate methods
- No chemical information is generated
- Computer codes are necessary for large numbers of analyses

Estimated Analysis Time

- 30 s to 5 min in most cases; thousands of samples can be handled in a few days

Capabilities of Related Techniques

- *X-ray fluorescence*: With repeated analyses at different excitation energies, essentially equivalent or somewhat superior results can be obtained when sample size and mass are sufficient
- *Neutron activation analysis*: Variable elemental sensitivity to neutron trace levels for some elements, essentially none for other elements. Neutron activation analysis is generally best for detecting the least common elements, but performs the poorest on the most common elements, complementing x-ray techniques
- *Electron microprobe*: Excellent spatial resolution (approximately 1 μm), but elemental mass sensitivity only approximately one part per thousand
- *Optical methods*: Atomic absorption or emission spectroscopy, for example, are generally applicable to elements capable of being dissolved or dispersed for introduction into a plasma

4. PIXE YIELDS

Since the range of charged particles in matter is limited PIXE is a surface technique only. For example, 3 MeV protons in C or Si have ranges of 65 and 95 microns respectively, while for 3 MeV alphas these ranges are only 9 and 12 microns respectively. Hence for bulk analysis using PIXE one must be certain that the target is homogeneous or at least that the first few microns of the surface are representative of the bulk of the material. This problem is further enhanced by two facts (i) the ion loses energy along its path and hence the X-ray production falls dramatically with depth into the target, (ii) the emerging X-rays are absorbed by the target. A good rule of thumb is that 90% of the total X-ray yield is usually produced in the first quarter of the ion range in the material [7,8].

Thin targets are defined as those for which ion energy losses and X-ray absorption effects are negligible, say less than 5%. Thick targets are usually those for which the incident ion is completely stopped and the calculated yields for these require integration over ion energy loss and emergent X-ray absorption. Expressions for yields for both thin and thick targets have been discussed at length elsewhere [8,9,12] and will not be reproduced here. Several papers [6,8,12,15] and the references therein have discussed in detail the data bases necessary to compute these X-ray yields for known concentrations of trace elements in known matrices. Computer codes have been written by a variecy of laboratories to not only analyse the peak areas of PIXE spectra [9,16,17] but also convert these areas to concentrations [17].

Fig. 10, taken from Bird et al. [7] shows the calculations of K and L shell yields for thick targets compared with similar yields for other Ion Beam Analysis (IBA) techniques such as Rutherford Backscattering (RBS) and Proton Induced Gamma-Ray Emission (PIGME). The PIXE technique clearly produces yields several orders of magnitude larger over a wide range of trace elements in the periodic table.

Fig. 11 shows the measured and calculated Kalpha X-ray yield versus trace element atomic number for a known reference thick hydroxy-apatite matrix (human tooth). The calculated values were obtained using the THIKPC codes of Clayton [17] and the sharp discontinuities at Z=15 and 20 are due to the P and Ca K absorption edges for hydroxy-apatite [$Ca_{10}(PO_4)_6(OH)_2$]. The ratio of the experimentally measured points to the theoretical line was (1.03±0.07) for the 10 reference elements present in the apatite and confirms the current state of PIXE knowledge to predict yields in quite complicated matrices.

Similar techniques also work for many trace elements in a simple matrix. For example, Fig. 12 is a PIXE spectrum for over 40 elements in a graphite matrix [18], each with a nominal concentration of around 200 $\mu g g^{-1}$. The spectrum was accumulated using 2.5 MeV protons, 1.5mm thick perspex filter in front of the detector with a solid angle of 1.34 msr. The solid curve is a fit to the data (dashed curve) using the PIXAN package of Clayton [17]. The measurement took less than 20 minutes. The theoretical yields obtained are compared with the experimental values in Fig. 13 and for elements between Ti and Sr differ by an average of less than 6% from the reference values.

These figures show that both thin and thick target PIXE calculations, and hence data bases [12,15], have reached such a degree of sophistication that X-ray yields for trace elements can now be predicted at the 5% level for an extremely diverse range of known target matrices. Further evidence for this is given by Maenhaut and Raemdonck [19] who measured a set of accurate thin film standards and compared this with absolute theoretical calculations. They found an individual element could be analysed with an accuracy of better than 4% for elements from Na to Sn.

The main advantage of having reliable data bases to produce reliable yield curves for a given matrix is that a single external or internal standard can be used to normalise this yield curve to the experimental results and hence produce yields for most elements across the periodic table. For example, if the yield curve for Fig. 11 is normalised to the known value of Ca in apatite (39.9 wt%) to give the experimentally measured value of the number of X-rays in the Ca Kalpha peak then Kalpha yields for all other elements from Z=10 to 50 can be obtained. This then would be normalising to the internal Ca standard in apatite and reduces all uncertainties associated with charge collection, detection efficiency and solid angle. This procedure is practised by many laboratories in varying forms, often uncommon elements such as Y or Sr are used in known amounts to spike powdered samples before pressing into a solid target. The X-ray yield results are then normalised to the known Kalpha yields from these internal standards.

5. PIXE SYSTEMS

It has already been shown that ion energies between 1 and 5 MeV are ideal for PIXE. This means that accelerator voltages up to 5 MV are required. Most PIXE machines are either old nuclear physics single ended Van de Graaff accelerators or more modern Tandetron or Pelletron accelerators. The ion beam currents from these machines are typically a few microamps to hundreds of microamps, this is far in excess of the 1 to few hundred nanoamps used by most PIXE experiments. The accelerator terminal voltage

is usually stabilised to a few keV or better and the excess ion currents reduced by beam transport through bending magnets, quadrupoles and apertures. Fig. 14 is a floor plan of the 3 MV Van de Graaff accelerator at Lucas Heights. The accelerator and the main analysing magnet are contained in a concrete block house or cell for radiation shielding. This is really only necessary when deuteron beams which produce neutrons are used. For protons radiation levels only become significant near the ion source and adjacent to the accelerator tank and shielding is not usually a problem. The analysing magnet can switch the ion beam down 3 legs into the main bay. The centre and right legs have switching magnets on them. So there are about 11 different legs operating at the present time. The main PIXE/PIGME system is located in a low noise (electronic) background area called the Alcove adjacent to our clean sample preparation room. Typically we would run 2.5 MeV protons, 10 μA, 10mm diameter beams onto the beam stop before the analysing magnet in the cell. This produces about 2 μA, 5mm diameter beam spot after the switching magnet in the main bay and with quadrupole defocusing and selected apertures we can dial up anything from a 1 mm diameter 1 nA beam spot to an 8mm several hundred nanoamp spot.

Currently there are 3 different PIXE systems operating on our accelerator, one for batch analysis of many targets, one miniprobe (50μm) system for detailed analysis of individual targets and one external beam system for large targets unable to be placed in vacuum.

5.1 VACUUM PIXE

A typical schematic of an experimental end station or target chamber for an in vacuum PIXE system is shown in Fig. 15. The Si(Li) or X-ray detector is placed at a backward angle of 135 degrees. A meter long target stick can hold up to 60 samples at a time and is driven across the proton beam by a computer controlled stepping motor attached to the target stick. A carbon Faraday cup completely encloses the target for accurate target measurement and carbon electron suppression and scraper apertures are placed in front of the cup to define the beam size. The electron flood system inside the Faraday cup is used to spray electrically insulated targets with electrons to reduce the secondary electron Bremsstrahlung background in the PIXE spectra (see below). Fig. 16 shows a similar system, in this case the whole chamber is insulated from ground and acts as the Faraday cup and the space restrictions introduced by an internal cup are removed. A gamma ray detector for simultaneous PIGME work is also shown attached to the chamber. A schematic of the target holder (H) is shown together with one method of mounting a solid PIXE sample (S). Vacuums of the order of 0.1mPa or better are typical but chamber pressures as high as 0.1 Pa may be used in some cases to overcome charging effects instead of the electron flood systems described above.

5.2 EXTERNAL PIXE

Some targets are either too big or too delicate to place in a vacuum system. For these the ion beam may be brought out into air or a helium atmosphere through a thin foil, usually Kapton or Ni. External systems are to be discussed by others at this meeting and will not be treated in detail here. Fig. 17 is a schematic of a typical external beam PIXE. The exit foil is Kapton resting on a perforated graphite support which transmits 50% of the beam. The target can be placed within a couple of cms. of the exit window.

Care should be taken with radiation from external beams. Contact with the skin will produce radiation burns from Mrad proton doses. X-ray and gamma ray fluxes can be high from the air and exit foils. Hundreds of mrads a few cms. from the exit windows are possible and care should be taken not to irradiate the eyes or other body parts.

Beryllium extraction windows should never be used as the neutron (p,n) reaction produces prolific numbers of neutrons at PIXE energies. Figs. 18 and 19 show typical external beam PIXE spectra for an investigation of glaze on a large Iranian bowl and the pigments in a 17th century Italian painting. The Argon peak around 3 keV is a typical feature of external Pixe spectra in air.

5.3 Si(Li) DETECTORS

X-rays are virtually always measured with energy dispersive Si(Li) detector systems. The use of these semiconductor detectors rests on the principle of absorption of photons through ionisation which occurs when energetic electron produced via the photo-electric effect loses its energy. The photo electron creates many electron-hole pairs in the Si(Li) crystal and a bias applied across the crystal sweeps out the charge to the corresponding electrode. This charge pulse is amplified and its height is proportional to the total energy deposited in the crystal detector. The energy required to generate an electron hole pair in Si is only about 3.8 eV at liquid nitrogen temperatures (77°K). The keV X-rays will generate large numbers of hole pairs which yield excellent statistics for measurement of the size of the charge pulse. Finally since the mobility of these charge carriers (electrons) is high most are collected and the Si(Li) detector has good resolution, typically 150 eV at 6 keV or ($\Delta E/E$) approximately 2.5%. These ideas and principles have been thoroughly discussed by Woldseth [20]. A comprehensive Si(Li) detector efficiency model has been presented by Cohen [21] covering the energy range 3-60 keV.

Fig. 20 shows the efficiency of a typical Si(Li) detector with a thin 8μm Be window as a function of X-ray energy. The experimental measurements were taken using X-ray standard sources and by measuring X-rays from known PIXE and HIXE targets. Clearly below 3 keV the efficiency as calculated from the manufacturer's specifications overestimates the experimental results. The detector crystals are held at 77°K and it was shown by Cohen [22] that this discrepancy was due to an ice buildup on the front face of the detector with a thin Be window. Ice thicknesses of between 10-20μm were common and easily removed by warming up the crystal (to 50°C) and pumping the cryostat for a few days. This buildup is present in most thin windowed detectors and increases in thickness with time. Measurements of this low energy efficiency degradation with time are given in Fig. 21. Over 36 months the ice thickness grew from 1 or 2 μm to 50μm at which point the detector was "sweating" so much it would not hold liquid nitrogen and the cryostat had to be pumped. For this range of ice thickness the efficiency of this detector for the Al Kalpha X-ray dropped from 35% to zero.

A simple technique to measure the thickness of ice build up on the front face of detectors has been described by Cohen [8,22] together with a full description of useful X-rays from Am-241 source for detector efficiency calibration. Figure 22 shows the X-ray spectrum from an Am-241 source and the 20 or so X-ray lines that can be used to calibrate Si(Li) detector efficiencies over the energy range 2-30 keV. The M X-ray lines are particularly sensitive to ice buildup.

5.4 ELECTRONICS

The signals from the Si(Li) detector are amplified, fed into an ADC and computing system for analysis. A typical block diagram for the electronic setup of a PIXE system is shown in Fig. 23. Logic busy signals are used to gate the ADC's deadtime and to adjust the spectrum live times. The inhibit signal from the main amplifier is used in the anticoincidence input of the ADC to reject pileup pulses in the spectrum. Spectrum run times are determined by the total accumulated charge on the target. This is monitored by a current to frequency convertor and the total number of pulses from this is used to drive an external start/stop clock for the run times.

5.5 FILTERS

Shaping the detector efficiency to suit the count rate into various peaks in a PIXE spectrum is a common way of optimising the system to give the best sensitivities in the shortest times.

If the spectrum contains mainly light elements whose K X-rays lie below 10 keV then generally minimal filtering is used providing the Be window thickness is sufficient to completely stop the scattered proton beam. If the spectrum contains high count rates into high energy X-rays with only trace elements in the lower energy regions then several hundreds of microns of Mylar or Perspex filter may be used. Many spectra however have significant count rates across the energy region and pinhole or funny filters are used. The effect on efficiency of these 3 types of filters is shown in Fig. 24. The pinhole filter is a 2mm Perspex filter with a 70μm pinhole through its centre to allow a small fraction of the lower energy X-rays through. Figs. 25 to 27 show the effects of such filters on PIXE spectra. Fig. 25 is the spectrum from 2.6 MeV protons on an aerosol filter paper taken near Al smelter pots. The 55μm Be was used to just stop the scattered protons. Clearly the filter paper contains lots of Al, Si, P, S and Fe with trace elements of Zn and As. No X-rays are detected above 10 keV. Fig. 26 shows the effects of pinhole and Perspex filters on 2.5 MeV proton PIXE spectra, for a USGS oil shale reference standard sample. The Perspex filter completely removes the light element X-rays. Fig. 26 demonstrates the use of a pinhole filter when both light elements like Al and heavier elements like Zr and Mo are wanted. Fig. 27 shows the spectrum from a pure Nb crystal cut with a W saw. Here 0.526 mm of Perspex were used to reduce the Bremsstrahlung background in the region up to channel 300 (6 keV) and the trace amounts of W are clearly seen.

Thin metal foil filters may also be used when particular peaks rather than whole regions of the spectrum need to be reduced. This is done by selecting a foil thickness (just a few microns) whose K edge energy lies just below that for the Kalpha line of the peak whose count rate must be reduced. For example 12μm of Cr filter will reduce the count rate into the Fe Kalpha peak by 98.5% but only reduced the adjacent elements Mn Kalpha and Cu Kalpha by 47.5% and 90% respectively.

5.6 SPECTRUM ARTIFACTS

We have already shown many experimental PIXE spectra which have been fitted by programs such as the PIXAN package of Clayton [17], see for example Figs. 25 and 26. These fits assume some knowledge of the spectral response of your detection system. Peaks shapes are basically Gaussian with low energy steps and tails as shown in Fig. 28a. These steps and tails are typically 2 to 3 orders of magnitude smaller than the primary amplitude and are produced by inefficient charge collection in the detector. If the amplitude and slope of these are allowed to vary in the fitting routines then excellent fits like those shown in Fig. 28b are obtained. This is a PIXE spectrum for a pure thick Sr sample taken from Ref. [8]. The amplitude of these steps and tails is both energy and count rate dependent.

Fig. 29 is the PIXE spectrum from a pure Ti target and clearly shows two more spectrum artifacts, namely the lower energy escape peak and sum peaks which occur at approximately twice the energy of the primary peak. For a given element the escape peak is a constant fraction (few percent of the primary peak amplitude and is not count rate dependent. It is produced by the escape of Si Kalpha X-rays from the detector crystal. The escape peak energy is always 1.74 keV lower than the primary X-ray energy from which it originates. Each X-ray peak will have its associated escape peak.

The sum peak, at twice the primary peak energy, is produced by the non zero pulse pair resolution time of the detector electronic system (usually 0.5 μs). Pulses arriving in the detector within this time interval are not counted as two pulses but as one with twice the energy. Clearly the peak height of this pulse is count rate dependent but in most typical systems it is around 3 orders of magnitude smaller than the primary peak. Again each primary peak can sum with itself and every other peak in the system. Hence for n X-ray peaks there are (n+1)n/2 sum peaks at the sum energy of each peak. For high count rates (>5kHz) into many element peaks this effect could seriously hamper the analysis of real trace element peaks which overlap with them. Fig. 30, taken from Ref. [8], shows the 10 to 14 keV region of a sample containing 6% Cr and 6% Fe. The top curve shows PIXAN fits without sum peaks and the bottom curve shows superior fits obtained by including the 10 sum peaks for the 4 Cr and Fe Kalpha and Kbeta peaks between 10.8 keV and 14 keV. The peaks for Br K alpha and beta at 11.9 and 13.3 keV and the Rb Kalpha at 13.4 keV can still be accurately extracted by the PIXAN package after inclusion of these sum peaks.

One further gross artifact that often appears in the PIXE spectrum for electrically insulated targets is an increased Bremsstrahlung background extending in some instances all the way out to several 10's of keV. Fig. 31 taken from Ref. [7] shows the PIXE spectra for a Motupure pottery sample. The dashed line shows the effects of charging of the insulated sample and the solid line shows the effective reduction of this background by flooding the target with electrons from a heated carbon filament. Clearly the sensitivity for the elements in the region around Sr and Zr is dramatically improved.

6. SUMMARY OF PIXE OPERATING CONDITIONS

Typical PIXE operating conditions are given in Table 4 for a non microprobe system.

TABLE 4 Typical PIXE operating conditions

Operating Characteristics	Value
Proton energy	2-3 MeV
Beam current on target	1-500nA
Maximum beam current density (for Mylar)	1nA/mm^2
Beam spot diameter	0.5-10mm
Data acquisition rate	100Hz-5kHz
Run times	30s-10mins.
Detector resolution Si(Li)	140-180 eV
Detector efficiency (100%)	10-20 keV
Detector diameter/thickness	3-6mm/4-6mm
Detector target distances	20-200mm
Detector window thickness	7-50μm Be
Detector ice thickness	5-50μm
Amplifier shaping constant (τ)	3-10μs
Amplifier pulse pair resolution time	0.5μs
Electron suppression voltages	-300V
Electron flood filaments (carbon)	red to white hot
Filters (Be)	50μm
Filters (Mylar/Perspex)	10-500μm/0.5-6mm
Filters (Metal foils)	5-20μm
X-ray energies (Na to U)	1-40 keV

7. PIXE APPLICATIONS

Applications of PIXE before 1980 in the areas of atmospheric physics, biology and medicine, geology and soil science, materials science, archaeology and nonbiological liquid analysis have been reviewed by Cahill [13]. More recent applications of the PIXE techniques have already been discussed in the 30 or so figures presented so far in this review. As already stated the variety of applications is enormous and best represented by the Proceedings of the International Conference on PIXE and Its Analytical Applications [3-5]. The range of trace element concentrations for different samples analysed by PIXE is given in Table 5.

We shall not go into much more detail here except to present a few interesting case studies conducted recently at our Laboratories at Lucas Heights. These few examples have been selected to demonstrate the power of the PIXE technique.

The earliest publications on PIXE included analyses of aerosol filter papers collected from the atmosphere and this work still continues today at a great pace, see Ref. [4] pages 235-372. The reasons for this type of study are obvious. They encompass occupational health, atmospheric

TABLE 5

Range $\mu g\ g^{-1}$	Sample								
	Serum	Urine	Hair	Bone	"Body Organs"	Geological	Botanical	Aerosol ng/m^3 remote	Aerosol ng/m^3 polluted
0.5-20	Fe Cu Zn Br	Fe Cu Zn Br Rb Sr	Al Ti Cr Mn Ni Pb Hg Rb Sr	Mn Cu Fe Pb Br	Al Ti Mn Cu Br Rb (Pb)	Ga Ge Pb Se Br Th U Mo	Ti Cu Br Rb	Mn Cu Zn Br Pb	
20-100	Mg		P K Fe Cu Br	Sr	Fe Zn Ca	Cr Ni As Rb Sr Y Zr	Fe Zn Sr	Mg Al S K Ca Fe	Mn Ni
100-1000	P K Ca	Mg S K Ca	Na Mg Cl Ca Zn	Zn	Mg P	S Cl Ba V Mn Cu Zn Sr	Na Al S Mn	Na Cl	S K Cu Zn Pb Br
>1000	Na Cl	Na P Cl	S	Na Mg P S Cl Ca	Na P S Cl K	Na Mg Al Si P K Ca Ti Fe	Mg P Cl K Ca		Na Mg Al Cl Ca Fe

visibility, acid rain, soil erosion and ecological effects. PIXE can contribute to these studies despite the very small masses collected on filter papers.

There are over 20 elements present at the 0.1% level or less in an average urban air sample. Fig. 32 shows a typical PIXE spectrum obtained for an urban aerosol filter paper after just a few minutes of machine running time. The MDL's in nanograms per unit area of filter paper versus trace element atomic number, calculated for typical aerosol filter samples are also shown. Values of a few $ngcm^{-2}$ are readily obtainable for elements from Ca to Zn. Cahill [5] reports on large scale aerosol monitoring programs which extend across the whole of North America, containing more than 50 sampling stations, and generating tens of thousands of PIXE samples a year.

Duerden et al [23] have reported a combination of ion beam techniques to analyse desert varnish cover on rock surfaces from western NSW in Australia. Desert varnish is a naturally occurring shiny dark coloured thin (5 to 200 μm) silicate clay mineral layer, containing Ca, Ti, K, P,m S and Na, which occur on fine-grained iron bearing rocks. Younger varnish may contain higher ratios of (Ca+K) to Ti than older varnish. Measurement of this varnish layer on or near rock bearing aboriginal carvings may be able to better date these artifacts. In this study X-rays induced by protons and helium ions were used as well as the PIGME and RBS techniques in an attempt to distinguish trace elements both in the varnish and the substrate rock.

X-ray and gamma ray yields were calculated as functions of incident ion energy as a function of sample depth. Fig. 33a shows proton depth in the sample (in mg/cm^2) for 50% contribution to the gamma ray yield for various light trace elements between Li and Mg. Similar calculations are shown for PIXE and HIXE for elements from Si upwards and for ion energies between 1.8 and 2.6 MeV in Figs. 33b and c. By varying the incident ion and its energy the varnish composition was measured for depths of around 20μm for protons but only 1 or 2 μm for helium ions and differences between the varnish cover and its underlying rock were easily distinguished.

One of the main strengths of the PIXE system is its ability to analyse very small samples. Kim et al [24] report on a quantitative PIXE study for measuring elemental composition of teeth, on the radula, of limpets. Fig. 34 shows the cross section of a limpet's mouth parts. The radula about 70 mm long contains the teeth, each of which is only about 300 μm long and 30 μm wide. The teeth have different stages of development and biomineralisation depending on their position along the radula, later stage teeth may contain up to 65% Fe. Teeth from several radulae at

similar stages of development were extracted, powdered, spiked with a V internal standard and pressed into pellets containing less than 1 mg of sample. Fig. 35 shows the PIXE spectra for two samples from different stages of development containing different amounts of Si. PIXE allowed elemental composition along the radula to be followed quantitatively. The calculated Kalpha yield curves for trace elements from Al to Zr are shown in Fig. 36. The concentrations of selected elements for four stages of mineralisation are shown in Fig. 37. The Fe concentration varies from less than 10 mgg^{-1} to over 65% along the radula an extremely high Fe content for a biological system.

The multielement analysis capability of PIXE is also another of its strengths. X-ray peaks from up to 40 elements (see Fig. 12) can be analysed in one spectrum simultaneously. However this many peaks can also interfere with other smaller peaks that may be of interest. An example of this is shown in Figs. 38a to c, which shows the PIXE spectrum from an aluminium blast furnace slag over the X-ray energy range 10 to 14 keV. The slag contains 29% Pb and the analysis required concentrations for Se and As to be extracted. The Pb Lalpha and Leta lines interfere with As Kalpha and Se Kalpha lines respectively. Using the PIXAN analysis package we first included Se (Fig. 38b) and then As (Fig. 38c). The fits (solid curves) become progressively closer to the experiment (dashed curves) eventually providing estimates of 700 μgg^{-1} for Se and 3.2% As in the presence of 29% Pb. Calculations show that MDL's for Se and As were 200 μgg^{-1} and 1500 μgg^{-1} respectively in the presence of 29% Pb.

The multielemental capabilities of PIXE have also been applied extensively at Lucas Heights to the fingerprinting of tens of thousands of obsidian glass samples [7]. Fig. 39 shows the PIXE spectrum, taken with a pinhole filter, of Lou Island obsidian glass. Elements from Na to Zr are clearly visible. Fingerprints have been obtained for all known obsidian sources from Australia, New Zealand and the South Pacific region as well as many artifacts from Melanesia, New Zealand and neighbouring islands. The only sample preparation was an ultrasonic wash in benzene. The analysis of artifacts and source obsidian has enabled archaeologists to establish trade patterns between natives in New Britain as early as 11000 BP and over distances of 400 km, including significant water crossings as early as 6800 BP. By 3500 BP, prime quality obsidian was extensively distributed over 3500 km of the Melanesian Island chain from the Admiralty Islands to Vanuatu (New Hebrides), see Fig. 40.

8. PIXE AND OTHER TECHNIQUES

The principles, instrumentation and methodological aspects of other techniques competing with PIXE have been very thoroughly reviewed in an

excellent recent article by Maenhaut [25]. The techniques he discusses include NAA, XRF including total reflection XRF and synchrotron radiation XRF, atomic emission (AES), atomic absorption (AAS) and atomic fluorescence spectrometry (AFS) and atomic mass spectrometry, in particular ICPMS. Particular emphasis is placed on instrument cost, speed of analysis, sample type and mass required for analysis, accuracy and detection limits. Table 6 and 7 have been taken from this review and summarises its findings.

TABLE 6 Detection limits, in $\mu g/g$ solid sample, for 17 elements in seven analytical techniques.

Element	INAA	ED-XRF[a)]	PIXE[a)]	ICP-AES[b)]	ETA-AAS[b)]	ICP-MS[b)]
V	0.03	20	1.3	3.5	0.2	0.03
Cr	0.03	16	0.8	4	0.01	0.06
Mn	0.001	12	0.6	0.95	0.01	0.10
Fe	6	12	0.5	3	0.02	
Ni	3	5	0.4	6.5	0.2	0.10
Cu	0.03	6	0.3	3.5	0.02	0.32
Zn	0.3	5	0.3	1.2	0.001	0.21
As	0.03	4	0.4	35	0.2	0.04
Se	0.03	2	0.4	50	0.5	0.79
Mo	0.3	5	1.9	5.5	0.02	0.04
Cd	0.6	6	10	1.7	0.003	0.06
In	0.0006		14	40		0.07
Sn	1	8	16	17	0.1	0.06
Sb	0.01	8	14	20	0.1	0.05
Hg	0.003	7	1.0	17	2	0.02
Tl			1.1	25	0.1	
Pb		8	1.1	30	0.05	0.05

a) For 1 mg/cm^2 sample layers of a light element matrix on a thin substrate film.

b) For solutions containing 0.1% dissolved solid sample.

9. PIXE COSTS

Table 7 quotes the total costs of a PIXE system as over US$500k. This of course depends heavily on the type of accelerator and the voltage required. The latest quotes in US dollars for a 1 MV NEC Pellatron (2 MeV protons) are around US$350k, this includes $200k for the accelerator, $90k for the low energy injection and ion source and $60k for the high energy PIXE system including Si(Li) detector. An HVEE 1 MV Tandetron including duoplasmatron 358 ion source, 860 Cs sputter source, dual injection magnet, electrostatic quadrupole triplet, turbo pumps and controls is US$880k. A high energy switch magnet ($35K), beam lines and controls ($62k) and PIXE system ($60k) are not included in this quote.

The HVEE 3MV AN2500 Van de Graaff accelerator only with RF ion source was quoted at US$535k. High energy beamlines, chambers and switching magnets are extra.

Spare parts and accessories for these accelerators are also not cheap. Accelerator tubes for HVEE Tandetron are $45k each. Beam profile monitors $15k each.

TABLE 7 Summary of some characteristics of analytical techniques for bulk trace element analysis

Technique	Price of Instr.[a)]	Detec.limit[b)] [μg/g]or[ng/ml]	Spectral Interf.	Matrix Effects	Multi-Element	Preferred Sample Type
INAA	(++++)	0.001-1	Low	Low	Yes	Solid
XRF[c)]	+/++	1-10	High/Low	Medium	Yes	Solid
TXRF	++	~ 0.2	High	Medium	Yes	Liquid[d)]
PIXE	(++++)	0.2-3	High	Medium	Yes	Solid
ICP-AES	++	1-30	High	Medium	Yes	Liquid
ETA-AAS	+	0.01-02	Medium	High	No	Liquid
ICP-MS	+++	0.03-0.1	High	High	Yes	Liquid

a) Code for price of instrument: + indicates less than $100,000; ++ from $100,000 to $250,000; +++ from $250,000 to $500,000; and ++++ more than $500,000.

b) Detection limits are in μg/g for INAA, XRF and PIXE, and in ng/ml for the other techniques, including TXRF.

c) The indications on this line before each slash apply to ED-XRF, those after each slash to WD-XRF.

d) The dried residue of the liquid on a totally reflecting substrate is subjected to analysis.

Electronic components and modules such as amplifiers and power supplies for a PIXE system are typically US$1500 to $2000 each and a standard Si(Li) detector costs around US$15k. An 8 port 25 cm diameter chamber costs around $15k with accessories and a 160 l/min turbo pump with roughing pump sells for around US$10k.

Few accelerators are used exclusively for PIXE and most carry other IBA techniques such as PIGME, RBS, FRA and NRA. A recent international survey by us on accelerator charges shows typical values were around US$150-300/hour or US$2000-3000/day. However the high throughput capabilities of PIXE together with full computer automation does allow for single sample

charges to be as low as $20/sample. However a more realistic range appears to be $30 to $70 per sample depending on the number of elements required and the levels at which they occur.

10. CONCLUSION

Johansson [5] in his summary of the 5th International Conference on PIXE and Its Applications points out that a PIXE spectrum looks the same as it did 20 years ago, since detector resolutions have not improved significantly and protons of a few MeV still give the best overall performance. The thing that has improved is our knowledge of all the details of PIXE and the PIXE procedure. An accuracy and precision of a few percent for thick target PIXE as well as thin targets can now be achieved. PIXE is now a standard world-wide accelerator based analytical technique.

The author acknowledges that a lot of the data presented here was obtained by many others in the Ansto IBA group over the last 15 years.

11. REFERENCES

[1] S.A.E. Johansson and T.B. Johansson,
Nucl. Instr. and Methods, 137(1976)473.

[2] T.B. Johansson, R. Akselsson and S.A.E. Johansson,
Nucl. Instr. and Methods, B4(1970)141.

[3] Proceedings of 3rd Int. Conf. on PIXE and Its Analytical Applications, Heidleberg, July, 1983, Nucl. Instr. and Methods, B3(1984)1-711.

[4] Proceedings of 4th Int. Conf. on PIXE and Its Analytical Applications, Florida, June, 1986, Nucl. Instr. and Methods, B22(1987)1-484.

[5] Proceedings of 5th Int. Conf. on PIXE and Its Analytical Applications, Amsterdam, August, 1989, Nucl. Instr. and Methods, B49(1990)1-589.

[6] "Particle Induced X-ray Emission Analysis Application to Analytical Problems", I.V. Mitchell and K.M. Barfoot, Nucl. Science Applications, 1(1981)99-162.

[7] "Ion Beam Techniques in Archaeology and the Arts", J.R. Bird, P. Duerden and D.J. Wilson, Nucl. Science Applications, 1(1983)357.

[8] "Ion Induced X-ray Emission", D.D. Cohen and E. Clayton in Ion Beams for Materials Analysis (Academic Press, New York, 1989) eds. J.R. Bird and J.S. Williams p209-260.

[9] "A Novel Technique for Elemental Analysis" (Wiley, New York, 1988) S.A.E. Johansson and J.L. Campbell.

[10] "Principles and Applications of High Energy Ion Beams" eds. F. Watt and G.W. Grime, 1987, Adam Hilger, Bristol.

[11] D.D. Cohen, M.H. Harrigan, Atomic Data Nucl. Data Tables, 33(1985)255.

[12] D.D. Cohen and E. Clayton, Nucl. Instr. and Methods, B22(1987)59.

[13] T.A. Cahill, Ann. Rev. Nucl. Part. Sci., 30(1980)211.

[14] "Particle Induced X-ray Emission", T.A. Cahill, Metals Materials Characterisation Handbook, 9th edition, vol.10, American Society for Metals, 1985, p102.

[15] D.D. Cohen, Nucl. Instr. and Methods, B49(1990)1.

[16] J.L. Campbell et al, Nucl. Instr. and Methods, B14(1986)204.

[17] E. Clayton, PIXAN Package, AAEC Report No. M113(1986).

[18] E. Clayton, Nucl. Instr. and Methods, 191(1981)567.

[19] W. Maenhaut and H. Raemdonck, Nucl. Instr. and Methods, B1(1984)123.

[20] R. Woldseth, X-ray Energy Spectrometry, published by Kevex Corp, USA (1973).

[21] D.D. Cohen, Nucl. Instr. and Methods, 178(1980)481.

[22] D.D. Cohen, X-ray Spectrometry, 16(1987)237.

[23] P. Duerden, D.D. Cohen, D. Dragovich and E. Clayton, Nucl. Instr. and Methods, B15(1986)643.

[24] K.S. Kim, D.D. Cohen, J. Webb and D.J. Macey, Nucl. Instr. and Methods, B22(1987)227.

[25] W. Maenhaut, Nucl. Instr. and Methods, B49(1990)518.

FIGURE CAPTIONS

Figure 1. Ion beam interactions with solid targets.

Figure 2. Allowable K and L shell X-ray transitions for an initial vacancy in the K and L shell.

Figure 3. X-ray energy bands versus target atomic number. ESC corresponds to the escape peak energies for the primary alpha X-ray.

Figure 4. (a) The K shell spectrum of pure Cu; (b) The L shell spectrum of pure Pb.

Figure 5. Typical PIXE spectrum for 2.6 MeV protons on an aerosol filter paper taken from an urban area near Melbourne.

Figure 6. K, L and M shell ionisation probabilities versus normalised ion energy. Taken from Ref.[8].

Figure 7. Calculated X-ray yield /100 μC/msr for thick targets and various proton energies.

Figure 8. Measured minimum detectable limits for 2.5 MeV protons on NBS standard reference materials.

Figure 9. Comparison of Reference concentrations versus measured PIXE concentrations covering six decades of concentration.

Figure 10. Comparison of yields/μC/sr for PIXE, PIGME, RBS and NRA. Taken from Ref.[7].

Figure 11. The K alpha yield for an apatite matrix without filter as a function of trace element atomic number for 2.26 MeV protons 0.06 msr.

Figure 12. The PIXE spectrum from a sample containing over 40 elements at the 200 $\mu g\ g^{-1}$ in a graphite matrix. The figure shows 26 elements in the range 4 to 20 keV, for 100 μC of 2.5 MeV protons with 1.5 mm perspex filter.

Figure 13. The trace element K alpha X-ray yields for a graphite matrix for 2.5 MeV protons and solid angle of 1.34 msr.

Figure 14. Floor plan of the Lucas Heights 3 MV Van de Graaff accelerator.

Figure 15. Schematic of a typical PIXE target chamber.

Figure 16. Schematic of a typical PIXE/PIGME system with target holder (H) and sample mount (S).

Figure 17. Schematic of a typical external PIXE/PIGME system showing window and graphite grid support.

Figure 18. Typical external beam PIXE spectra for 2.5 MeV protons on an Iranian bowl for two different spots on its surface.

Figure 19. External beam PIXE spectrum of 17^{th} century Italian painting. Blue pigments are identified by the presence of Co, Si and K.

Figure 21. Variation of Si(Li) detector efficiency with time due to ice buildup on the detector front face.

Figure 33. The depth reached in a desert varnish sample for 50% contribution to the yield for (a) PIGME; (b) PIXE; and (c) HIXE.

Figure 34. Baccal cavity and mouth parts of the limpet Patella Vulgata.

Figure 35. PIXE spectra from two different stages of Limpet radula development.

Figure 36. Calculated PIXE yields for limpet teeth versus target trace element atomic number.

Figure 37. A plot of the elemental concentrations along the limpet radula representing various stages of mineralisation.

Figure 38. PIXE spectra for blast furnace slag containing 29% Pb. The dashed curves are the experimental data and the solid curves are the fits using the PIXAN package of Clayton. (a) no As or Se (b) Pb and 700 μgg^{-1} of Se (c) As 3.2% and Se.

Figure 39. PIXE spectrum of obsidian glass taken for 2.5 MeV protons and using a pinhole filter.

Figure 40. Map of island groups to the north of Australia showing native trade patterns as determined by obsidian analysis.

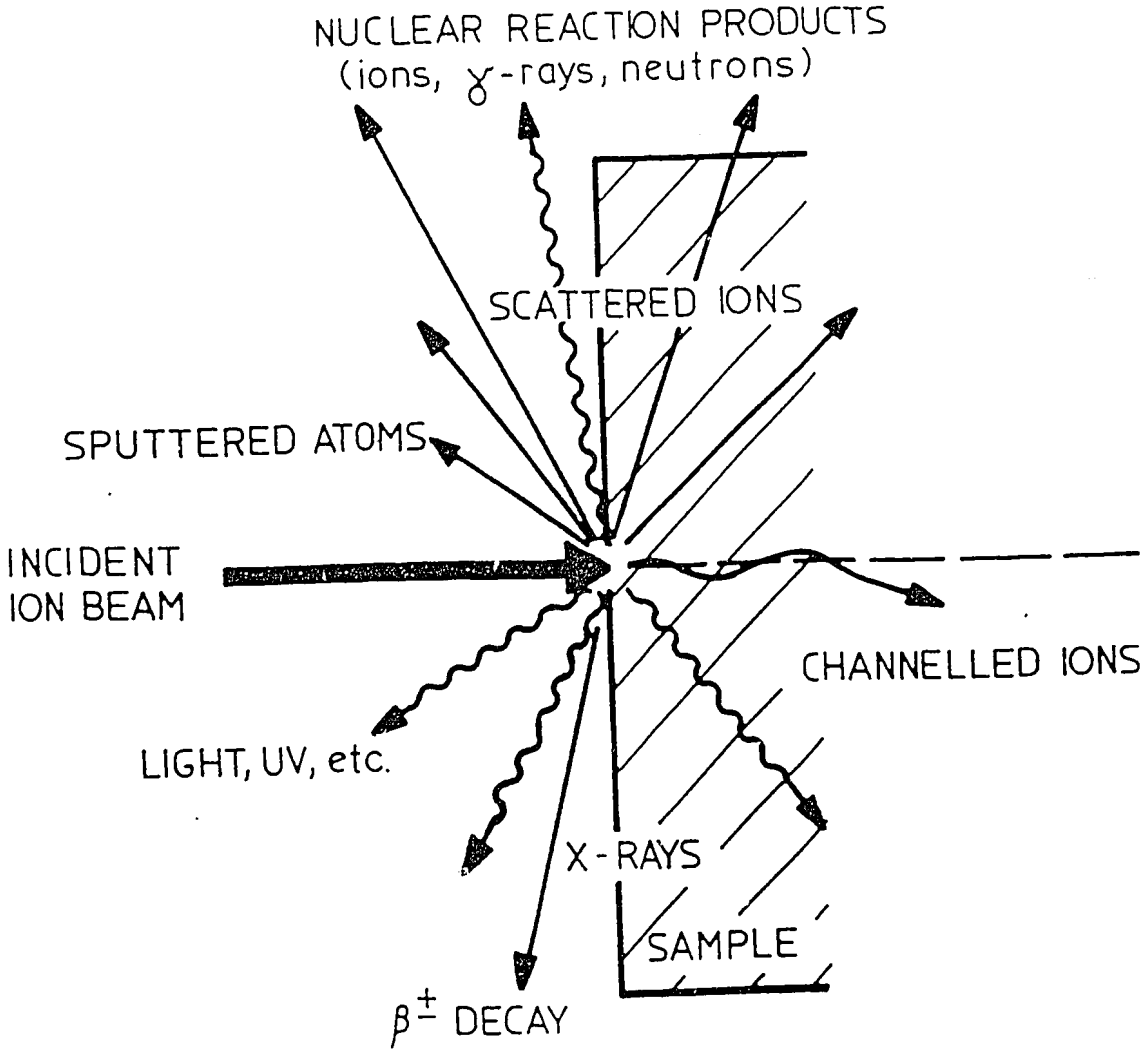
NUCLEAR REACTION PRODUCTS
(ions, γ-rays, neutrons)
SCATTERED IONS
SPUTTERED ATOMS
INCIDENT
ION BEAM
CHANNELLED IONS
LIGHT, UV, etc.
X-RAYS
SAMPLE
β± DECAY

Fig. 1

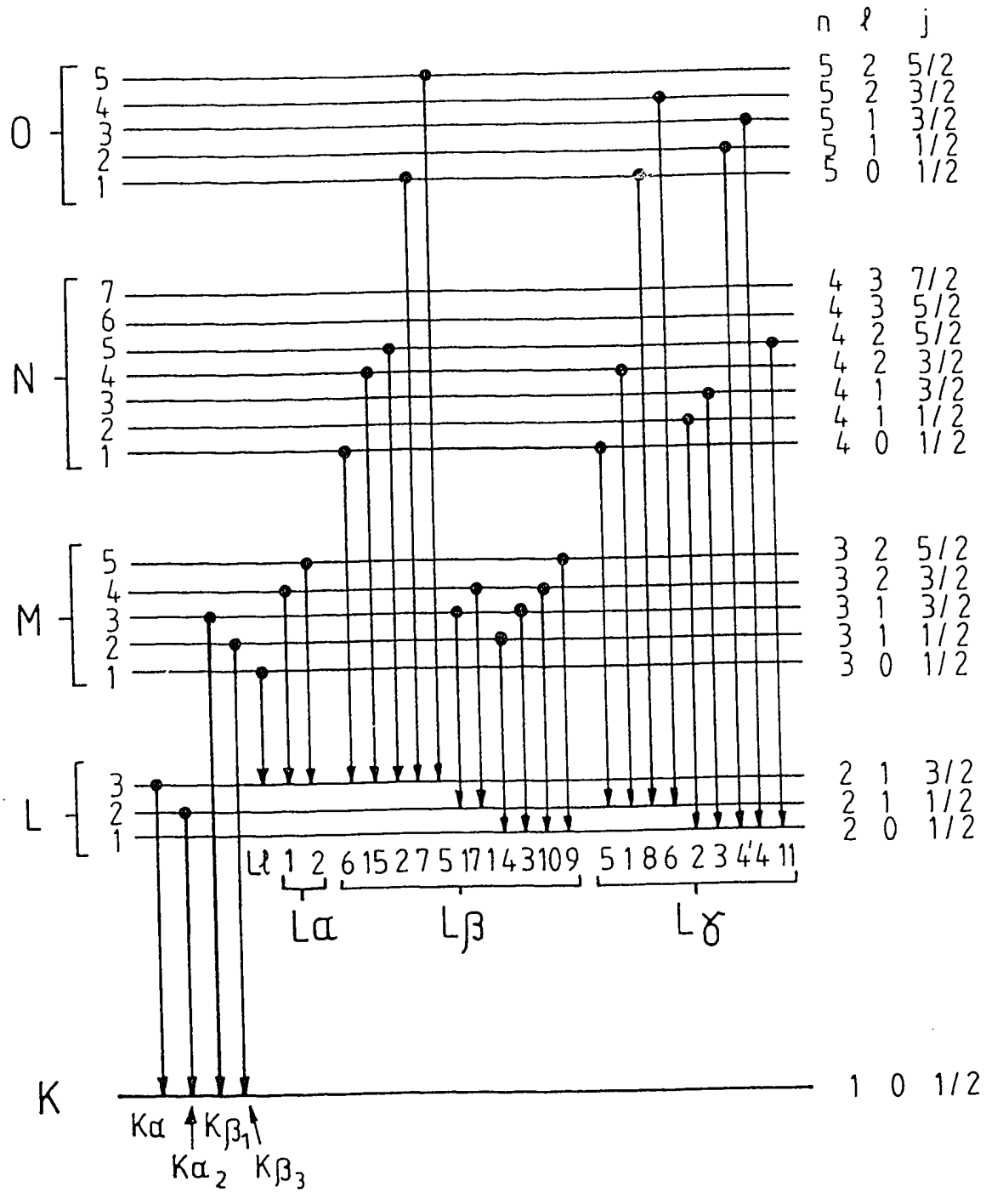
n ℓ j
O
5
4
3
2
1
5 2 5/2
5 2 3/2
5 1 3/2
5 1 1/2
5 0 1/2
N
7
6
5
4
3
2
1
4 3 7/2
4 3 5/2
4 2 5/2
4 2 3/2
4 1 3/2
4 1 1/2
4 0 1/2
M
5
4
3
2
1
3 2 5/2
3 2 3/2
3 1 3/2
3 1 1/2
3 0 1/2
L
3
2
1
2 1 3/2
2 1 1/2
2 0 1/2
Lℓ 1 2 6 15 2 7 5 17 14 3 10 9 5 1 8 6 2 3 4 4 11
Lα
Lβ
Lγ
K
1 0 1/2
Kα
Kβ1
Kα2
Kβ3

Fig. 2

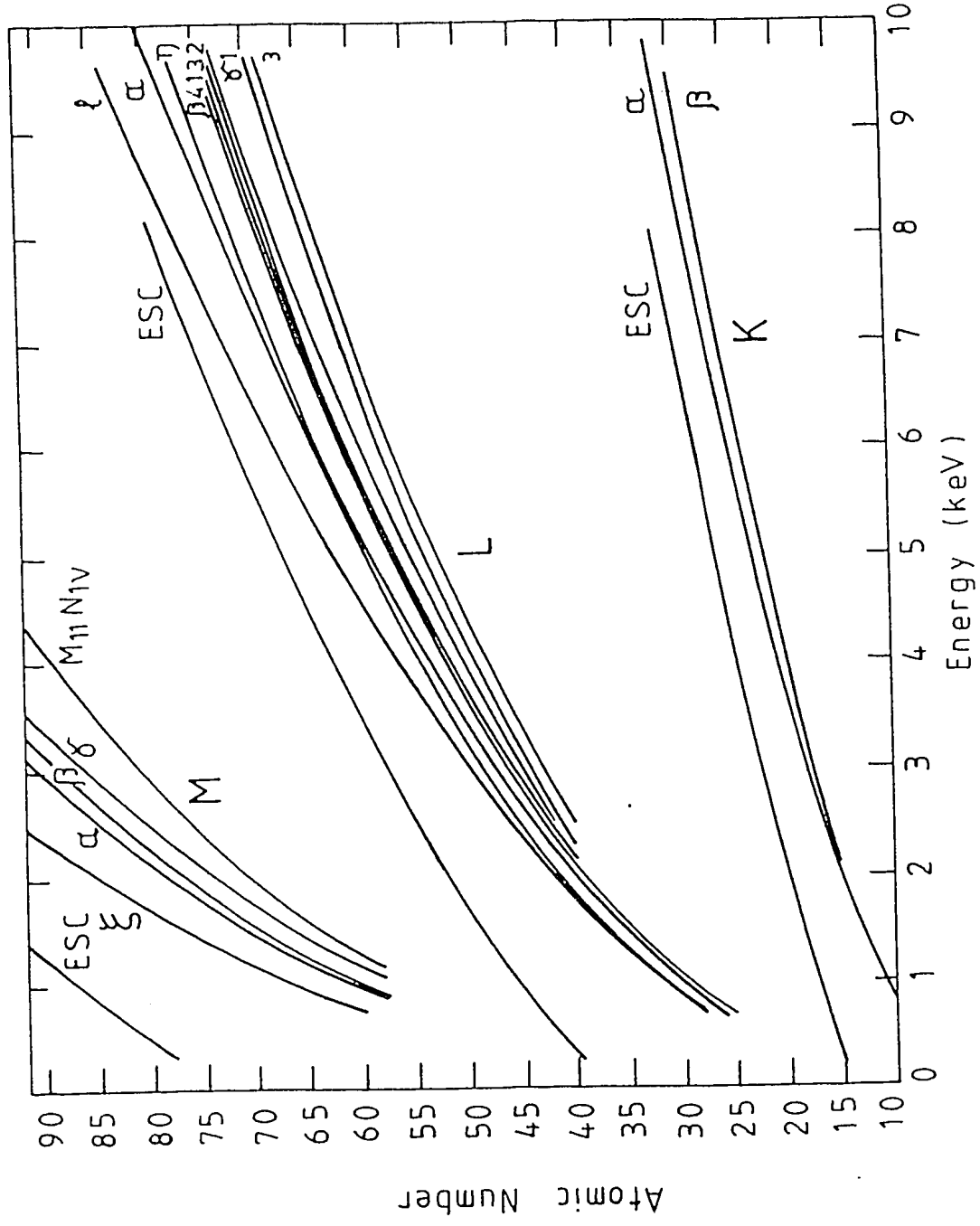
Atomic Number
Energy (keV)
K
L
M
ESC
α
β
ESC
ℓ
α
η
β4132
γ1
3
ESC
ξ
α
β
γ
M11 N1v

Fig. 3

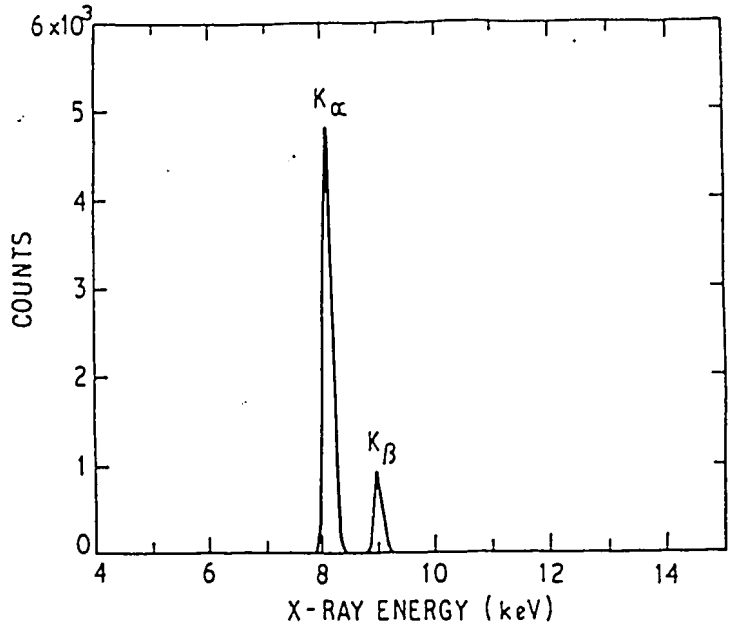

(a) The K X-ray spectrum for Cu showing Kα and Kβ peaks. The Kα: Kβ ratio is approximately 7.

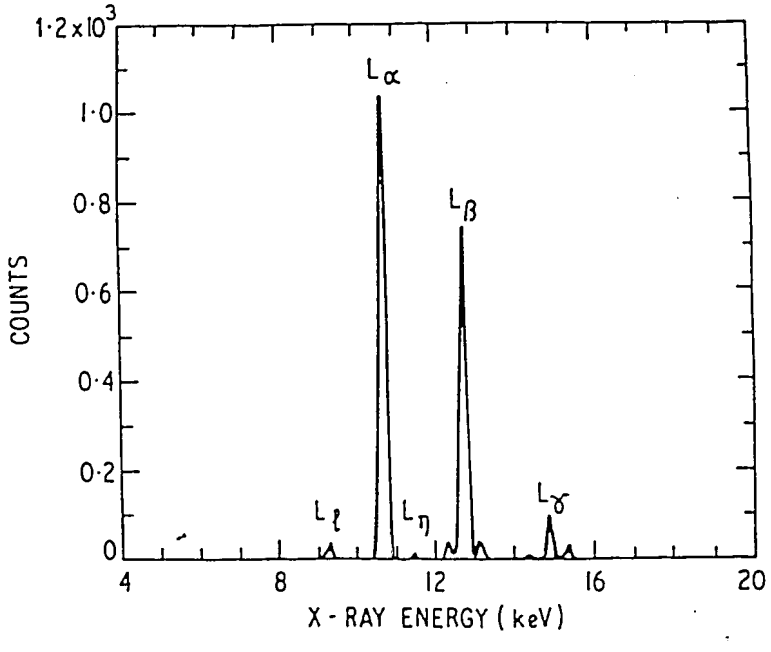

(b) The L transition spectrum for Pb. This is a more complicated spectrum and requires 10 lines to fully characterize it.

Fig. 4

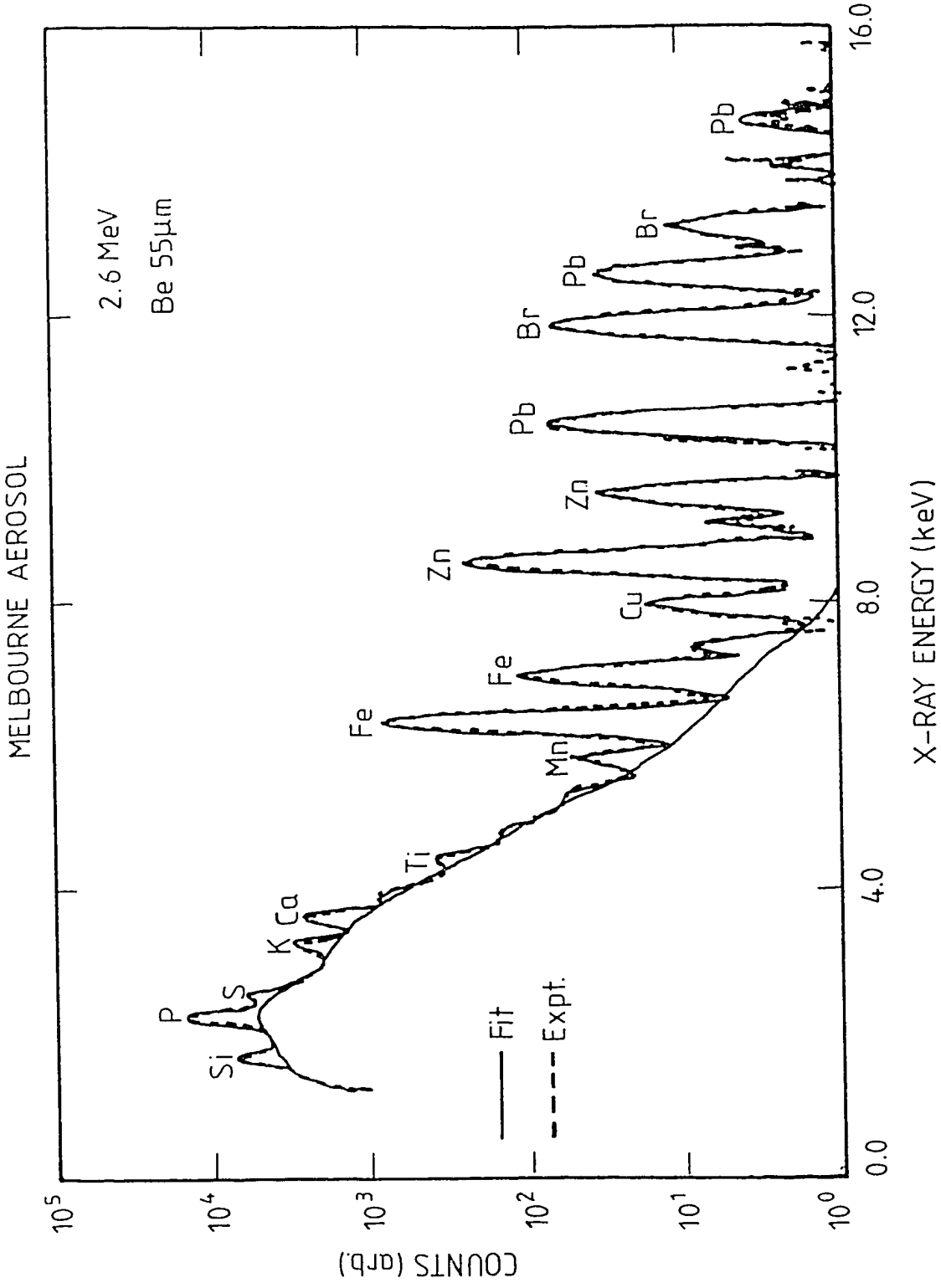
MELBOURNE AEROSOL
2.6 MeV
Be 55µm
Si
P
S
K
Ca
Ti
Mn
Fe
Fe
Cu
Zn
Zn
Pb
Br
Pb
Br
Pb
Fit
Expt.
COUNTS (arb.)
X-RAY ENERGY (keV)
0.0
4.0
8.0
12.0
16.0

Fig. 5

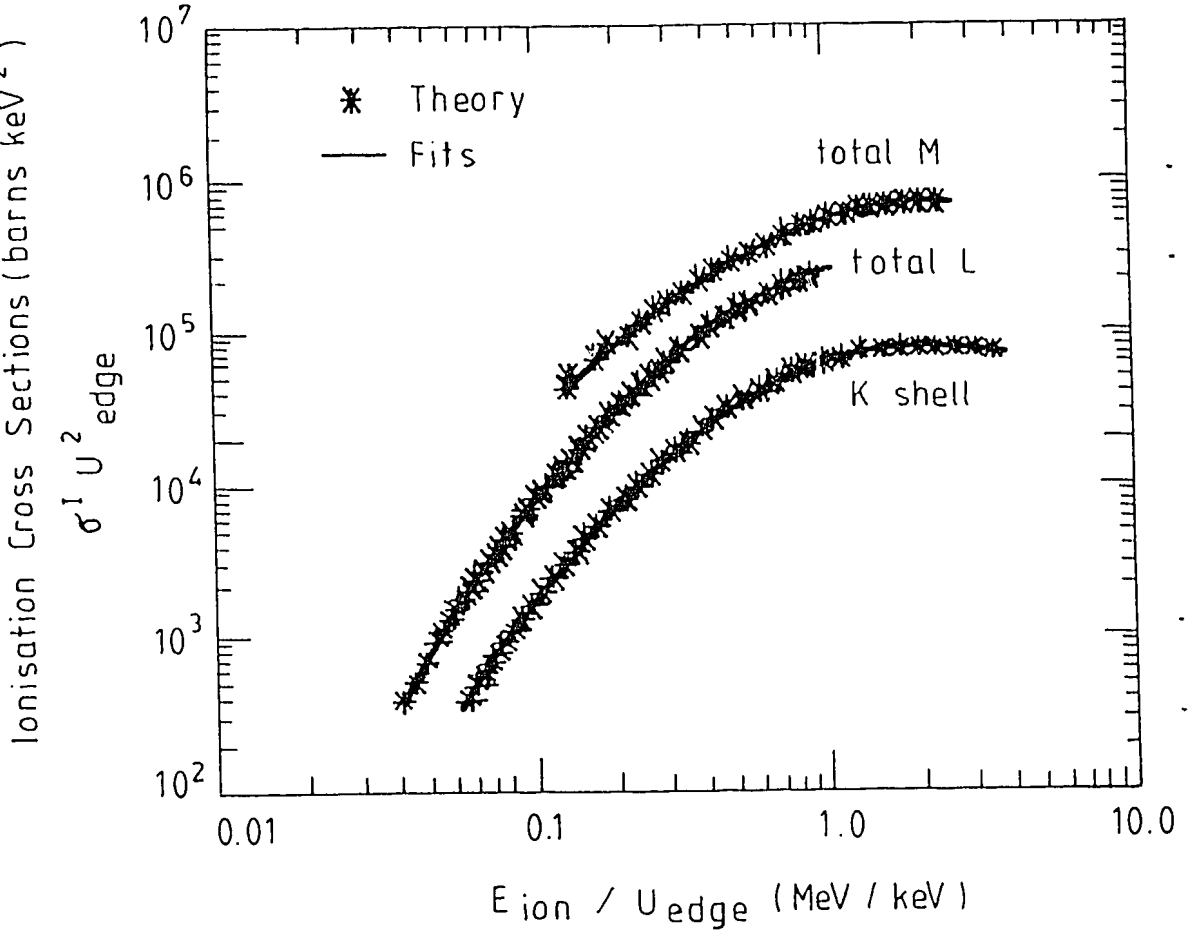
Ionisation Cross Sections (barns keV^2)
$\sigma^1 U^2_{edge}$
10^7
10^6
10^5
10^4
10^3
10^2
Theory
Fits
total M
total L
K shell
0.01
0.1
1.0
10.0
E ion / U edge (MeV / keV)

Fig. 6

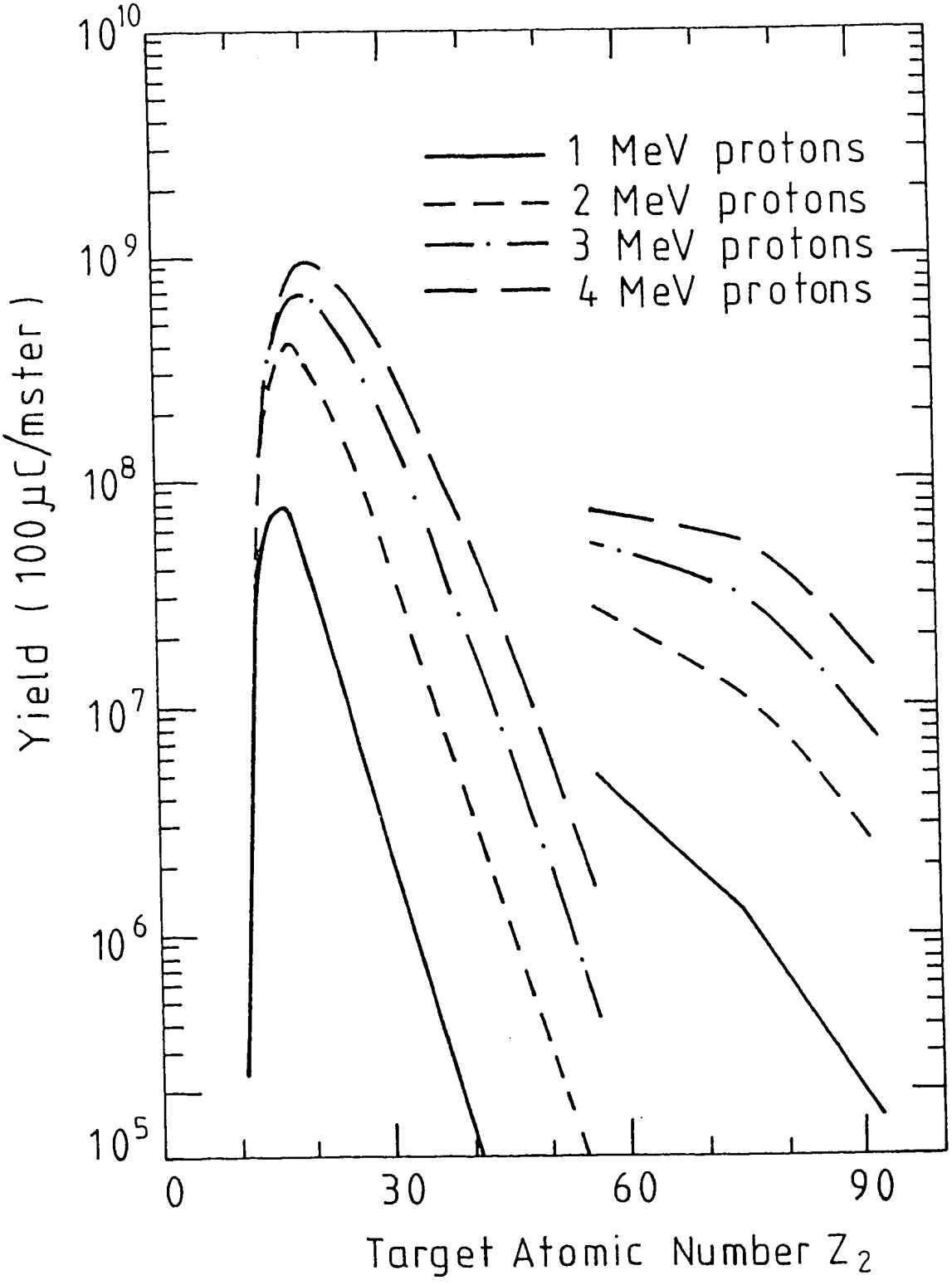
1 MeV protons
2 MeV protons
3 MeV protons
4 MeV protons
Yield (100 µC/mster)
Target Atomic Number Z_2
10^{10}
10^9
10^8
10^7
10^6
10^5
0
30
60
90

Fig. 7

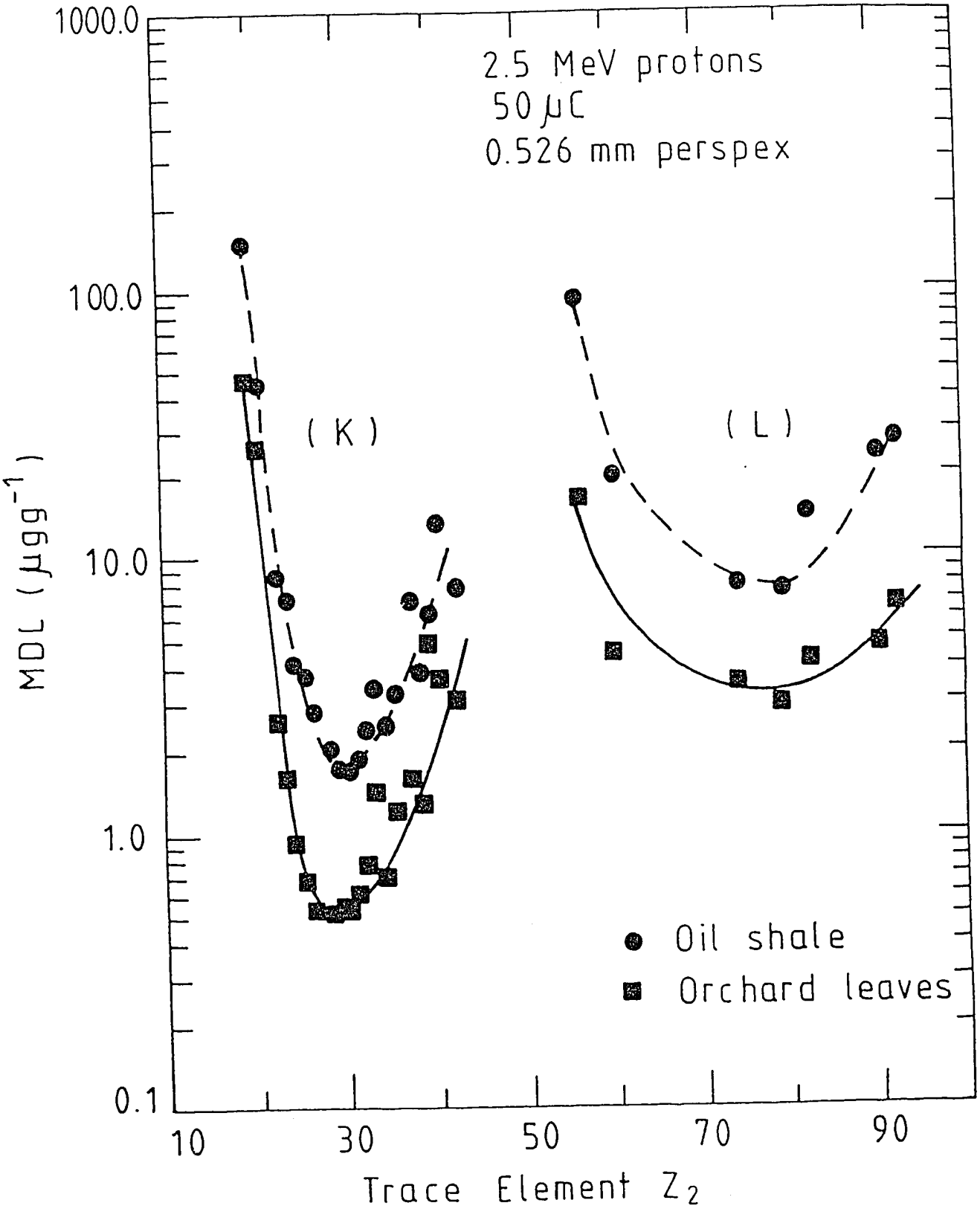
1000.0
100.0
10.0
1.0
0.1
MDL ($\mu g g^{-1}$)
2.5 MeV protons
50 μC
0.526 mm perspex
(K)
(L)
Oil shale
Orchard leaves
10
30
50
70
90
Trace Element Z_2

Fig. 8

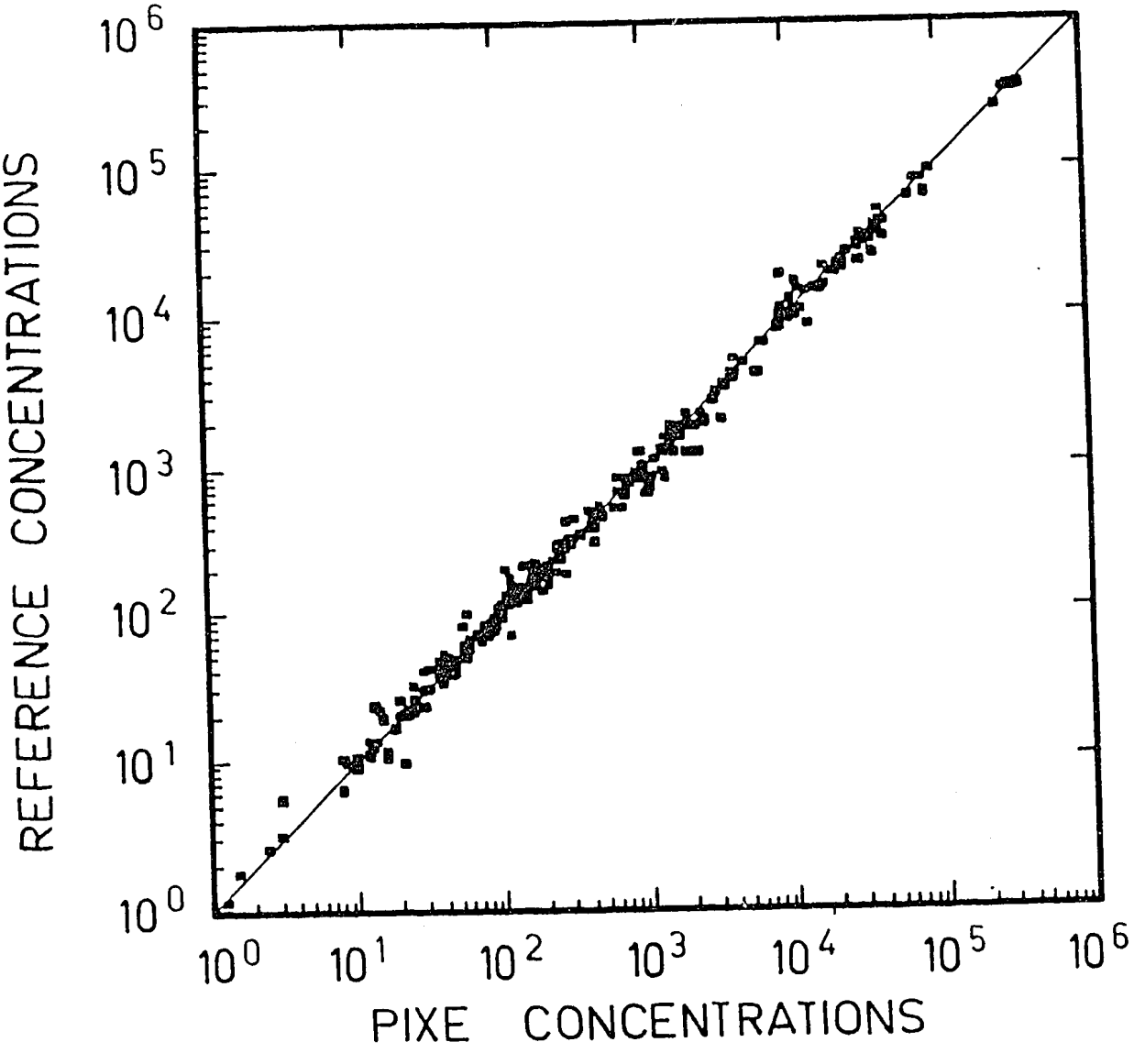
REFERENCE CONCENTRATIONS
10^6
10^5
10^4
10^3
10^2
10^1
10^0
10^0 10^1 10^2 10^3 10^4 10^5 10^6
PIXE CONCENTRATIONS

Fig. 9

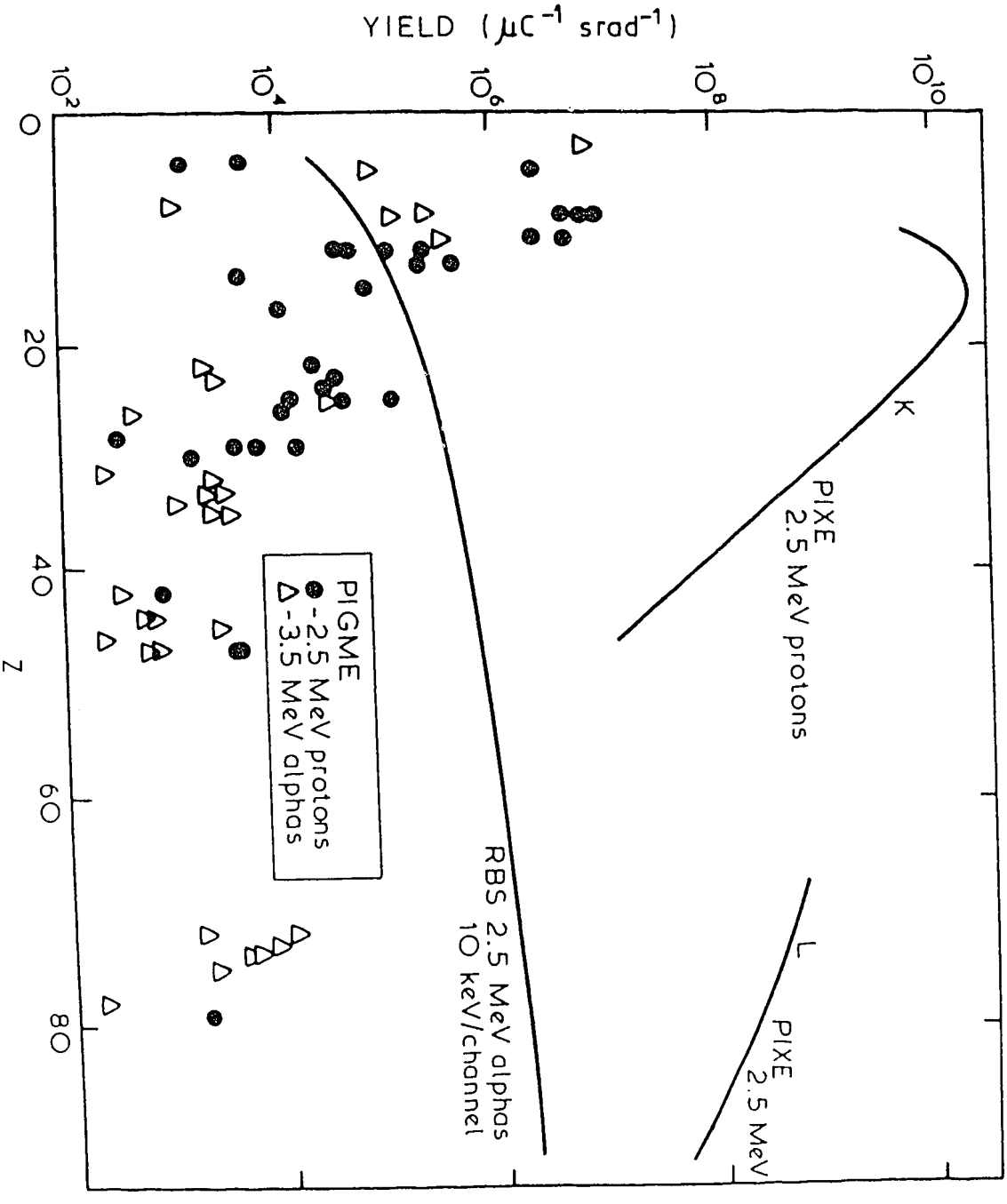
YIELD (μC^{-1} srad^{-1})
10^2
10^4
10^6
10^8
10^{10}
0
20
40
60
80
Z
PIXE
2.5 MeV protons
K
L
PIXE
2.5 MeV
RBS 2.5 MeV alphas
10 keV/channel
PIGME
● -2.5 MeV protons
Δ -3.5 MeV alphas

Fig.10

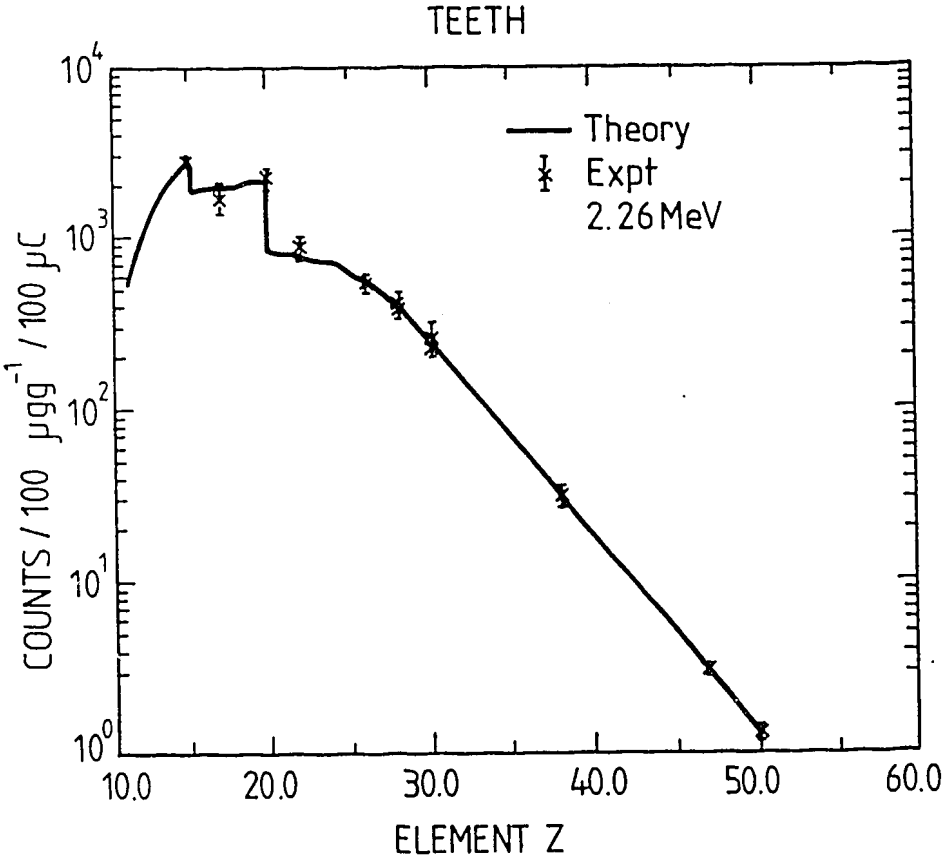
TEETH
Theory
Expt
2.26 MeV
COUNTS / 100 μgg^{-1} / 100 μC
10^4
10^3
10^2
10^1
10^0
10.0
20.0
30.0
40.0
50.0
60.0
ELEMENT Z

Fig. 11

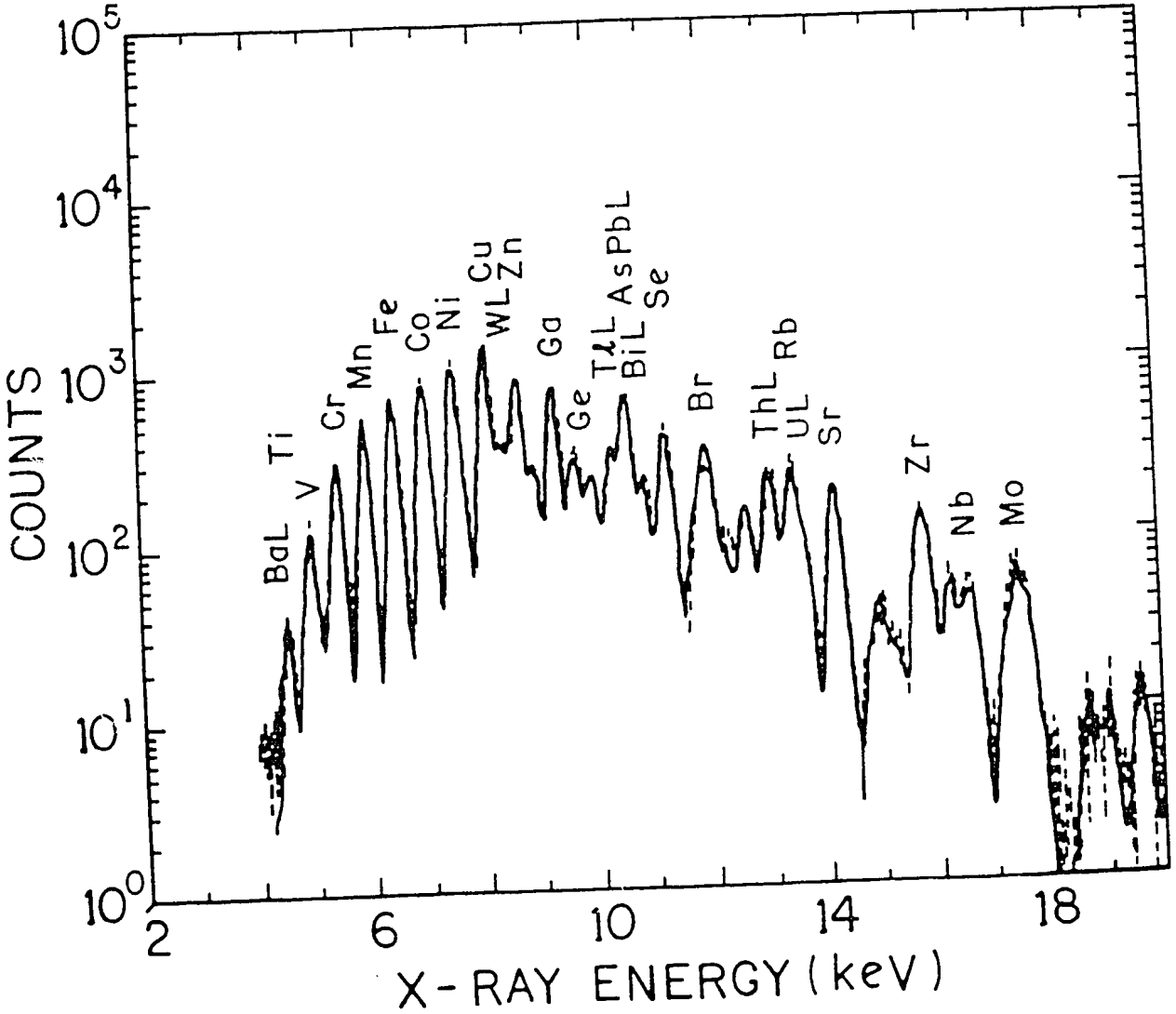
COUNTS
X-RAY ENERGY (keV)
BaL
Ti
V
Cr
Mn
Fe
Co
Ni
Cu
WL
Zn
Ga
Ge
TiL
BiL
As
PbL
Se
Br
ThL
UL
Rb
Sr
Zr
Nb
Mo

Fig. 12

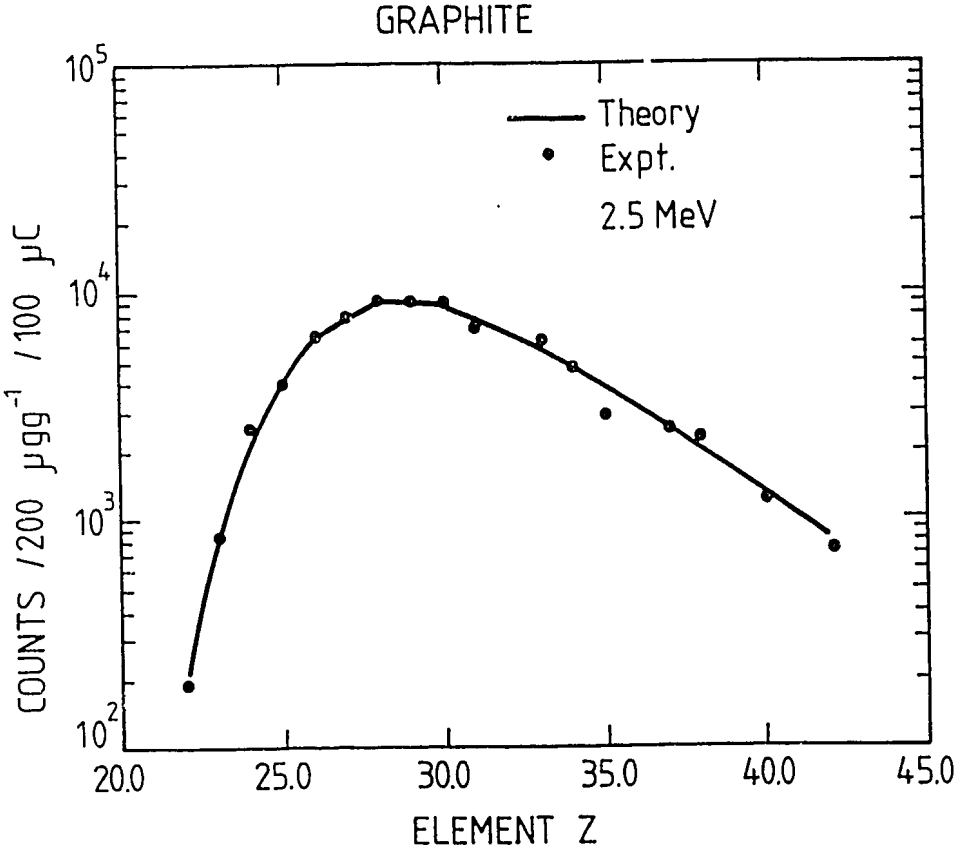
GRAPHITE
Theory
Expt.
2.5 MeV
COUNTS /200 μgg⁻¹ /100 μC
10⁵
10⁴
10³
10²
20.0
25.0
30.0
35.0
40.0
45.0
ELEMENT Z

Fig. 13

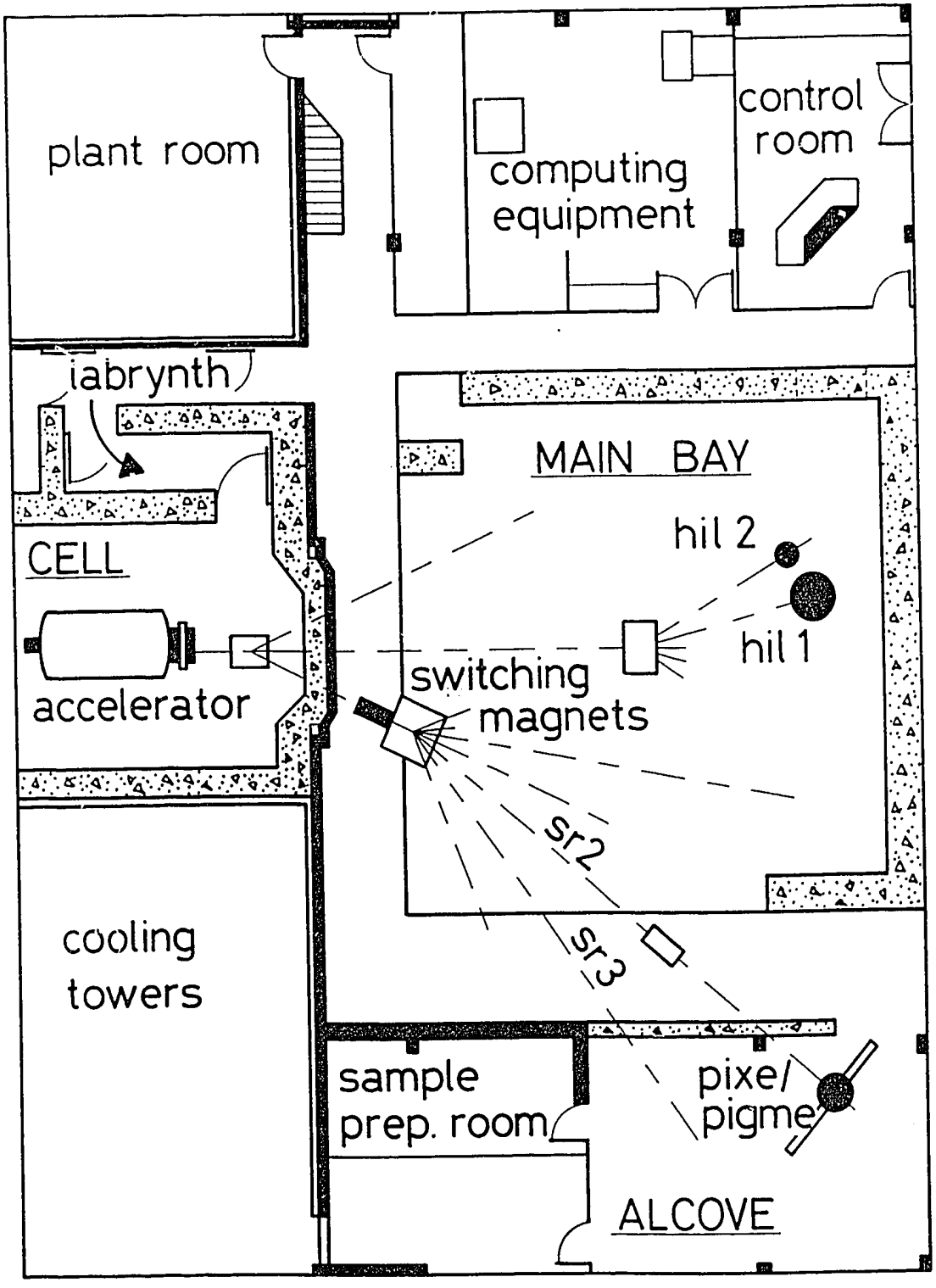
plant room
computing equipment
control room
iabrynth
MAIN BAY
CELL
hil 2
hil 1
accelerator
switching magnets
sr2
sr3
cooling towers
sample prep. room
pixe/ pigme
ALCOVE

Fig. 14

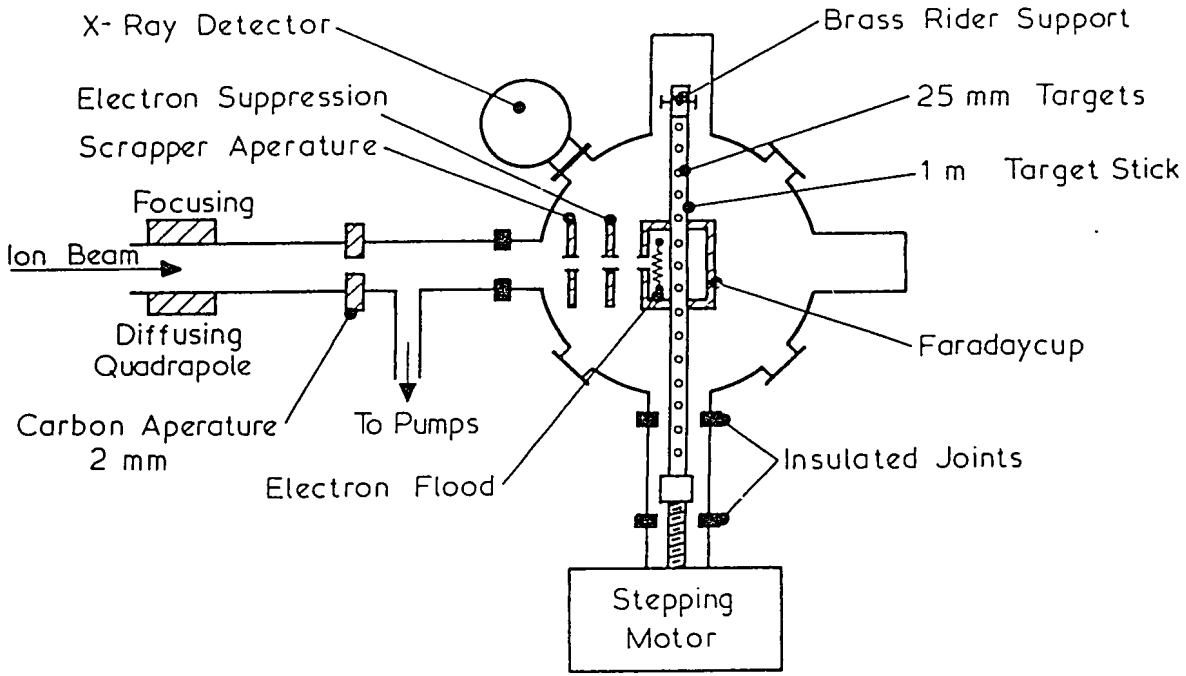
X- Ray Detector
Brass Rider Support
Electron Suppression
25 mm Targets
Scrapper Aperature
1 m Target Stick
Focusing
Ion Beam
Diffusing
Quadrapole
Faradaycup
Carbon Aperature
2 mm
To Pumps
Insulated Joints
Electron Flood
Stepping
Motor

Fig. 15

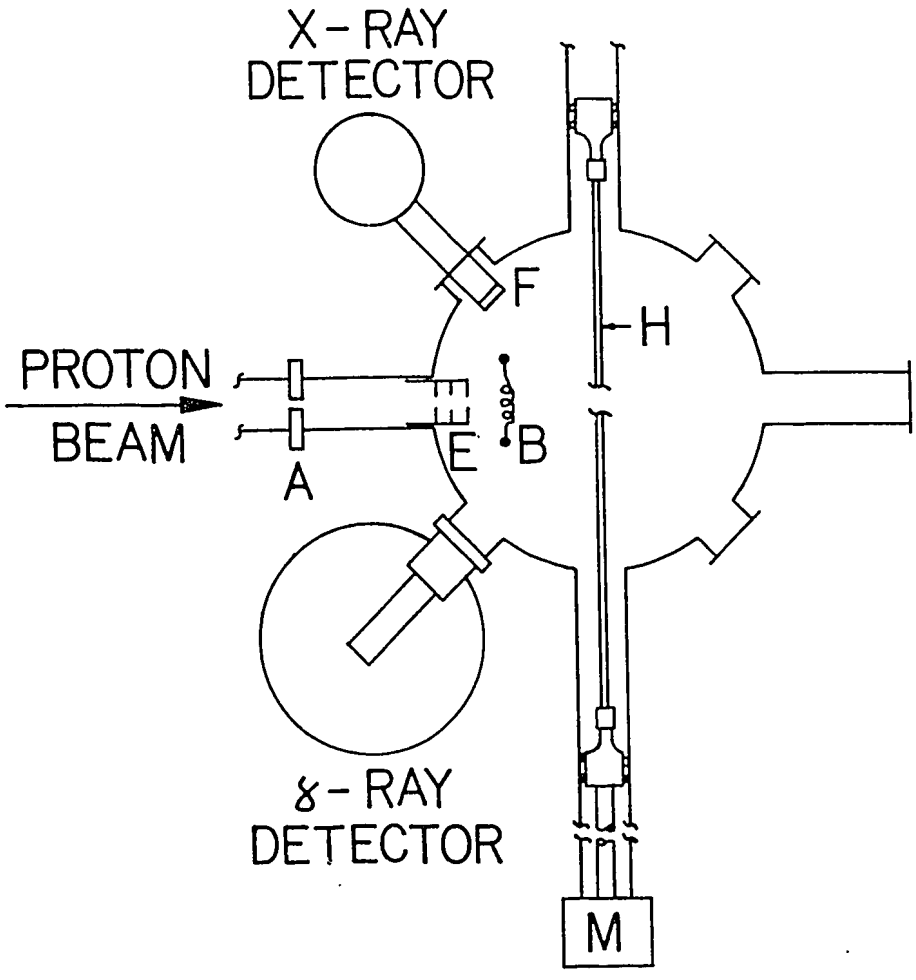
X-RAY
DETECTOR
F
H
PROTON
BEAM
A
E
B
γ-RAY
DETECTOR
M

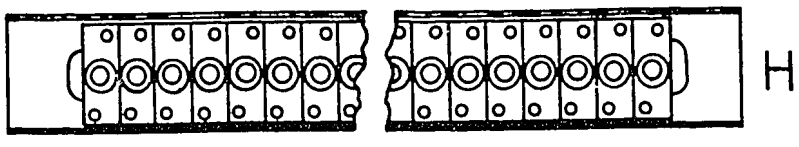
H

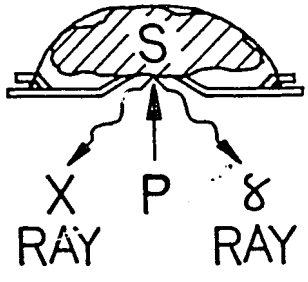
S
X
RAY
P
γ
RAY

Fig. 16

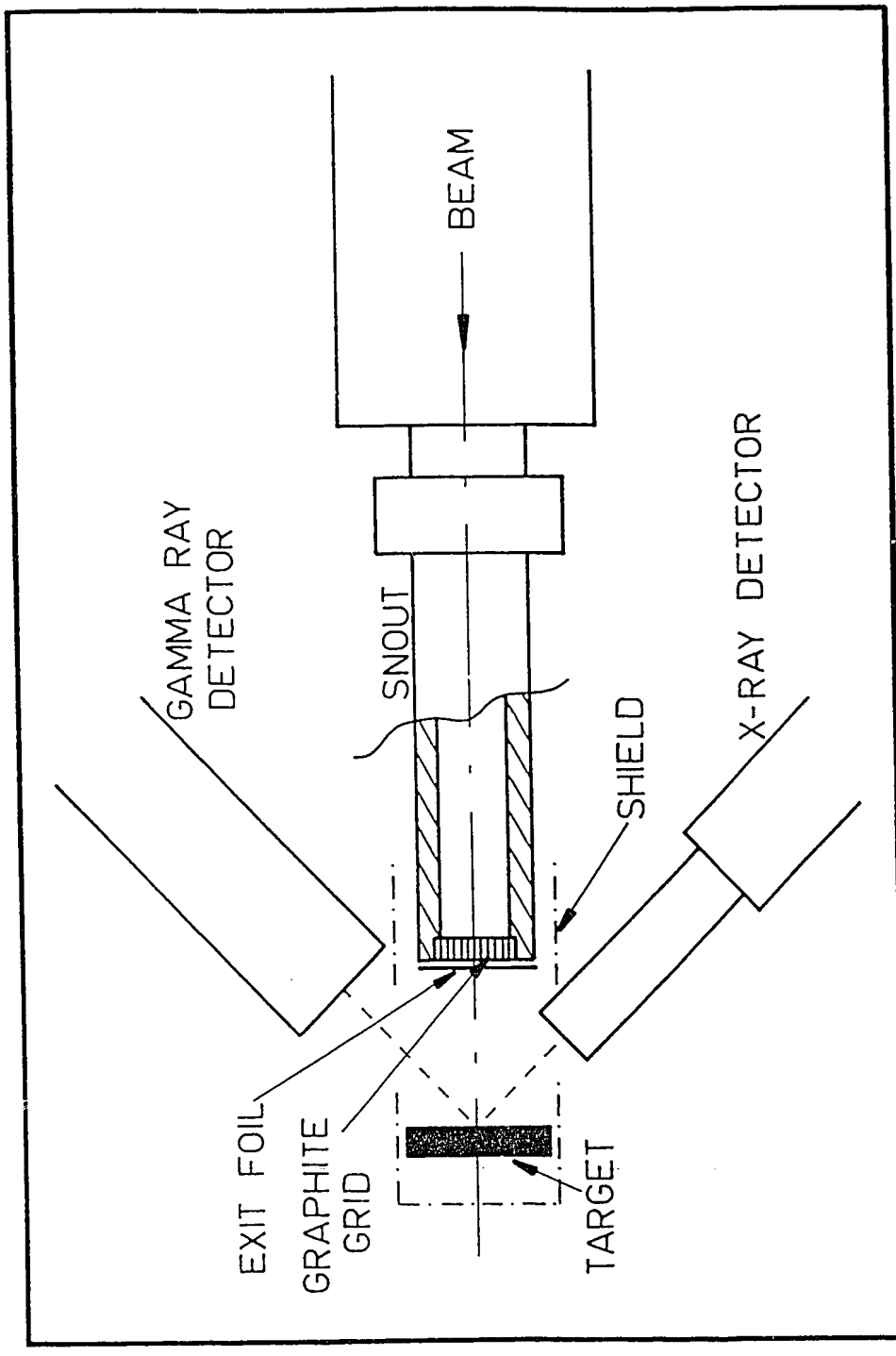
BEAM
GAMMA RAY DETECTOR
SNOUT
SHIELD
X-RAY DETECTOR
EXIT FOIL
GRAPHITE GRID
TARGET

Fig. 17

(a)

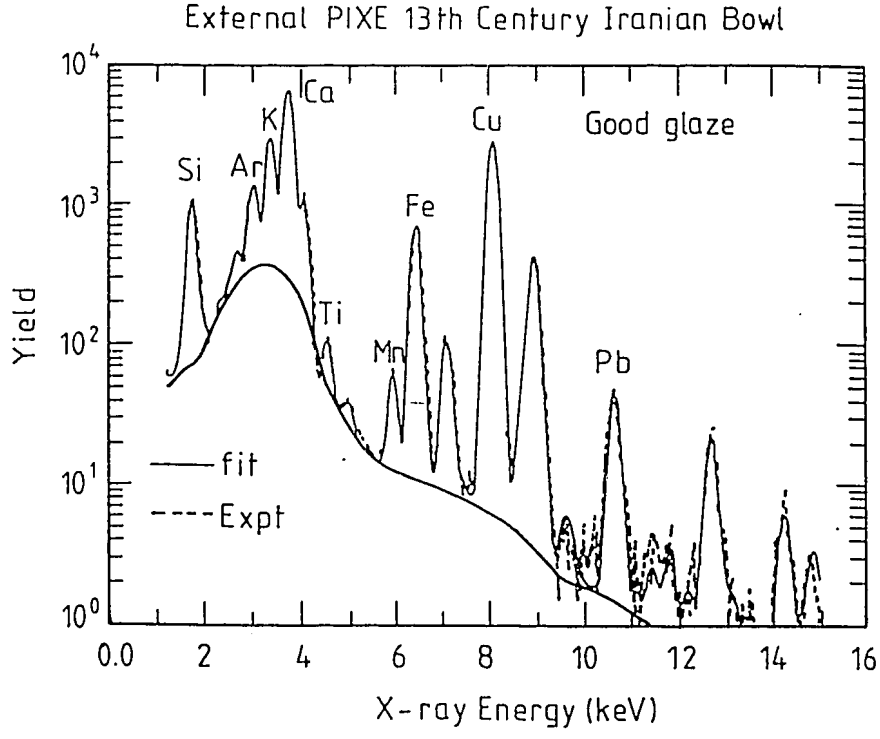
External PIXE 13th Century Iranian Bowl
Good glaze
Si
Ar
K
Ca
Ti
Mn
Fe
Cu
Pb
fit
Expt
Yield
X-ray Energy (keV)

(b)

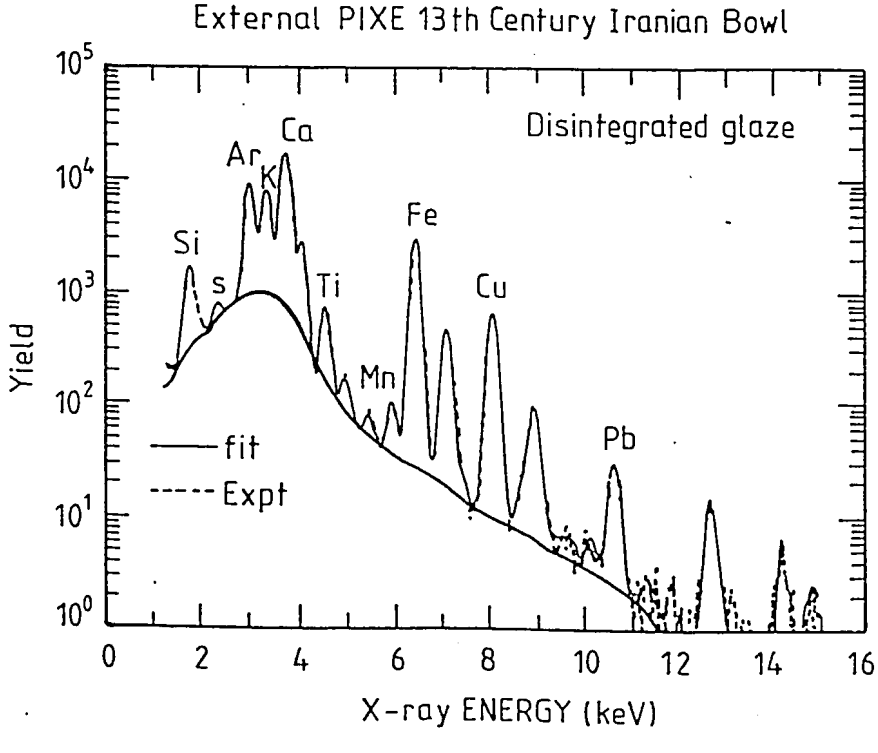
External PIXE 13th Century Iranian Bowl
Disintegrated glaze
Si
S
Ar
K
Ca
Ti
Mn
Fe
Cu
Pb
fit
Expt
Yield
X-ray ENERGY (keV)

Fig. 18

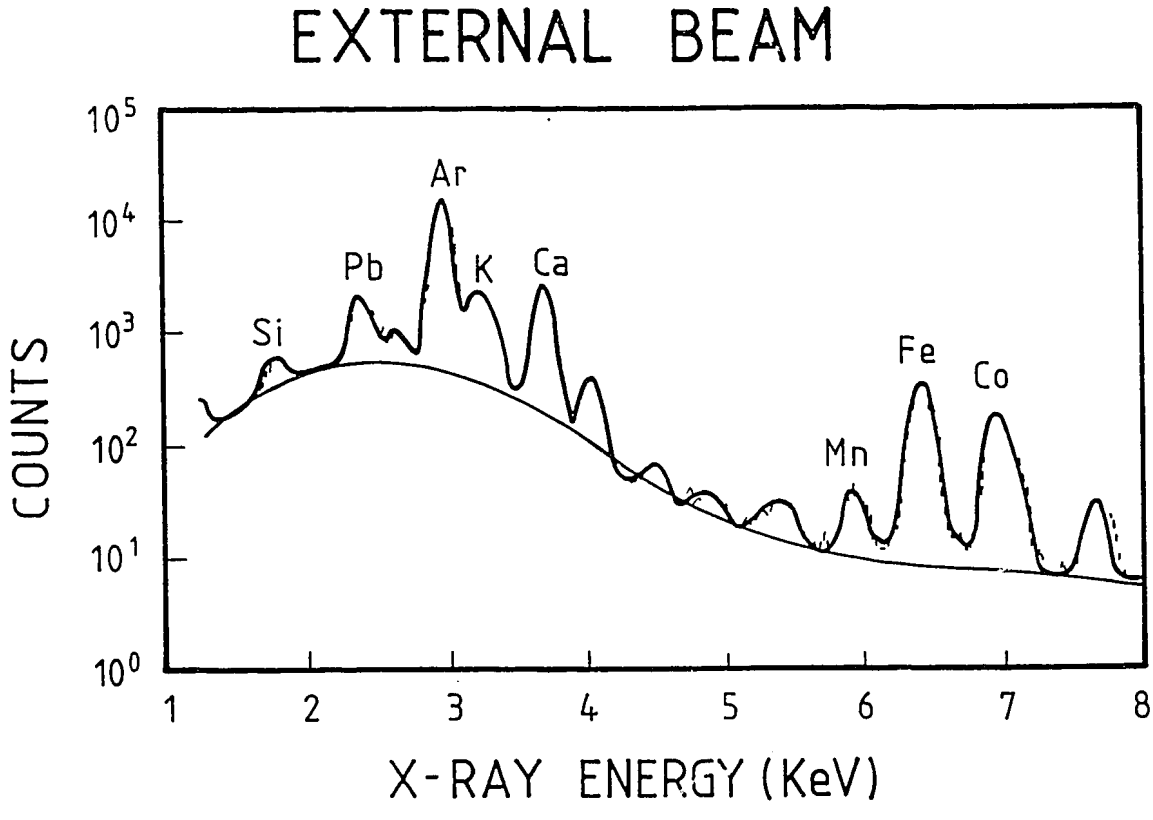
EXTERNAL BEAM
COUNTS
10^5
10^4
10^3
10^2
10^1
10^0
Si
Pb
Ar
K
Ca
Mn
Fe
Co
1
2
3
4
5
6
7
8
X-RAY ENERGY (KeV)

Fig. 19

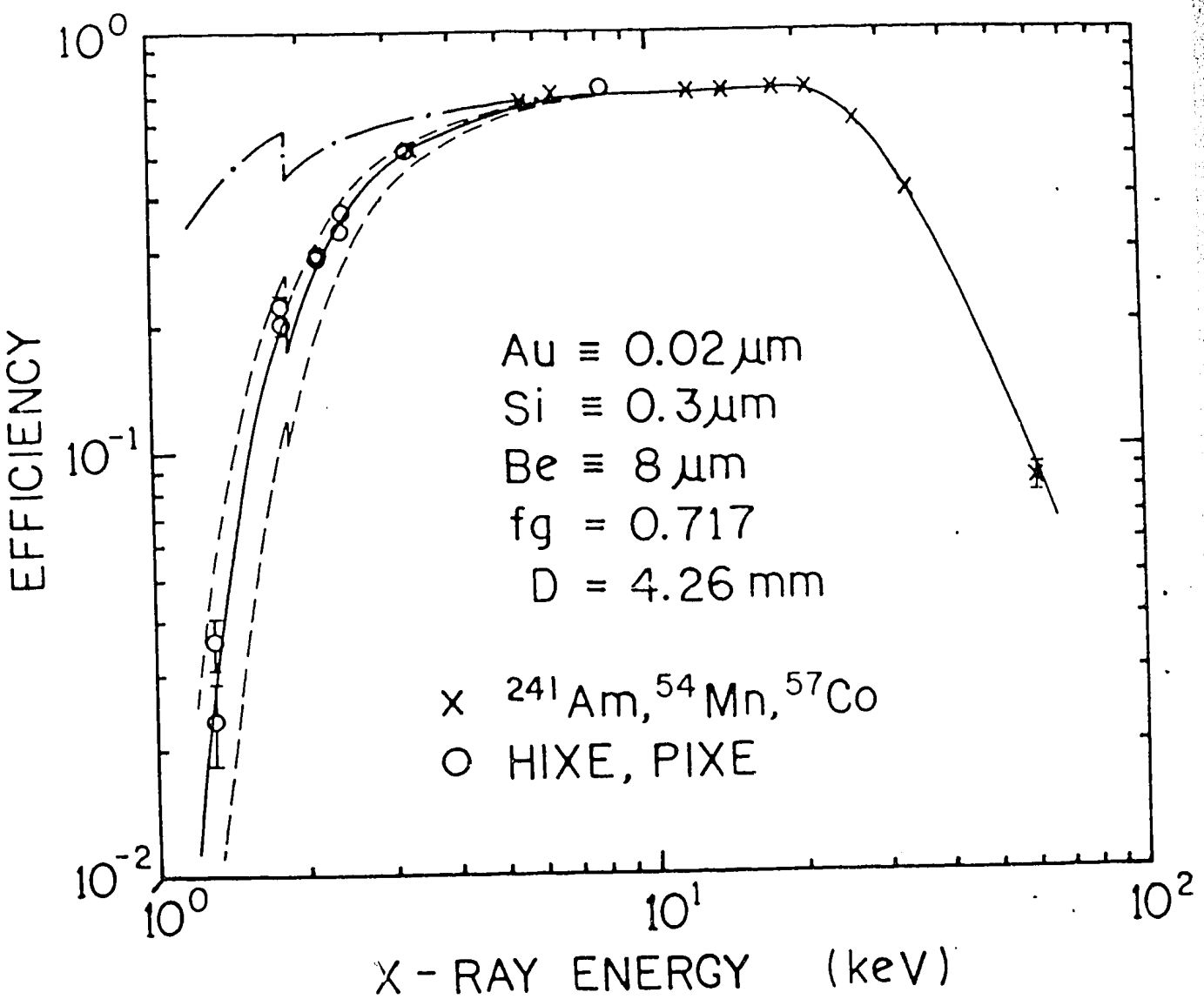
EFFICIENCY
10^0
10^{-1}
10^{-2}
10^0
10^1
10^2
X - RAY ENERGY (keV)
Au ≡ 0.02 μm
Si ≡ 0.3 μm
Be ≡ 8 μm
fg = 0.717
D = 4.26 mm
x ^{241}Am, ^{54}Mn, ^{57}Co
o HIXE, PIXE

Fig. 20

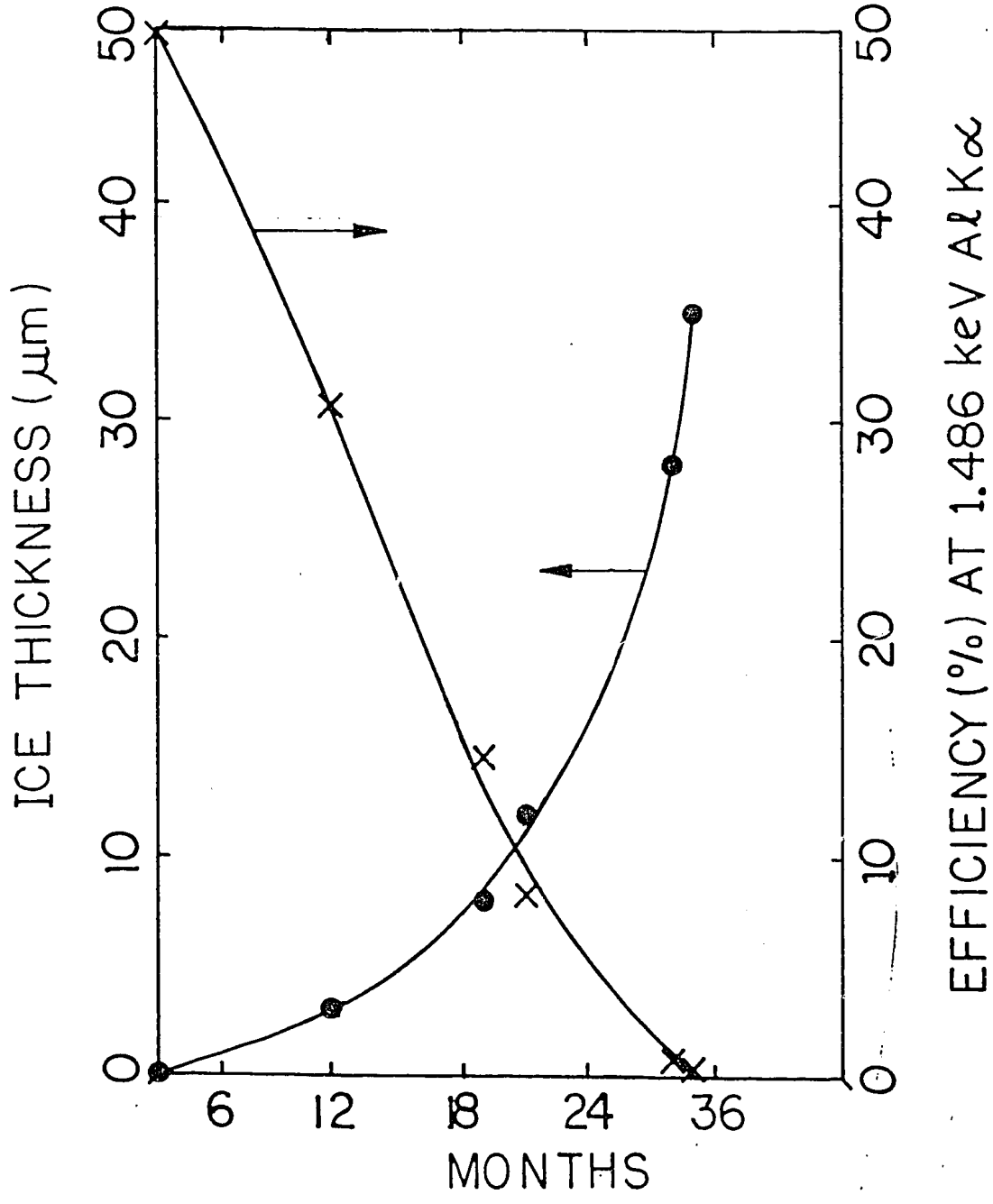
ICE THICKNESS (μm)
EFFICIENCY (%) AT 1.486 keV Al Kα
MONTHS
0
10
20
30
40
50
6
12
18
24
36

Fig. 21

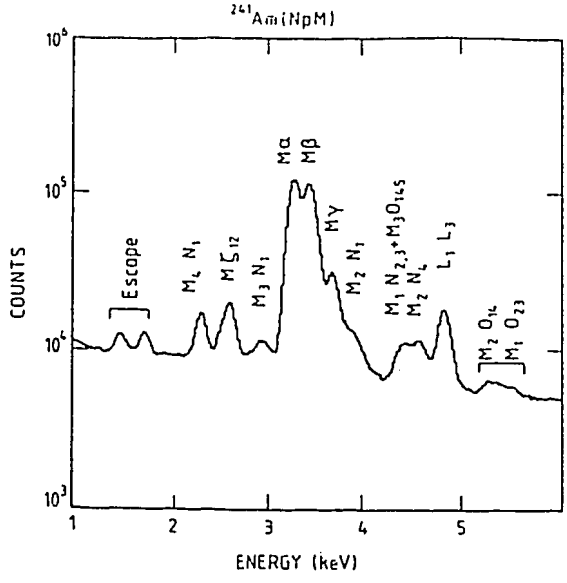
^{241}Am(NpM)
COUNTS
ENERGY (keV)
Escape
$M_4 N_1$
$M\zeta_{12}$
$M_3 N_1$
Mα
Mβ
MY
$M_2 N_1$
$M_1 N_{2,3} + M_3 O_{145}$
$M_2 N_4$
$L_1 L_3$
$M_2 O_{14}$
$M_1 O_{23}$

(a)

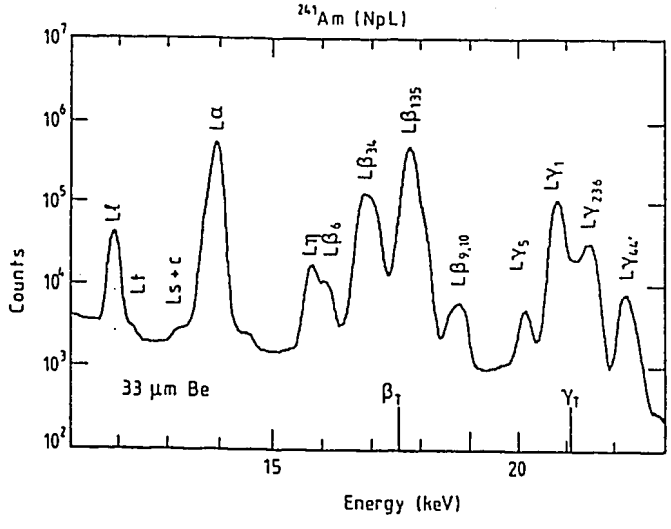
^{241}Am (NpL)
Counts
Energy (keV)
Lℓ
Lf
Ls+c
Lα
Lη
$L\beta_6$
$L\beta_{34}$
$L\beta_{135}$
$L\beta_{9,10}$
LY_5
LY_1
LY_{236}
$LY_{4,4'}$
33 µm Be
β_T
γ_T

(b)

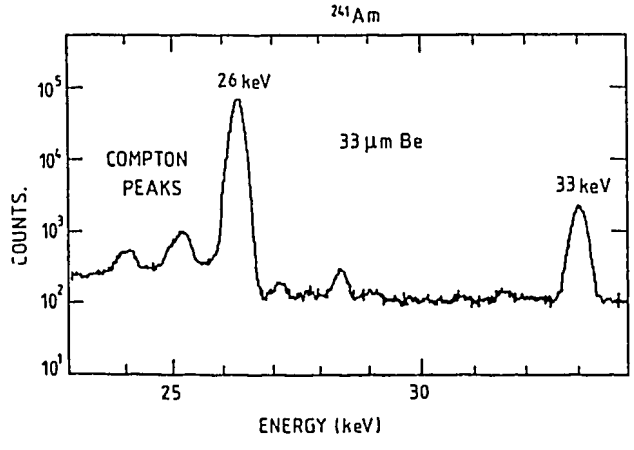
^{241}Am
COUNTS.
ENERGY (keV)
26 keV
33 µm Be
COMPTON
PEAKS
33 keV

(c)

Fig. 22

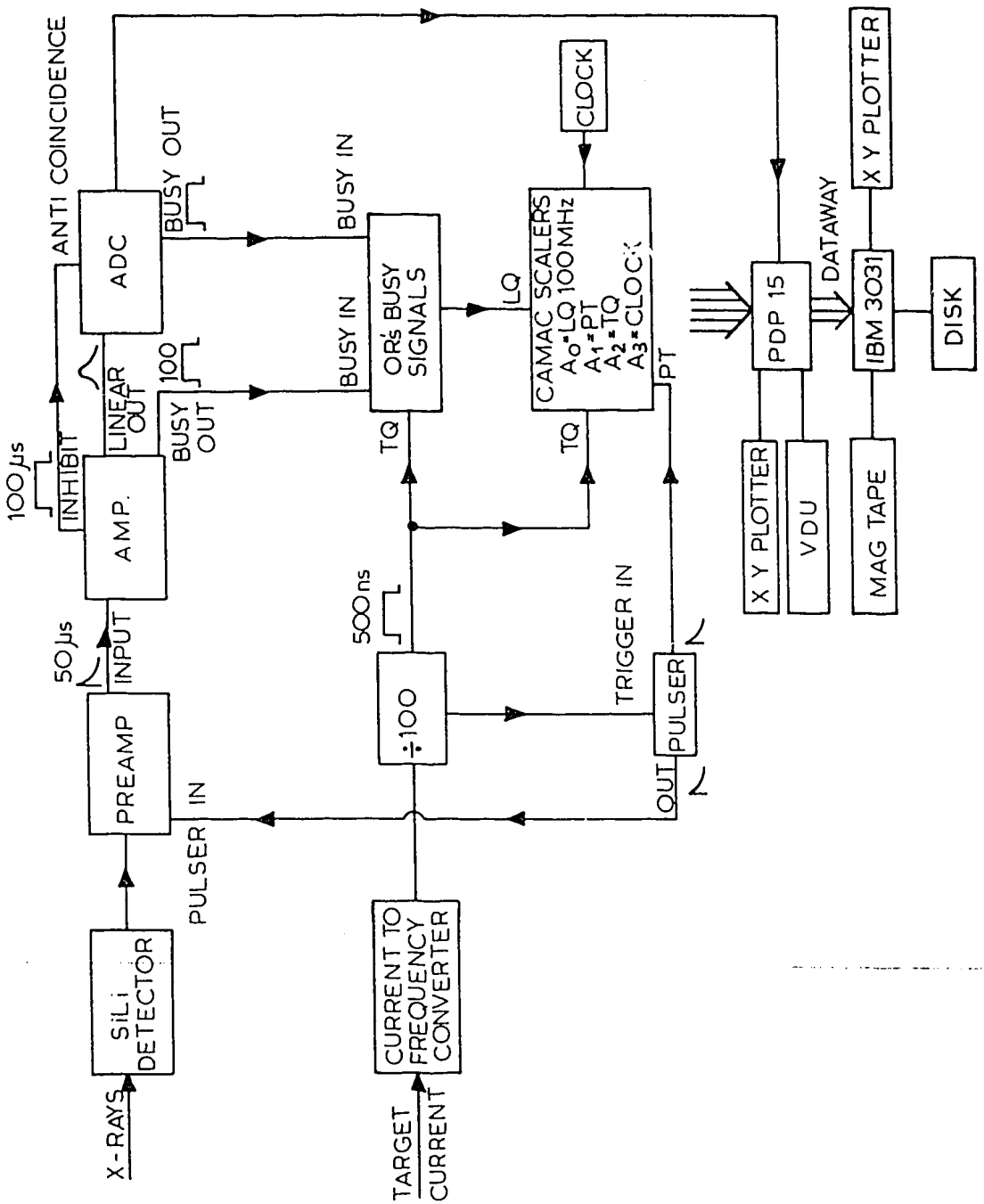
X-RAYS
Si(Li) DETECTOR
PREAMP
50 µs
INPUT
PULSER IN
AMP.
100 µs
INHIBIT
LINEAR OUT
BUSY OUT
ANTI COINCIDENCE
ADC
BUSY OUT
100
BUSY IN
BUSY IN
ORs BUSY SIGNALS
LQ
CAMAC SCALERS
A0=LQ 100 MHz
A1=PT
A2=TQ
A3=CLOCK
CLOCK
PT
TQ
TQ
500 ns
÷100
TRIGGER IN
PULSER
OUT
TARGET CURRENT
CURRENT TO FREQUENCY CONVERTER
PDP 15
DATAWAY
X Y PLOTTER
IBM 3031
DISK
X Y PLOTTER
VDU
MAG TAPE

Fig. 23

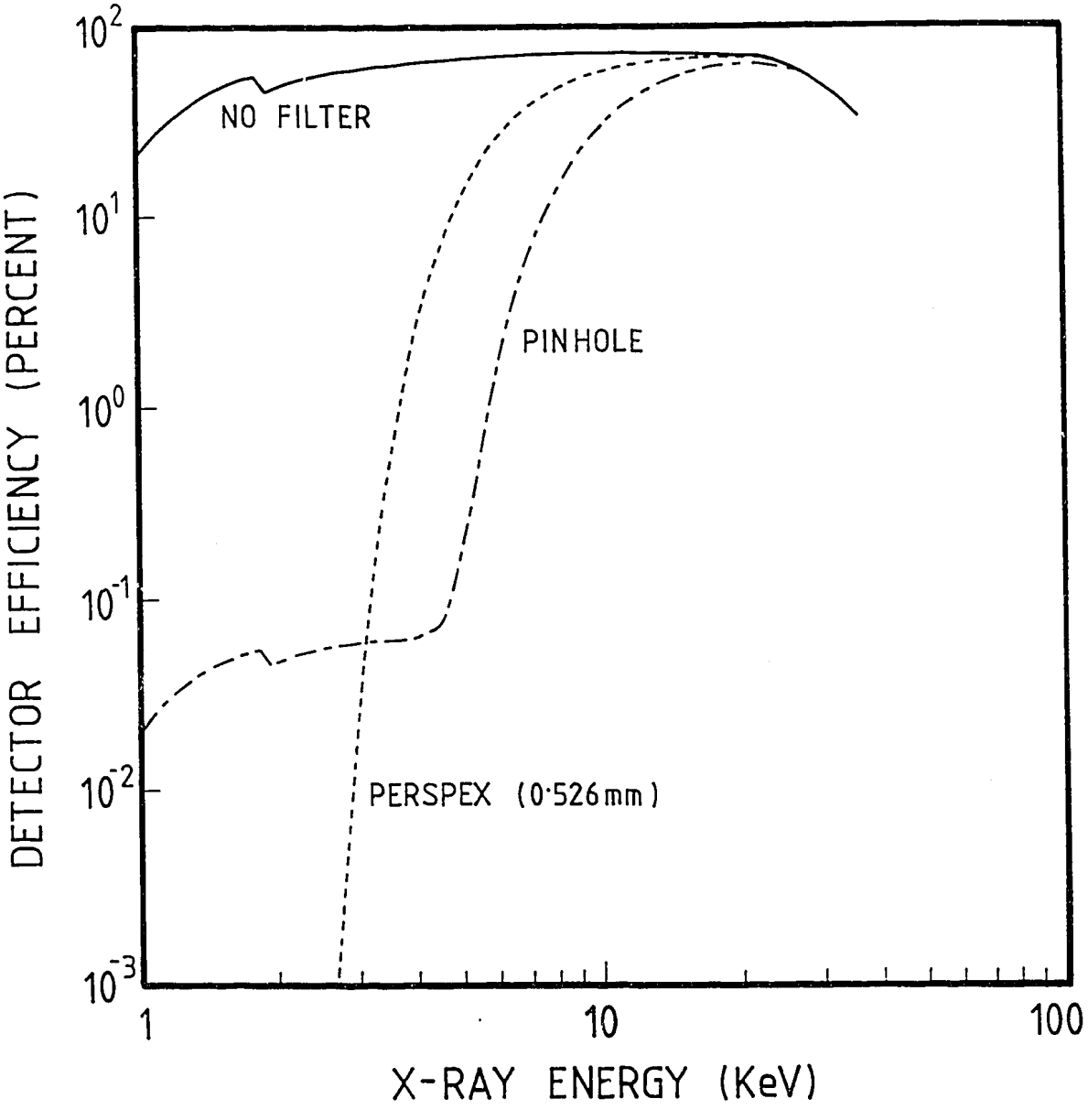
10^2
10^1
10^0
10^{-1}
10^{-2}
10^{-3}
DETECTOR EFFICIENCY (PERCENT)
NO FILTER
PINHOLE
PERSPEX (0·526mm)
1
10
100
X-RAY ENERGY (KeV)

Fig. 24

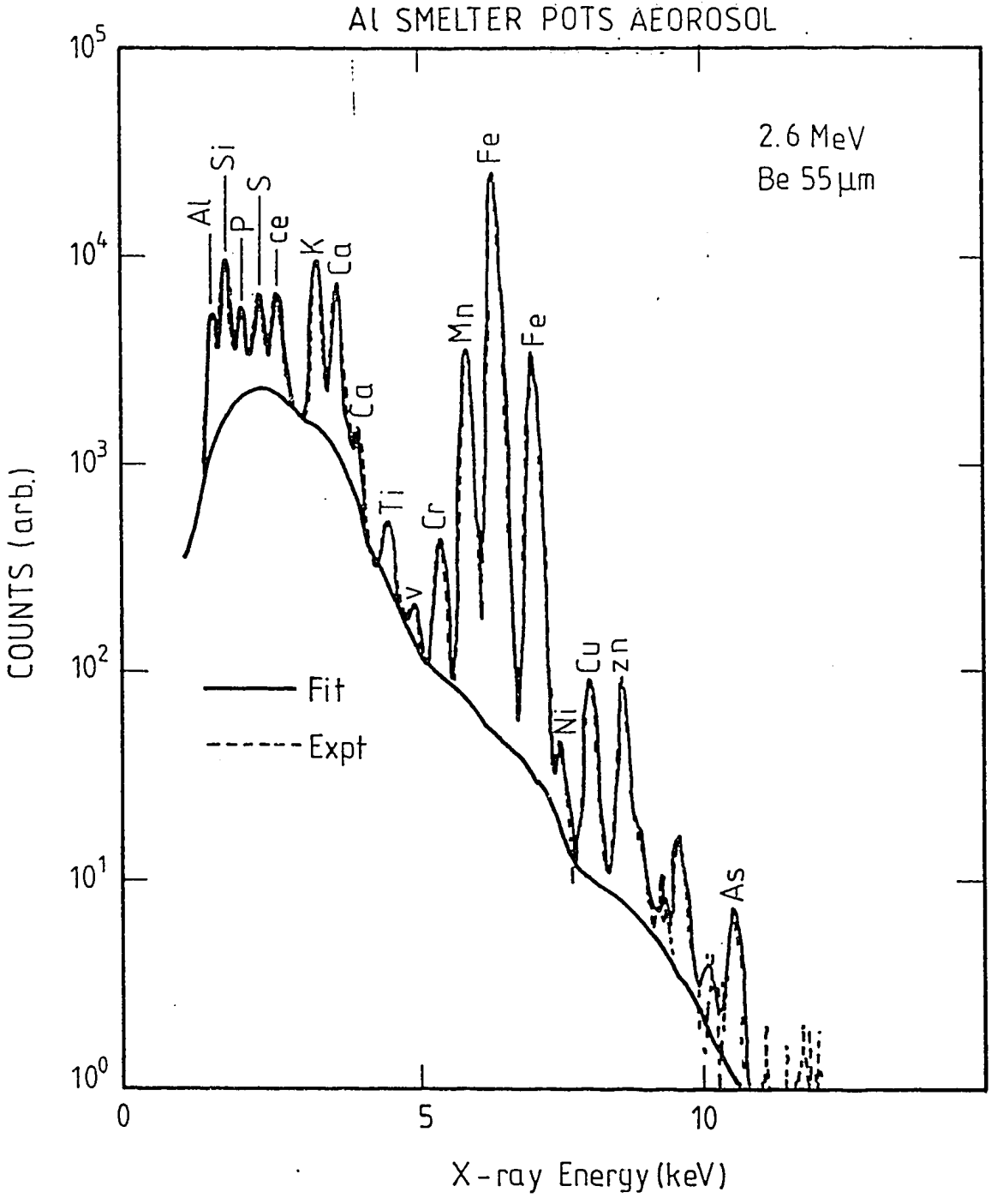
Al SMELTER POTS AEOROSOL
2.6 MeV
Be 55 µm
COUNTS (arb.)
X-ray Energy (keV)
Fit
Expt
Al
Si
P
S
Cl
K
Ca
Ca
Ti
V
Cr
Mn
Fe
Fe
Ni
Cu
Zn
As
10^5
10^4
10^3
10^2
10^1
10^0
0
5
10

Fig. 25

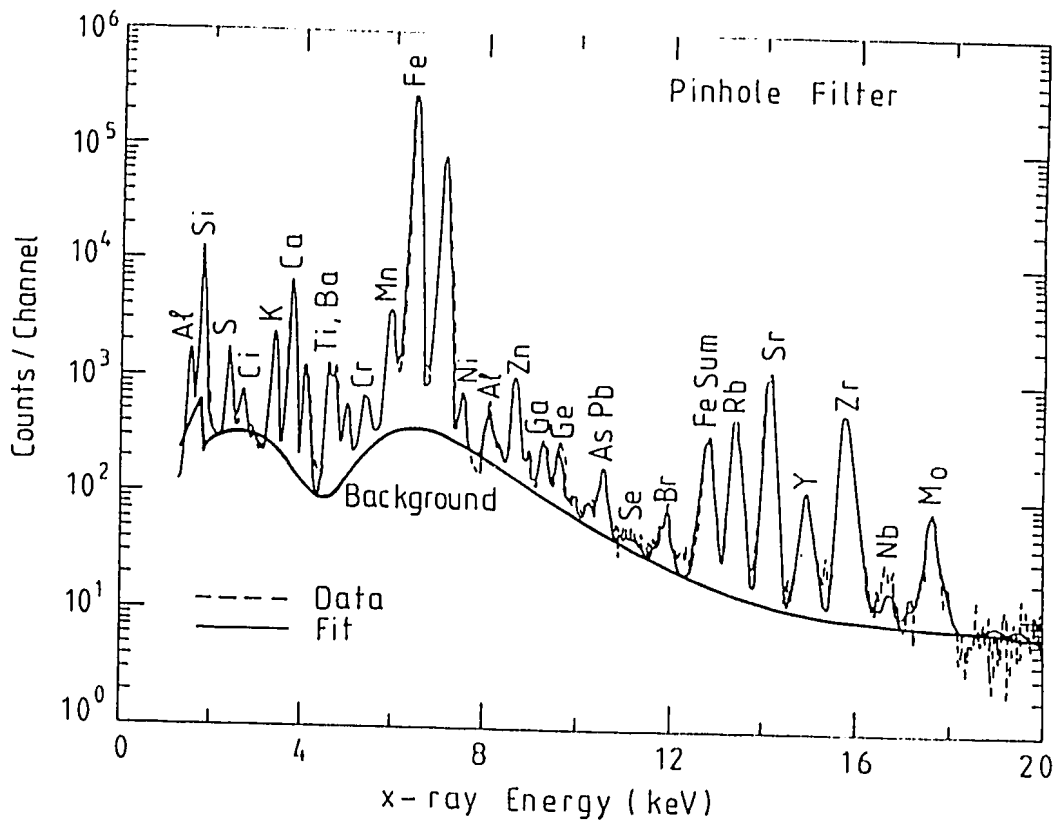
Pinhole Filter
Counts / Channel
x-ray Energy (keV)
Background
Data
Fit
Al
Si
S
Cl
K
Ca
Ti, Ba
Cr
Mn
Fe
Ni
Al
Zn
Ga
Ge
As Pb
Se
Br
Fe Sum
Rb
Sr
Y
Zr
Nb
Mo
(a)

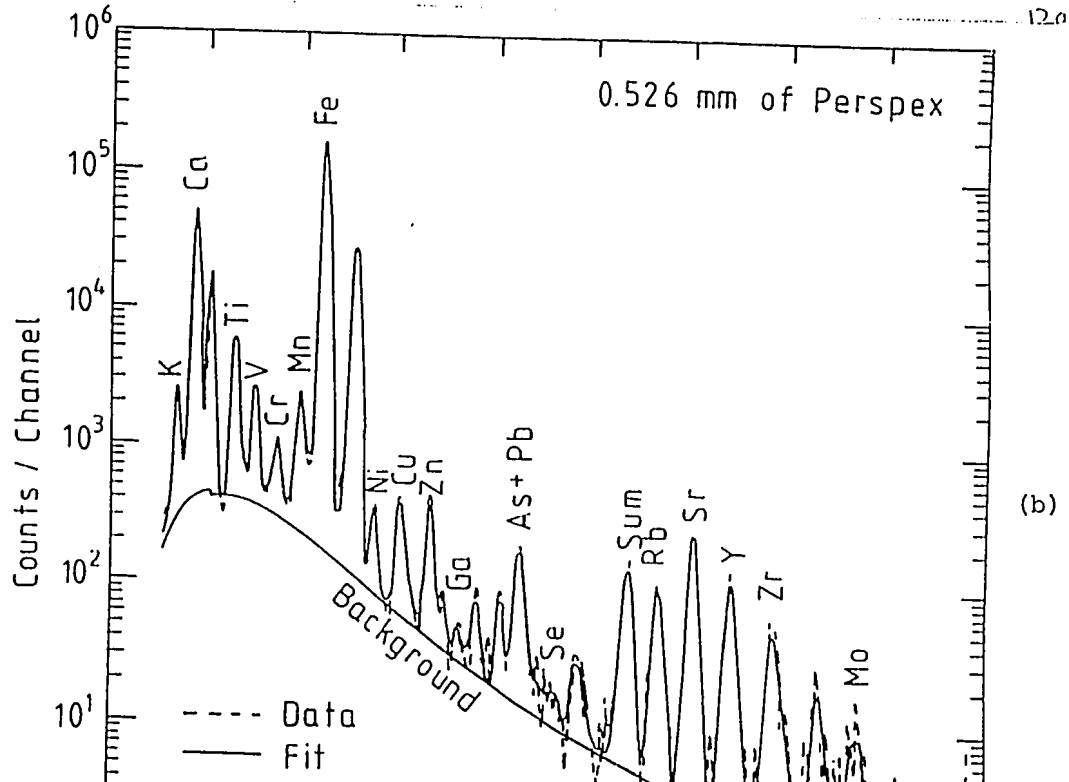
0.526 mm of Perspex
Counts / Channel
x-ray Energy (keV)
Background
Data
Fit
K
Ca
Ti
V
Cr
Mn
Fe
Ni
Cu
Zn
Ga
As+Pb
Se
Sum
Rb
Sr
Y
Zr
Mo
(b)

Fig. 26

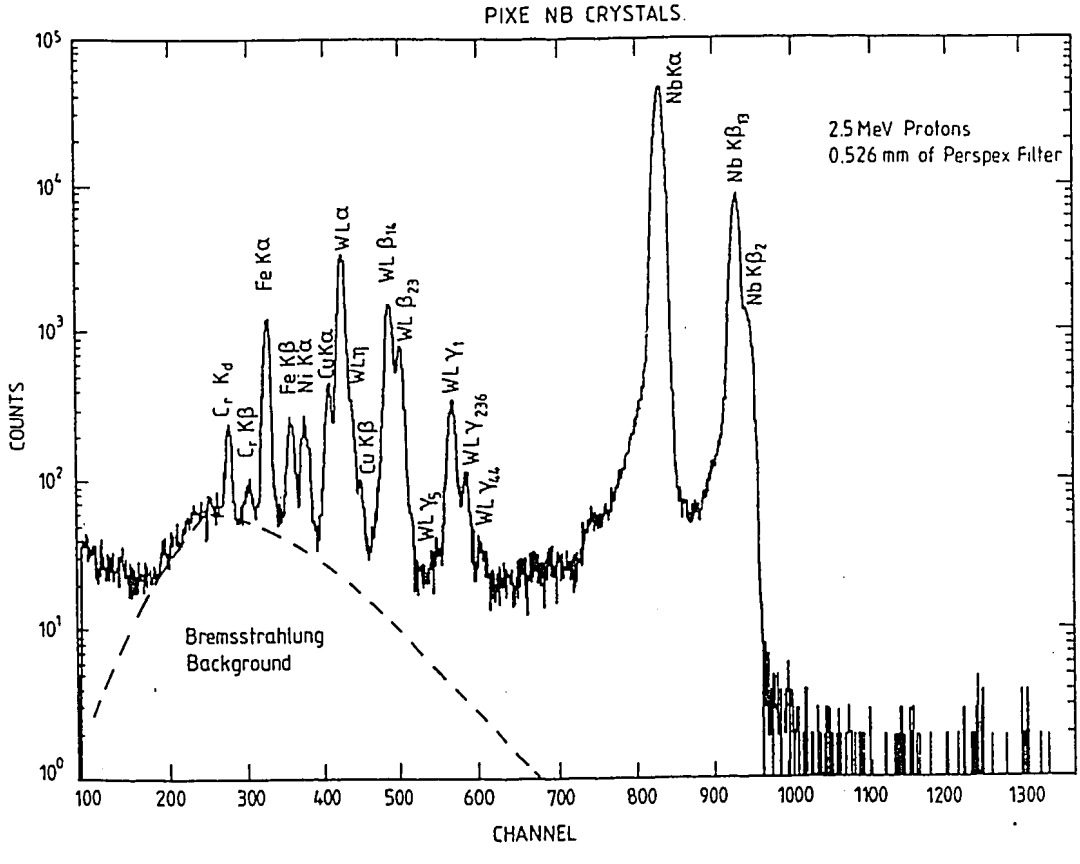
PIXE NB CRYSTALS.
2.5 MeV Protons
0.526 mm of Perspex Filter
COUNTS
CHANNEL
Cr Kα
Cr Kβ
Fe Kα
Fe Kβ
Ni Kα
Cu Kα
WLα
WLη
Cu Kβ
WL β14
WL β23
WL γ1
WL γ5
WL γ236
WL γ44
Nb Kα
Nb Kβ13
Nb Kβ2
Bremsstrahlung
Background

Fig. 27

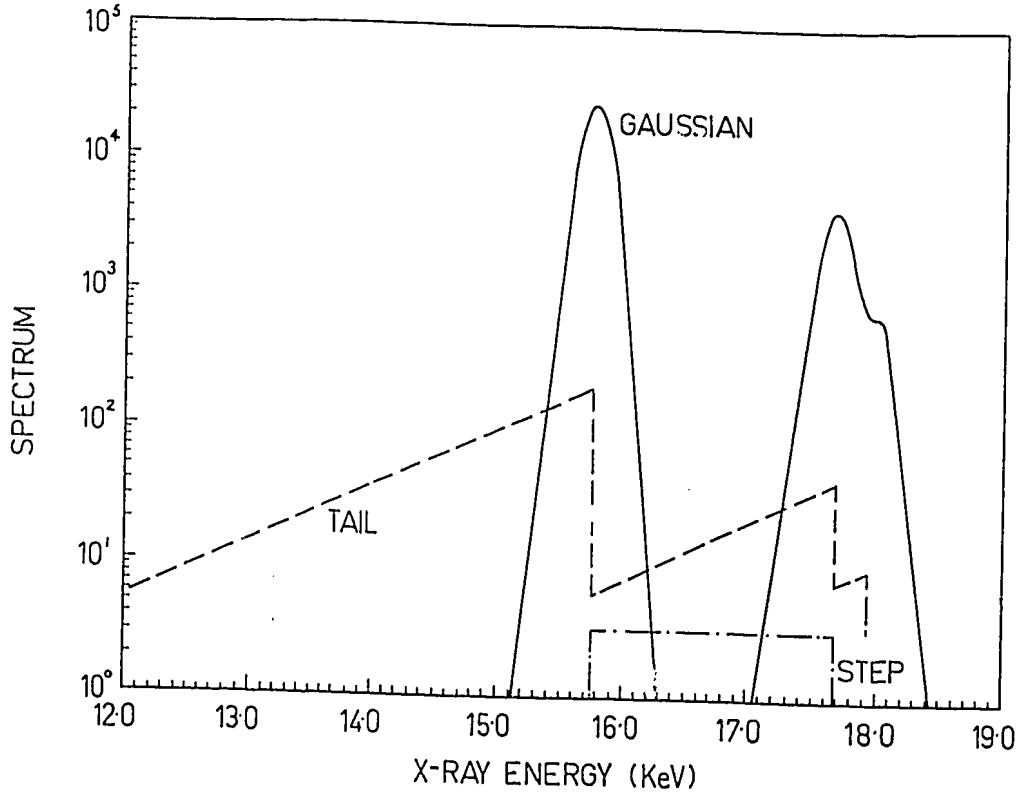
SPECTRUM
GAUSSIAN
TAIL
STEP
X-RAY ENERGY (KeV)

(a)

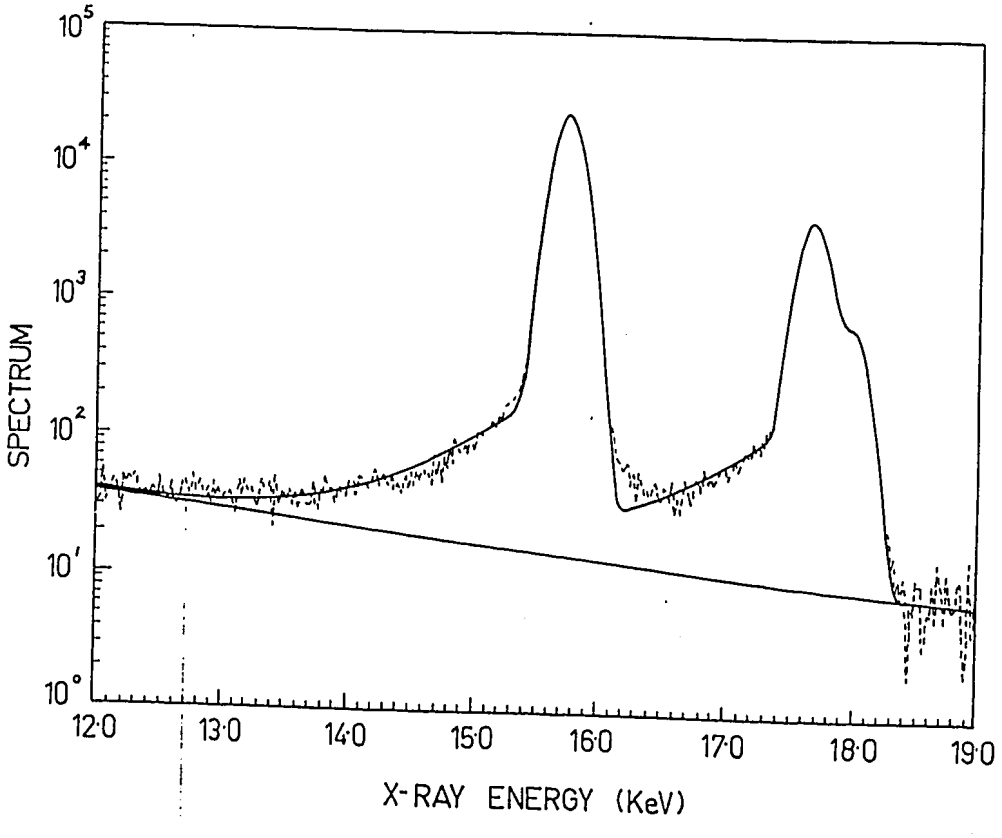
SPECTRUM
X-RAY ENERGY (KeV)

(b)

Fig. 28

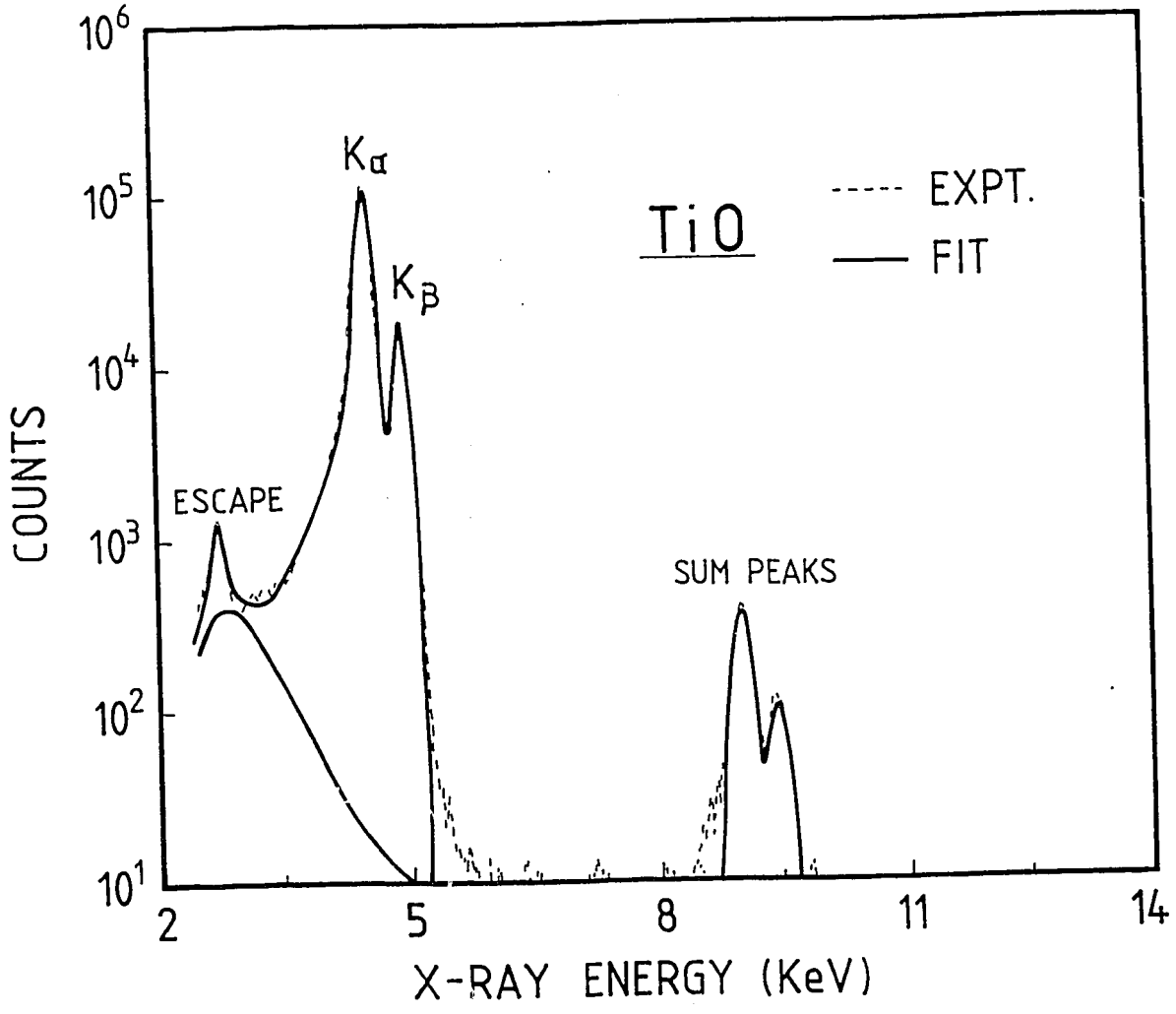
10^6
10^5
10^4
10^3
10^2
10^1
COUNTS
K_α
K_β
ESCAPE
SUM PEAKS
TiO
----- EXPT.
—— FIT
2
5
8
11
14
X-RAY ENERGY (KeV)

Fig. 29

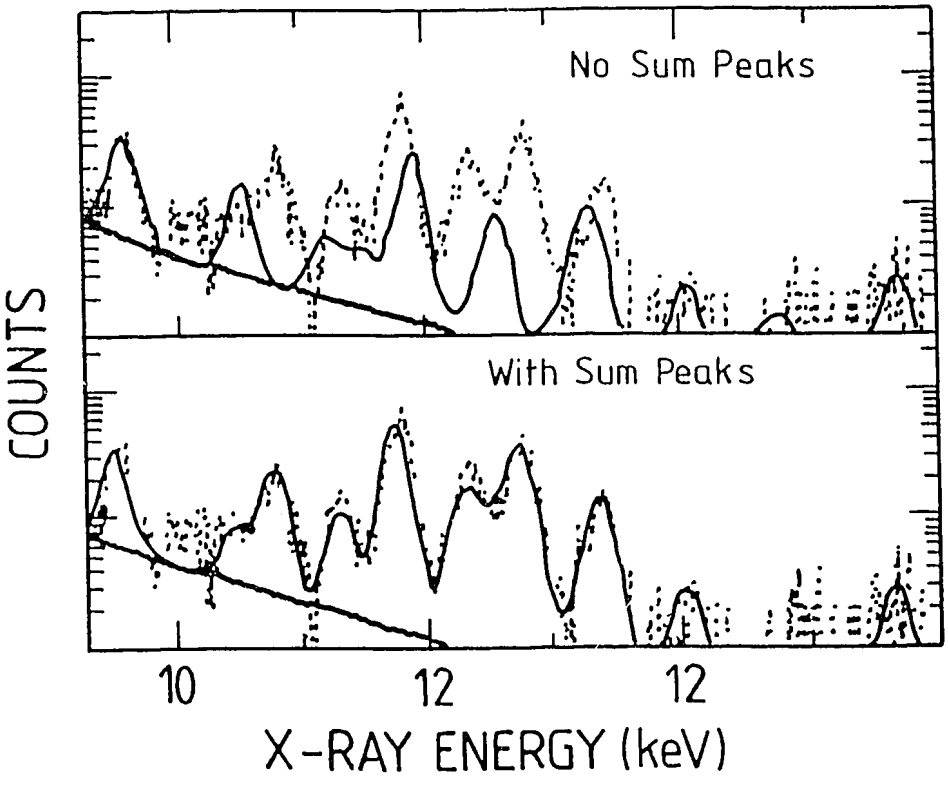

Fig. 30

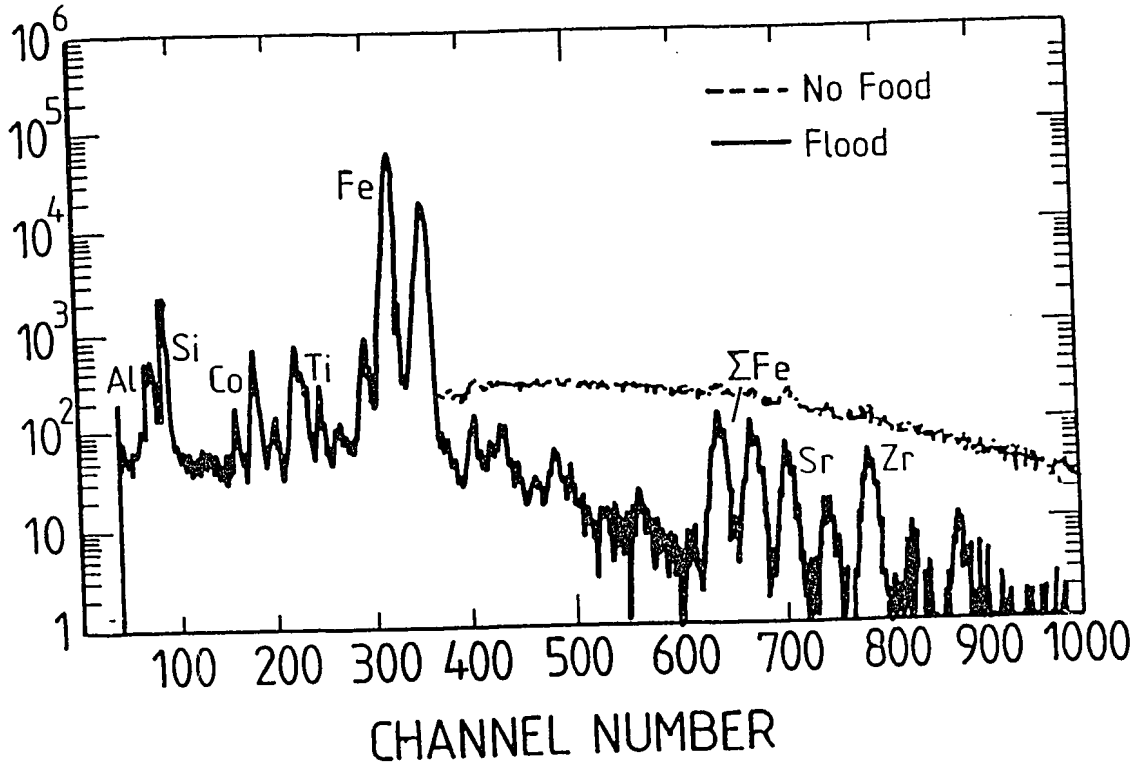
10^6
10^5
10^4
10^3
10^2
10
1
No Food
Flood
Fe
Al
Si
Co
Ti
ΣFe
Sr
Zr
100 200 300 400 500 600 700 800 900 1000
CHANNEL NUMBER

Fig. 31

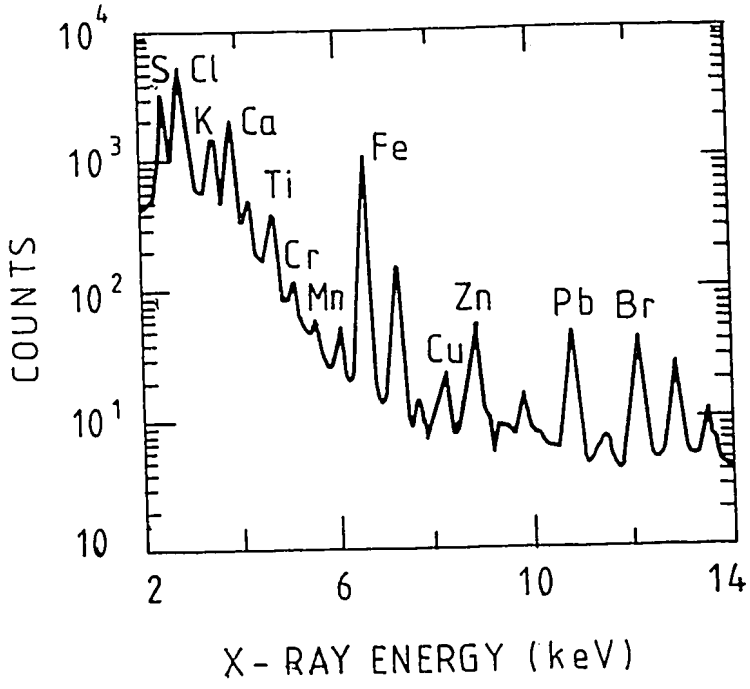
COUNTS
10^4
10^3
10^2
10^1
10
S
Cl
K
Ca
Ti
Cr
Mn
Fe
Cu
Zn
Pb
Br
2
6
10
14
X-RAY ENERGY (keV)

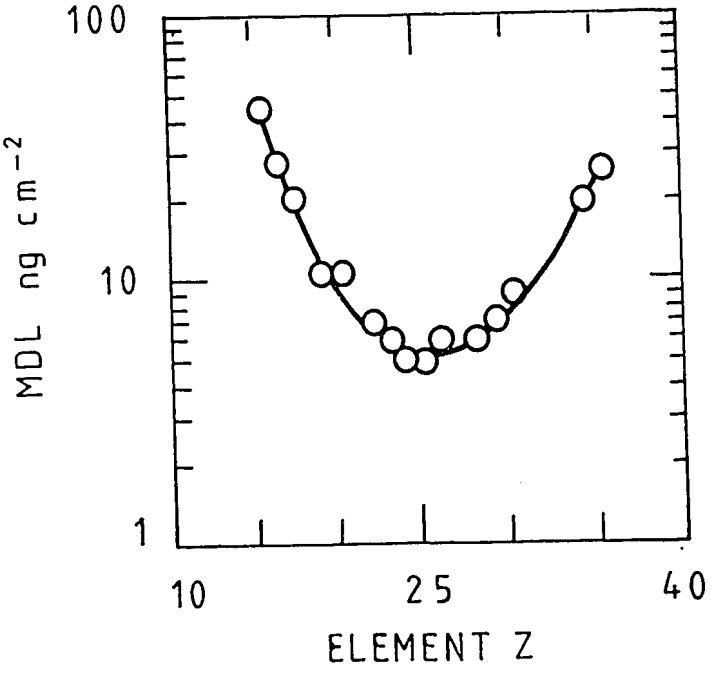
MDL ng cm^{-2}
100
10
1
10
25
40
ELEMENT Z

Fig. 32

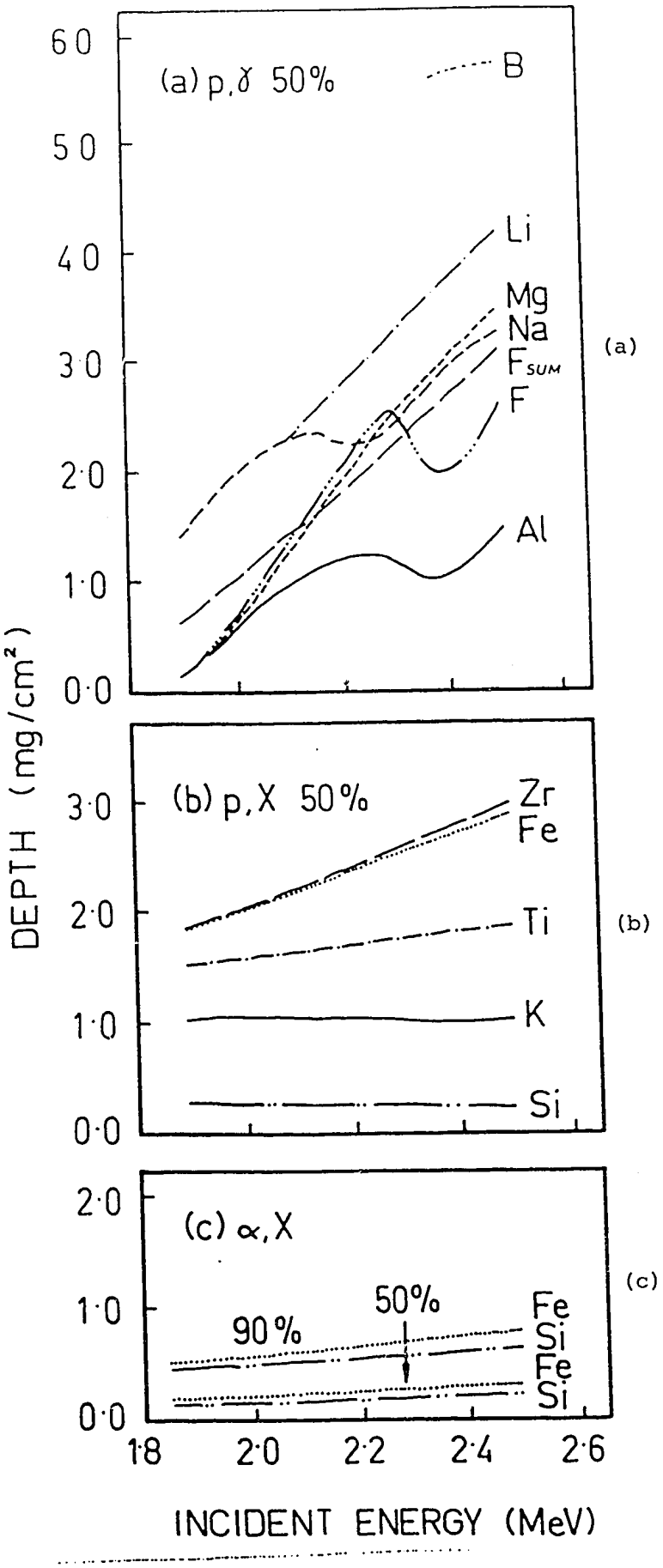
(a) p,γ 50%
B
Li
Mg
Na
F SUM
F
Al
(a)
(b) p,X 50%
Zr
Fe
Ti
K
Si
(b)
(c) α,X
50%
90%
Fe
Si
Fe
Si
(c)
DEPTH (mg/cm²)
INCIDENT ENERGY (MeV)
6·0
5·0
4·0
3·0
2·0
1·0
0·0
3·0
2·0
1·0
0·0
2·0
1·0
0·0
1·8
2·0
2·2
2·4
2·6

Fig. 33

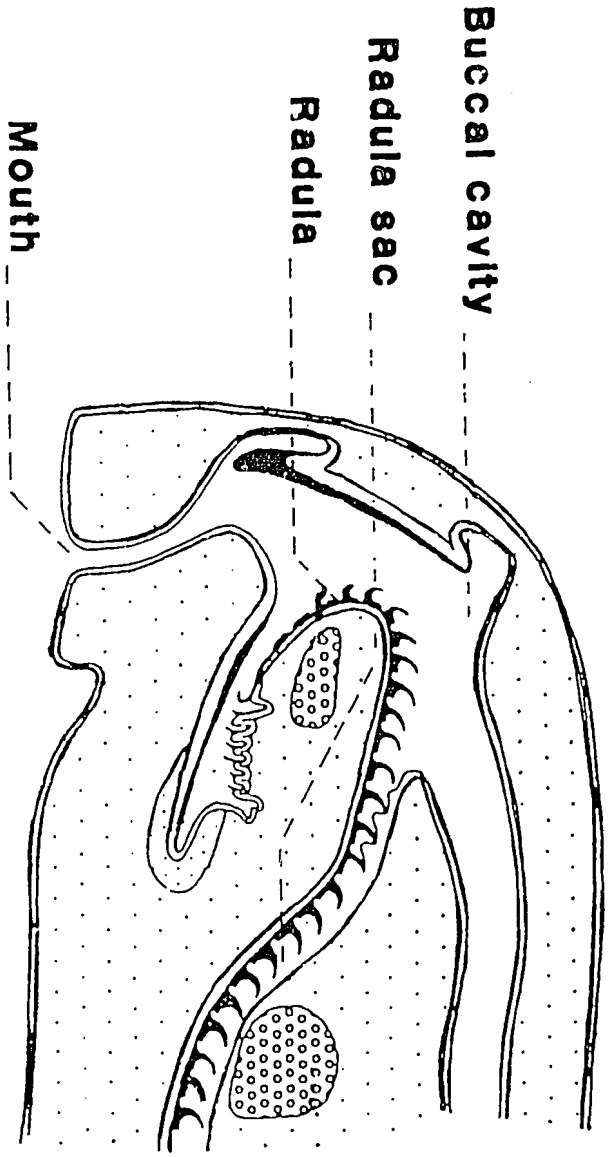

Fig. 34

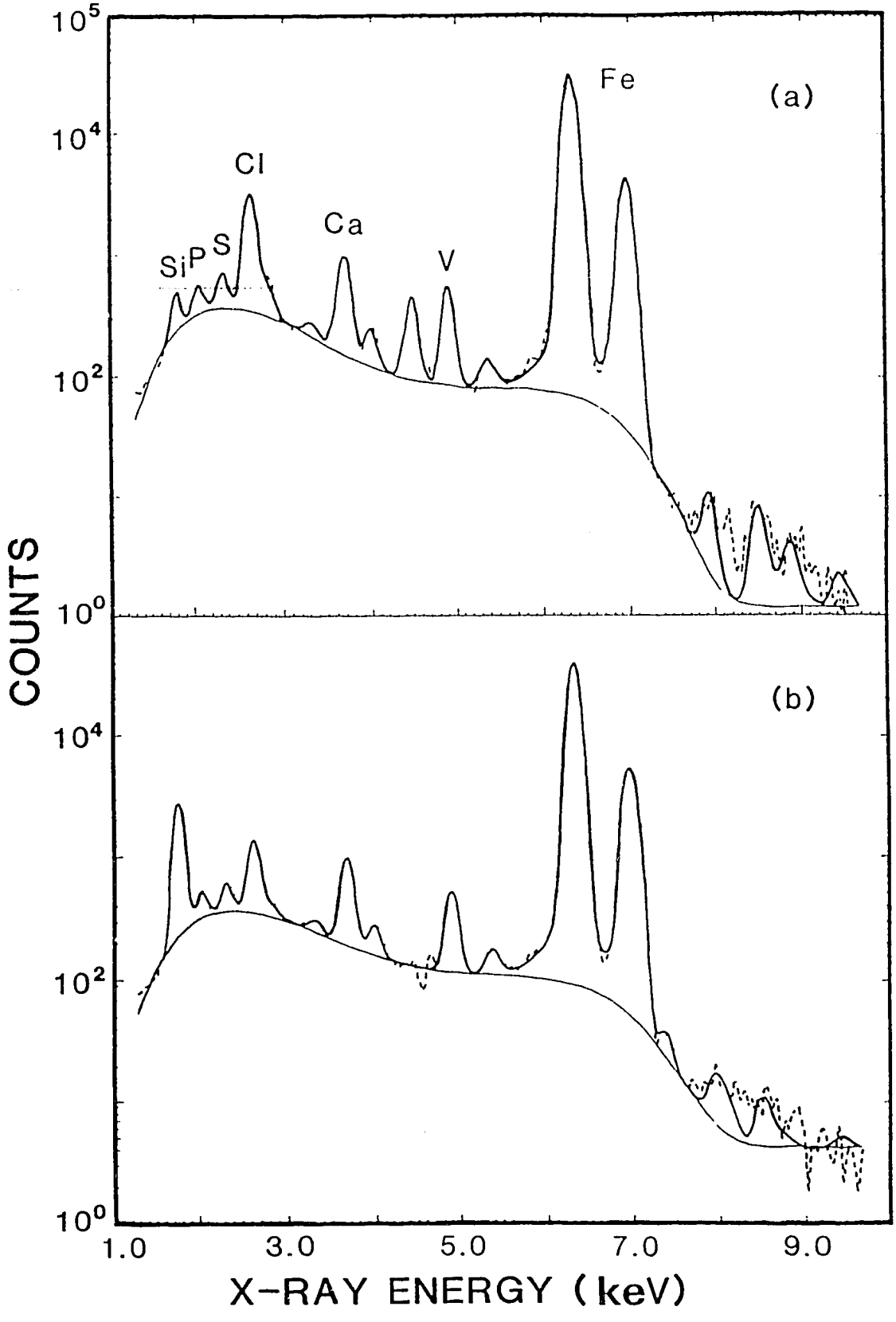
10^5
10^4
10^2
10^0
COUNTS
Si
P
S
Cl
Ca
V
Fe
(a)
(b)
1.0
3.0
5.0
7.0
9.0
X-RAY ENERGY (keV)

Fig. 35

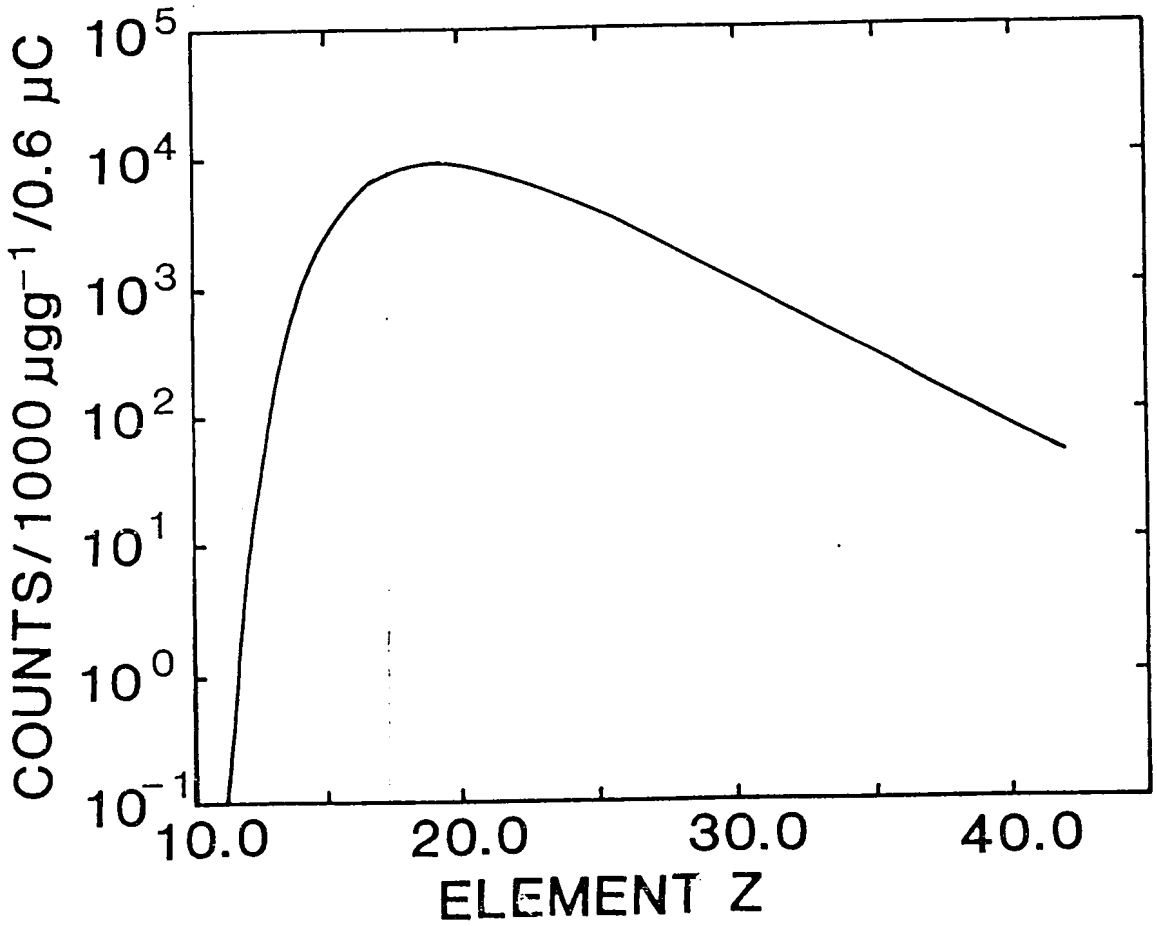

Na	0
Al	154
Si	1024
P	2450
S	5092
Cl	7286
K	9241
Ca	9018
V	5438
Fe	2951
Cu	1401
Zn	1089

Fig. 36

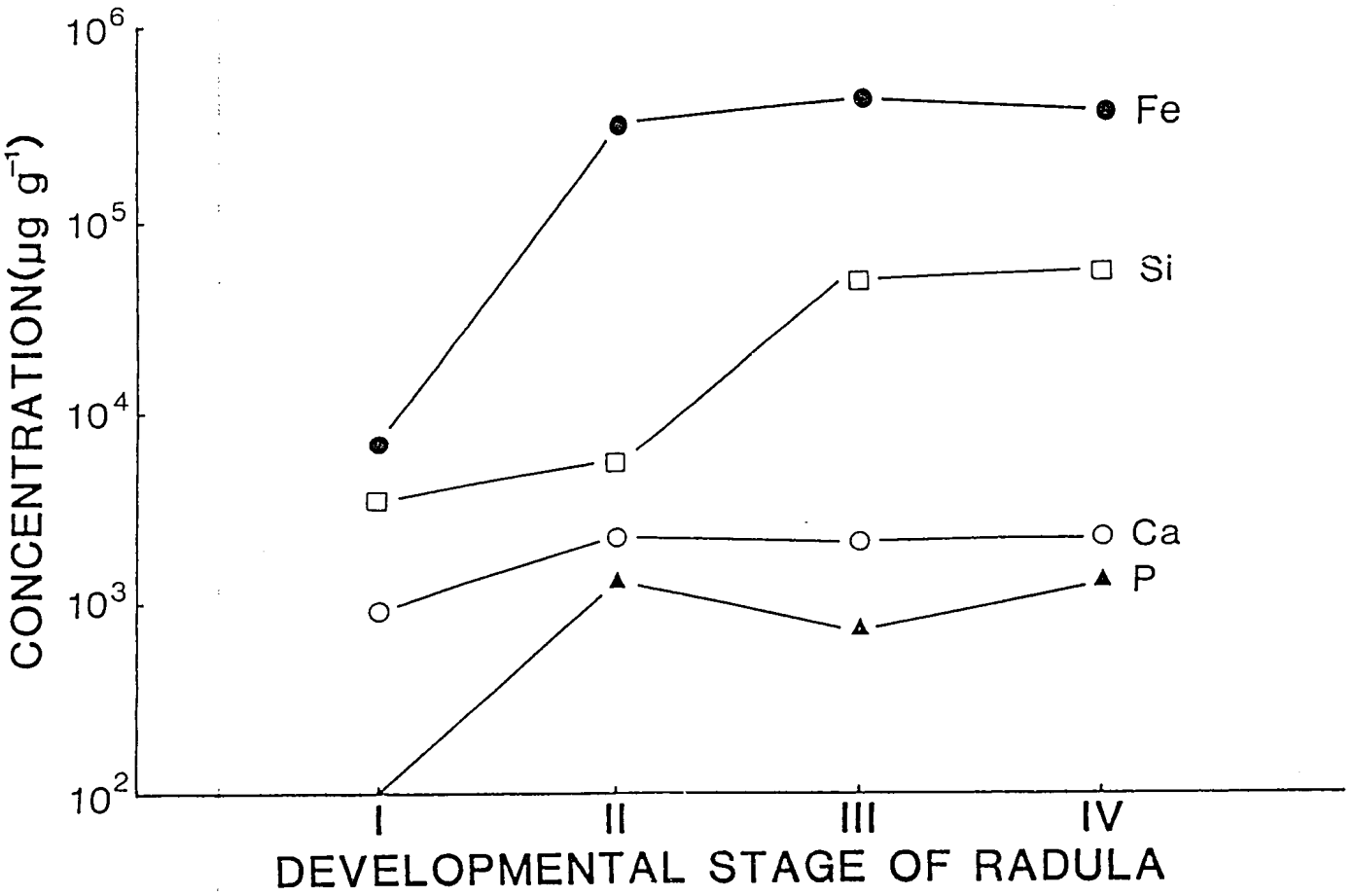
CONCENTRATION(μg g⁻¹)
10⁶
10⁵
10⁴
10³
10²
Fe
Si
Ca
P
I
II
III
IV
DEVELOPMENTAL STAGE OF RADULA

Fig. 37

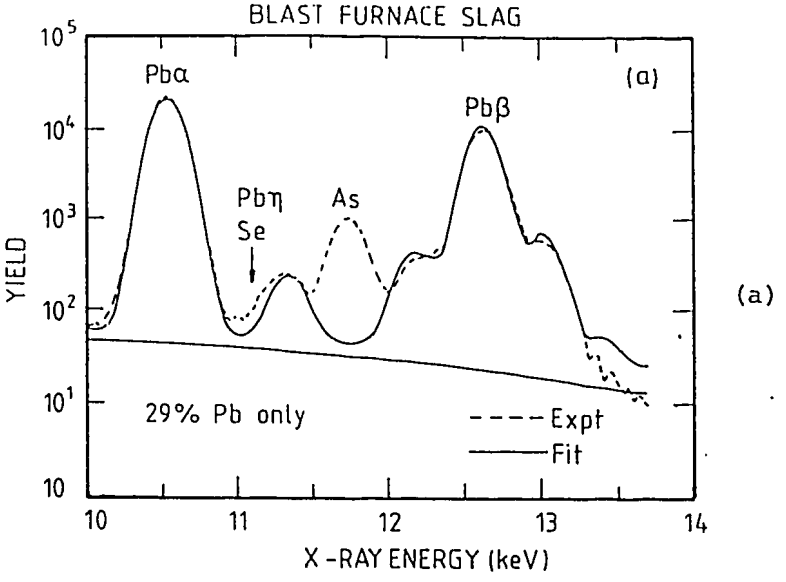
BLAST FURNACE SLAG
Pbα
(a)
Pbβ
Pbη
Se
As
YIELD
29% Pb only
Expt
Fit
X-RAY ENERGY (keV)

(a)

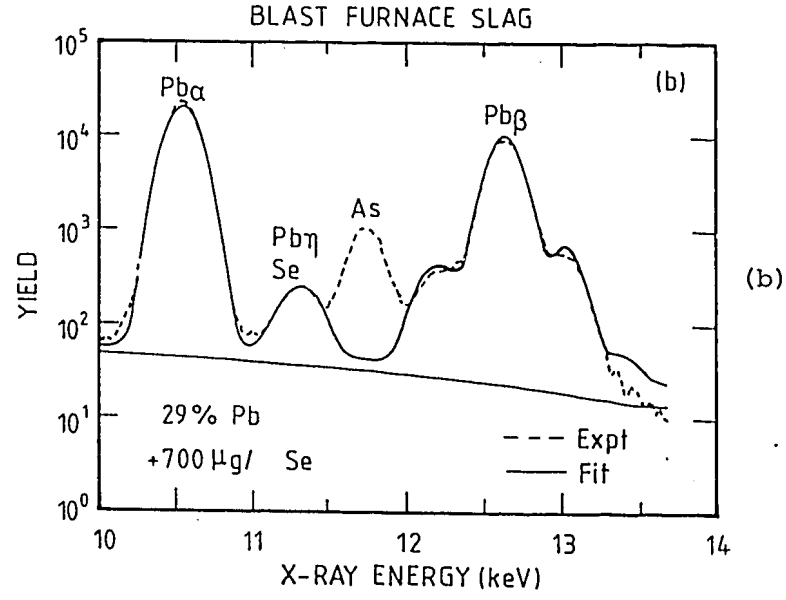
BLAST FURNACE SLAG
Pbα
(b)
Pbβ
As
Pbη
Se
YIELD
29% Pb
+700 µg/ Se
Expt
Fit
X-RAY ENERGY (keV)

(b)

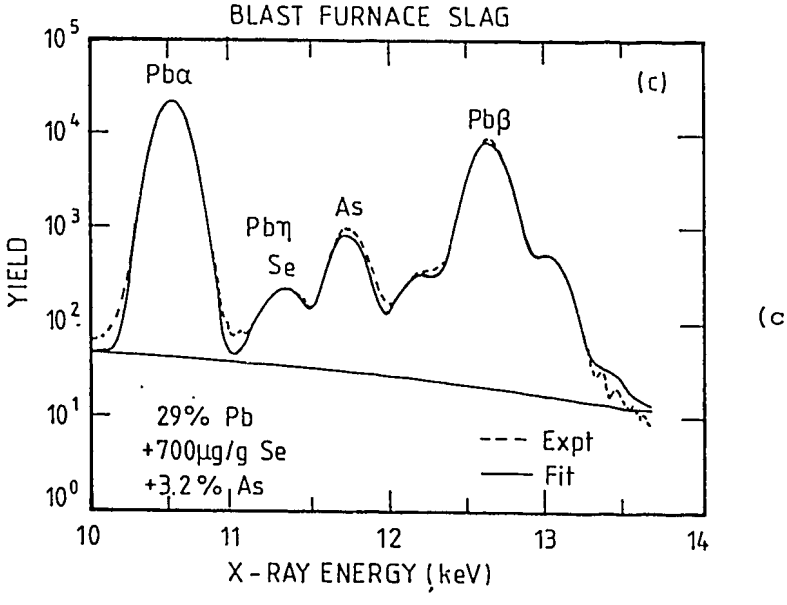
BLAST FURNACE SLAG
Pbα
(c)
Pbβ
As
Pbη
Se
YIELD
29% Pb
+700µg/g Se
+3.2% As
Expt
Fit
X-RAY ENERGY (keV)

(c)

Fig. 38

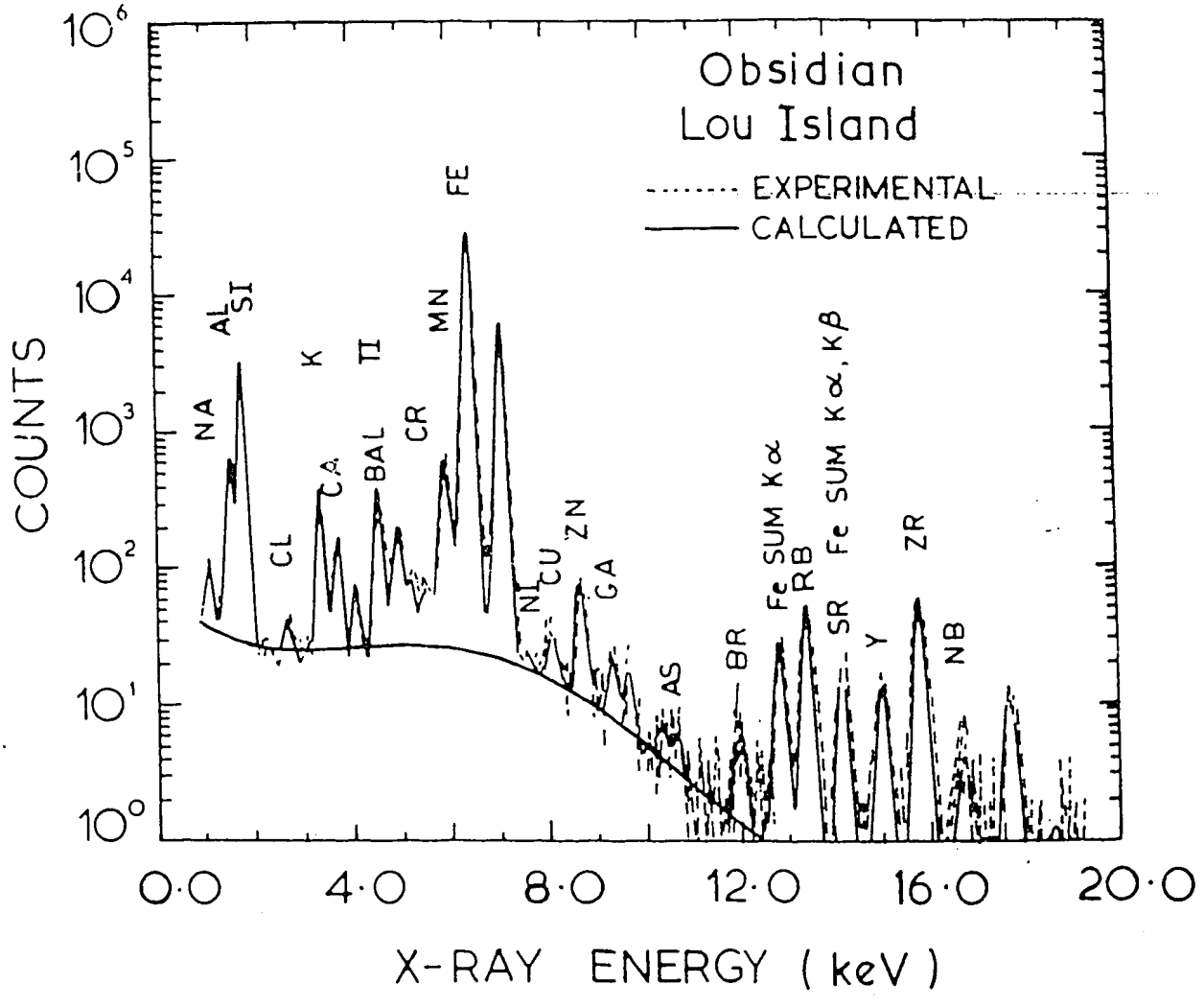

PIXIE Spectrum - Lou Island Obsidian

Fig. 39

Tracing trade patterns in prehistoric communities

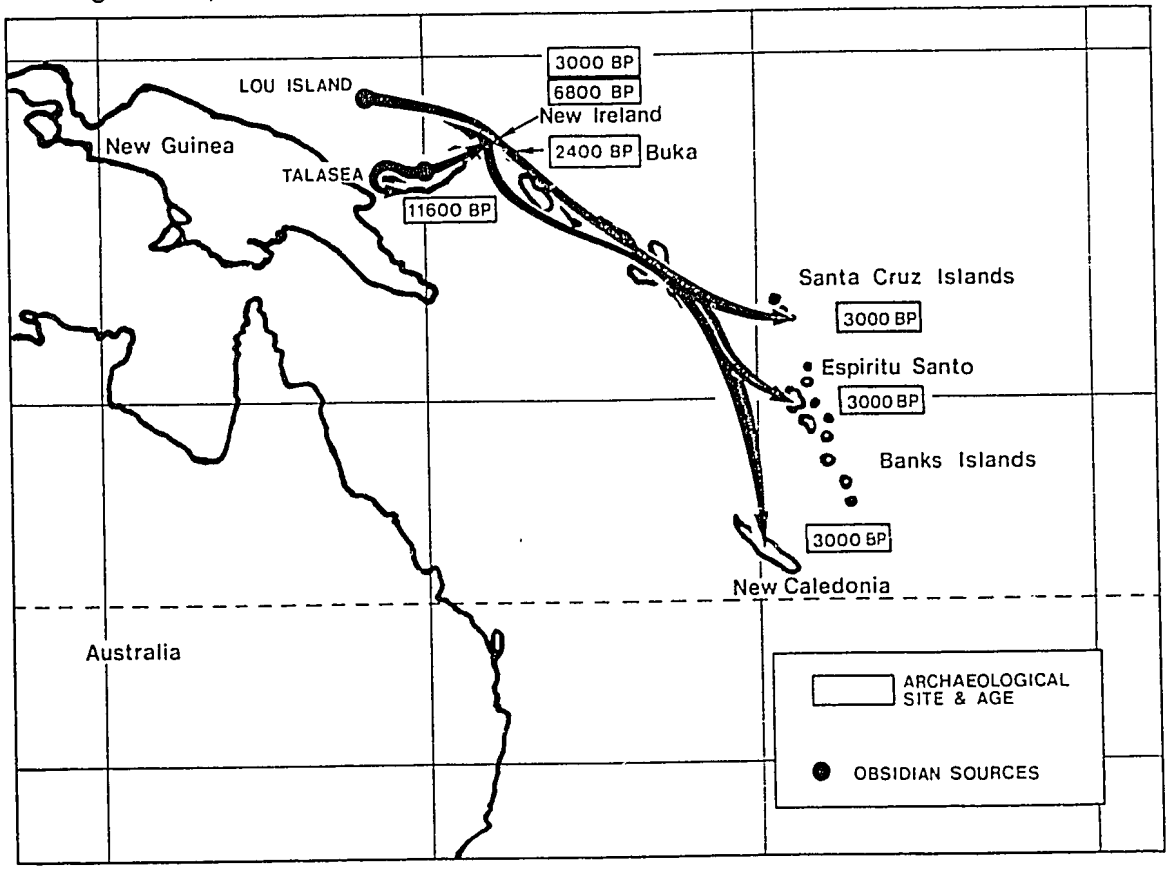

Fig. 40

APPENDIX A

USEFUL PIXE DATA

K Shell

Line Energies, Fluorescence yields and Emission Rates

		Energy (keV)					Relative Intensity Kα = 100	
Elt	Z	K_{abs}	$K\alpha_1$	$K\beta_1$	$K\beta_2$	ω_K	$K\beta_1$	$K\beta_2$
Na	11	1.072	1.041			0.023		
Mg	12	1.305	1.253			0.030		
Al	13	1.559	1.486			0.039		
Si	14	1.838	1.736	1.839		0.050	2.7	
P	15	2.142	2.013	2.139		0.063	4.3	
S	16	2.472	2.307	2.464		0.078	5.9	
Cl	17	2.822	2.621	2.816		0.097	8.2	
Ar	18	3.202	2.955	3.190		0.118	10.5	
K	19	3.607	3.312	3.589		0.140	11.7	
Ca	20	4.038	3.690	4.012		0.163	12.8	
Sc	21	4.496	4.088	4.460		0.188	13.1	
Ti	22	4.965	4.508	4.931		0.214	13.4	
V	23	5.465	4.949	5.426		0.243	13.5	
Cr	24	5.989	5.411	5.946		0.275	13.5	
Mn	25	6.540	5.894	6.489		0.308	13.5	
Fe	26	7.112	6.398	7.057		0.340	13.5	
Co	27	7.709	6.924	7.648		0.373	13.5	
Ni	28	8.333	7.471	8.263		0.406	13.5	
Cu	29	8.979	8.040	8.904		0.440	13.7	
Zn	30	9.659	8.630	9.570		0.474	13.8	
Ga	31	10.368	9.241	10.263		0.507	14.3	
Ge	32	11.104	9.874	10.980		0.535	14.7	
As	33	11.868	10.530	11.724		0.562	15.2	
Se	34	12.658	11.207	12.494		0.589	15.7	
Br	35	13.474	11.907	13.289	13.467	0.618	15.8	1.1
Rb	37	15.201	13.373	14.959	15.183	0.667	16.0	1.7
Sr	38	16.105	14.140	15.833	16.082	0.690	16.0	2.0
Y	39	17.037	14.931	16.735	17.013	0.710	16.3	2.2
Zr	40	17.998	15.744	17.665	17.967	0.730	16.6	2.4
Nb	41	18.986	16.581	18.619	18.949	0.747	16.8	2.6
Mo	42	20.002	17.441	19.610	19.962	0.765	17.0	2.7
Tc	43	21.054	18.325	20.615	21.002	0.780	17.3	2.8
Ru	44	22.118	19.233	21.653	22.070	0.794	17.5	2.9
Rh	45	23.224	20.165	22.720	23.169	0.808	17.7	3.0
Pd	46	24.350	21.121	23.815	24.295	0.820	17.9	3.1
Ag	47	25.514	22.101	24.938	25.452	0.831	17.9	3.3
Cd	48	26.711	23.106	26.091	26.639	0.843	17.8	3.5
In	49	27.940	24.136	27.271	27.856	0.853	18.1	3.6
Sn	50	29.200	25.191	28.481	29.104	0.862	18.5	3.7
Sb	51	30.491	26.271	29.721	30.388	0.870	18.5	3.7
I	53	33.169	28.607	32.289	33.036	0.884	18.9	4.0
Ba	56	37.441	32.062	36.372	37.251	0.902	19.2	4.5

L SHELL LINE ENERGIES (keV)

Elt	z	$L\alpha_1$	$L\ell$	$L\eta$	$L\beta_1$	$L\beta_2$	$L\beta_3$	$L\beta_4$	$L\beta_5$	$L\beta_6$	$L\gamma_1$	$L\gamma_2$	$L\gamma_3$	$L\gamma_4$	$L\gamma_5$	$L\gamma_6$
ZRL	40	2.040	1.792	1.876	2.124	2.219	2.201	2.187		2.171	2.302	2.502			2.255	
NBL	41	2.166	1.902	1.996	2.257	2.367	2.334	2.319		2.312	2.461	2.663			2.406	
MOL	42	2.293	2.015	2.120	2.394	2.518	2.473	2.455		2.455	2.623	2.830			2.563	
RUL	44	2.558	2.252	2.382	2.683	2.835	2.763	2.771		2.763	2.964	3.180			2.891	
RHL	45	2.696	2.376	2.519	2.834	3.001	2.915	2.890		2.922	3.143	3.363			3.064	
PDL	46	2.838	2.503	2.660	2.990	3.171	3.072	3.045		3.087	3.328	3.553			3.243	
AGL	47	2.984	2.633	2.806	3.150	3.347	3.234	3.203		3.255	3.519	3.743			3.428	
CDL	48	3.133	2.767	2.956	3.316	3.528	3.401	3.367		3.429	3.716	3.951			3.619	
INL	49	3.286	2.904	3.112	3.487	3.713	3.572	3.535		3.608	3.920	4.160		4.236	3.815	
SNL	50	3.443	3.044	3.272	3.662	3.904	3.750	3.708		3.792	4.130	4.376		4.463	4.018	
SBL	51	3.604	3.188	3.436	3.843	4.100	3.932	3.886		3.979	4.347	4.599		4.696	4.228	
TEL	52	3.796	3.335	3.605	4.029	4.301	4.120	4.069		4.173	4.570	4.828		4.936	4.443	
IL	53	3.937	3.484	3.780	4.221	4.507	4.313	4.257		4.370	4.800	5.065		5.184	4.665	
CSL	55	4.286	3.794	4.141	4.619	4.935	4.716	4.649		4.780	5.279	5.541	5.552	5.702	5.128	
BAL	56	4.465	3.953	4.330	4.827	5.156	4.926	4.851		4.993	5.530	5.796	5.808	5.972	5.370	
LAL	57	4.650	4.124	4.524	5.041	5.383	5.143	5.061		5.211	5.788	6.059	6.073	6.251	5.620	
CEL	58	4.839	4.287	4.731	5.261	5.612	5.364	5.276		5.433	6.051	6.324	6.340	6.527	5.874	
PRL	59	5.033	4.452	4.935	5.488	5.849	5.591	5.497		5.659	6.321	6.597	6.615	6.814	6.135	
NDL	60	5.229	4.632	5.145	5.721	6.088	5.828	5.721		5.892	6.601	6.882	6.900	7.106	6.405	
SML	62	5.635	4.994	5.588	6.204	6.586	6.317	6.195	6.711	6.369	7.177	7.465	7.485	7.712	6.967	7.306
EUL	63	5.845	5.176	5.816	6.455	6.842	6.570	6.438	6.975	6.616	7.479	7.766	7.795	8.029	7.255	7.613
GDL	64	6.056	5.361	6.049	6.712	7.102	6.830	6.686	7.236	6.866	7.784	8.086	8.104	8.354	7.553	7.924
TBL	65	6.272	5.546	6.283	6.977	7.365	7.095	6.939	7.508	7.115	8.100	8.396	8.422	8.683	7.852	8.245
DYL	66	6.494	5.742	6.533	7.246	7.634	7.369	7.203	7.804	7.369	8.417	8.713	8.752	9.018	8.165	8.574
HOL	67	6.719	5.942	6.787	7.524	7.910	7.650	7.470	8.061	7.634	8.746	9.049	9.086	9.373	8.480	8.903
ERL	68	6.947	6.152	7.057	7.809	8.188	7.938	7.744	8.349	7.908	9.087	9.384	9.429	9.721	8.812	9.253
TML	69	7.179	6.341	7.308	8.100	8.467	8.229	8.024	8.639	8.176	9.424	9.728	9.778	10.083	9.143	9.606
YBL	70	7.414	6.544	7.579	8.400	8.757	8.535	8.312	8.938	8.455	9.788	10.088	10.141	10.458	9.484	9.975
LUL	71	7.654	6.752	7.856	8.708	9.047	8.845	8.605	9.239	8.736	10.142	10.458	10.509	10.840	9.841	10.341
HFL	72	7.898	6.958	8.138	9.021	9.346	9.162	8.904	9.553	9.021	10.514	10.832	10.889	11.238	10.199	10.731
TAL	73	8.145	7.172	8.427	9.342	9.650	9.486	9.211	9.873	9.314	10.893	11.215	11.276	11.643	10.569	11.129
WL	74	8.396	7.386	8.723	9.671	9.960	9.817	9.524	10.199	9.610	11.284	11.606	11.672	12.061	10.947	11.537
REL	75	8.651	7.602	9.026	10.008	10.274	10.158	9.845	10.530	9.909	11.683	12.008	12.080	12.490	11.332	11.954
OSL	76	8.910	7.821	9.335	10.354	10.597	10.509	10.174	10.869	10.215	12.093	12.420	12.498	12.921	11.728	12.383
IRL	77	9.174	8.040	9.649	10.706	10.919	10.866	10.509	11.209	10.523	12.510	12.840	12.922	13.366	12.132	12.818
PTL	78	9.441	8.267	9.973	11.069	11.249	11.233	10.852	11.559	10.840	12.940	13.268	13.359	13.826	12.550	13.269
AUL	79	9.712	8.493	10.307	11.440	11.583	11.608	11.203	11.914	11.158	13.379	13.707	13.807	14.297	12.972	13.728
HGL	80	9.987	8.720	10.649	11.821	11.922	11.993	11.561	12.275	11.480	13.828	14.160	14.262	14.776	13.408	14.196
TLL	81	10.267	8.952	10.992	12.211	12.270	12.388	11.929	12.641	11.810	14.289	14.623	14.734	15.269	13.850	14.684
PBL	82	10.554	9.183	11.347	12.612	12.621	12.791	13.013	12.304	12.141	13.370	14.762	15.200	15.765	14.305	15.176
BIL	83	10.837	9.419	11.710	13.021	12.978	13.208	12.689	13.393	12.479	15.245	15.580	15.708	16.292	14.771	15.683
RAL	88	12.338	10.620	13.661	15.233	14.839	15.442	14.745	15.375	14.234	17.845	18.176	18.354	19.081	17.271	18.411
THL	90	12.967	11.117	14.507	16.199	15.621	16.423	15.640	16.211	14.973	18.979	19.302	19.503	20.289	18.361	19.596
PAL	91	13.288	11.364	14.944	16.699	16.022	16.927	16.101	16.634	15.343	19.565	19.869	20.094	20.879	18.925	20.212
UL	92	13.612	11.616	15.397	17.217	16.425	17.452	16.573	17.067	15.723	20.164	20.481	20.709	21.559	19.504	20.839

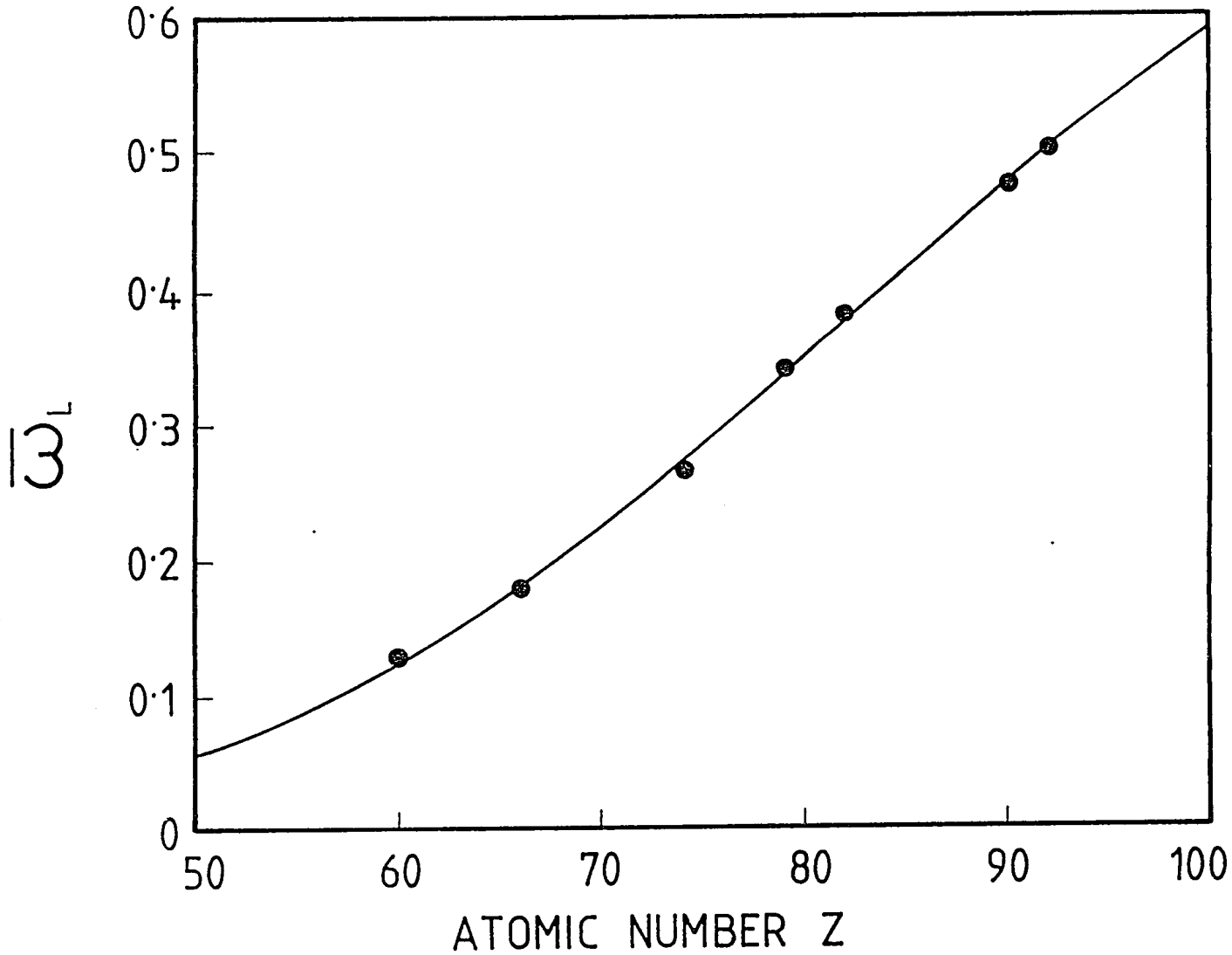
0·6
0·5
0·4
0·3
0·2
0·1
0
$\bar{\omega}_L$
50
60
70
80
90
100
ATOMIC NUMBER Z

L Subshell

Fluorescence Yields and Coster-Kronig Transitions Rates

Z	ω_1	ω_2	ω_3	$f_{1\,2}$	$f_{1\,3}$	$f_{2\,3}$	$f'_{1\,3}$	ν_1	ν_2	ν_3
28	0.0014	0.0086	0.0093	0.300	0.55	0.028		0.0092	0.0089	0.0093
30	0.0018	0.011	0.012	0.290	0.54	0.026		0.0116	0.0113	0.012
32	0.0024	0.013	0.015	0.280	0.53	0.050		0.0142	0.0138	0.015
34	0.0032	0.016	0.018	0.280	0.52	0.076		0.0174	0.0174	0.018
36	0.0041	0.020	0.022	0.270	0.52	0.100		0.0215	0.0222	0.022
38	0.0051	0.024	0.026	0.270	0.52	0.117		0.0259	0.0270	0.026
40	0.0068	0.028	0.031	0.260	0.52	0.132	0.0001	0.0313	0.0321	0.031
42	0.010	0.034	0.037	0.100	0.61	0.141	0.0001	0.0365	0.0392	0.037
44	0.012	0.040	0.043	0.100	0.61	0.148	0.0001	0.0429	0.0464	0.043
46	0.014	0.047	0.049	0.100	0.60	0.151	0.0001	0.0488	0.0544	0.049
48	0.018	0.056	0.056	0.100	0.59	0.155	0.0001	0.0575	0.0647	0.056
50	0.037	0.065	0.064	0.170	0.27	0.157	0.0003	0.0671	0.0750	0.064
52	0.041	0.074	0.074	0.180	0.28	0.155	0.0003	0.0771	0.0855	0.074
54	0.046	0.083	0.085	0.190	0.28	0.154	0.0004	0.0881	0.0961	0.085
56	0.052	0.096	0.097	0.190	0.28	0.153	0.0005	0.1003	0.1108	0.097
58	0.058	0.110	0.111	0.190	0.29	0.153	0.0006	0.1144	0.1270	0.111
60	0.064	0.124	0.125	0.190	0.30	0.152	0.0007	0.1288	0.1430	0.125
62	0.071	0.140	0.139	0.190	0.30	0.150	0.0008	0.1434	0.1609	0.139
64	0.079	0.158	0.155	0.190	0.30	0.147	0.0010	0.1600	0.1808	0.155
66	0.089	0.178	0.174	0.190	0.30	0.143	0.0012	0.1800	0.2029	0.174
68	0.100	0.200	0.192	0.190	0.30	0.140	0.0014	0.2010	0.2269	0.192
70	0.112	0.222	0.210	0.190	0.29	0.138	0.0018	0.2210	0.2510	0.210
72	0.128	0.246	0.231	0.180	0.28	0.135	0.0023	0.2431	0.2772	0.231
74	0.147	0.270	0.255	0.170	0.28	0.133	0.0028	0.2708	0.3039	0.255
76	0.130	0.295	0.281	0.160	0.39	0.128	0.0029	0.2934	0.3310	0.281
78	0.114	0.321	0.306	0.140	0.50	0.124	0.0028	0.3181	0.3589	0.306
80	0.107	0.347	0.333	0.130	0.56	0.120	0.0030	0.3448	0.3870	0.333
82	0.112	0.373	0.360	0.120	0.58	0.116	0.0035	0.3718	0.4148	0.360
84	0.122	0.401	0.386	0.110	0.58	0.111	0.0042	0.3963	0.4438	0.386
86	0.134	0.429	0.411	0.100	0.58	0.110	0.0052	0.4219	0.4742	0.411
88	0.146	0.456	0.437	0.090	0.58	0.108	0.0064	0.4475	0.5032	0.437
90	0.161	0.479	0.463	0.090	0.57	0.108	0.0078	0.4761	0.5290	0.463
92	0.176	0.467	0.489	0.080	0.57	0.167	0.0097	0.5034	0.5487	0.489
94	0.205	0.464	0.514	0.050	0.56	0.198	0.0130	0.5278	0.5658	0.514
96	0.228	0.479	0.539	0.040	0.55	0.200	0.0160	0.5565	0.5868	0.539

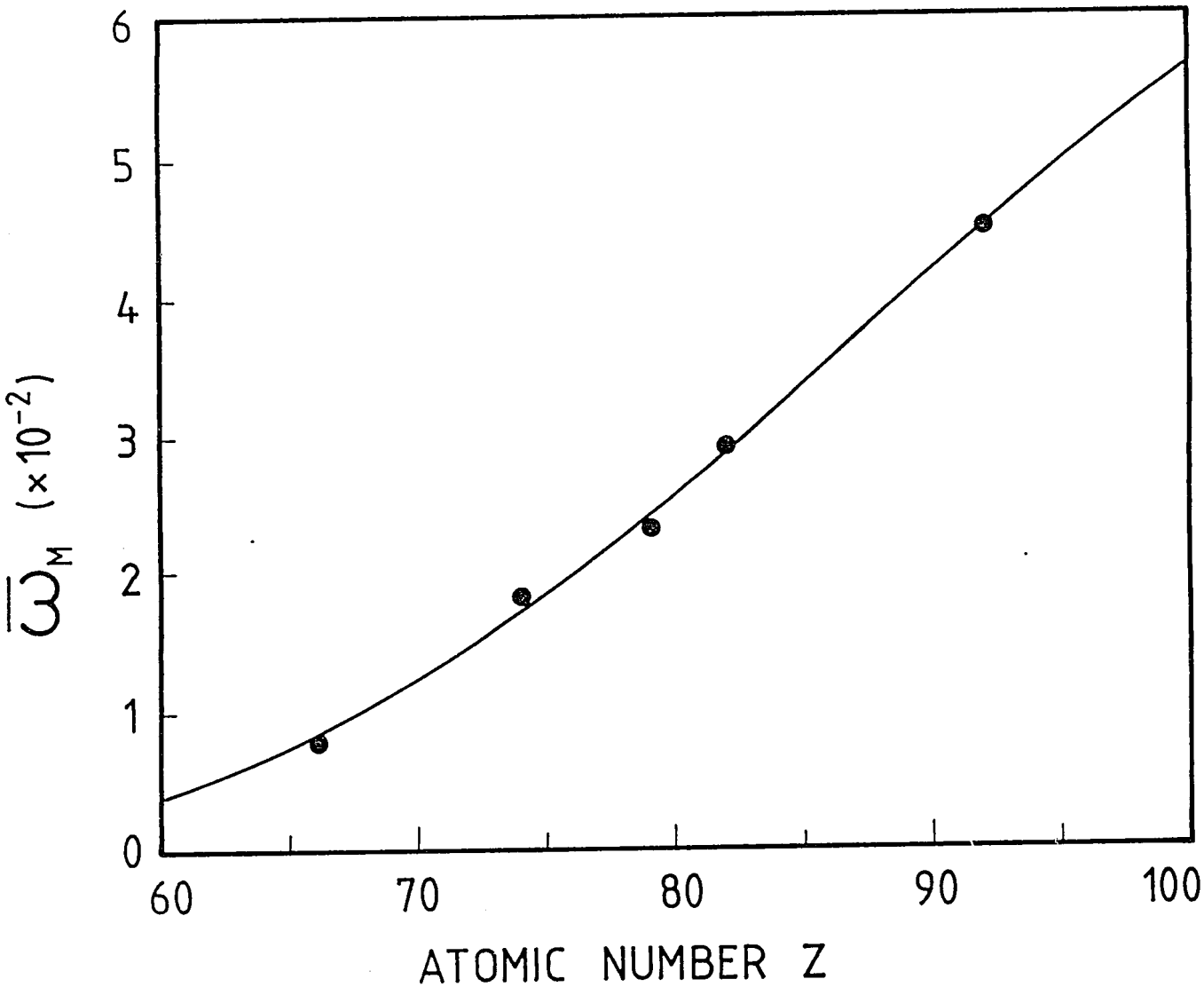
6
5
4
3
2
1
0
$\overline{\omega}_M$ ($\times 10^{-2}$)
60
70
80
90
100
ATOMIC NUMBER Z

POLYNOMIAL COEFFICIENTS FOR K, L AND M FLUORESCENCE YIELDS

	+2% Z_2 Range	a_0	a_1	a_2	a_3
ω_K	15-100	8.51051 (-2)	2.63414 (-2)	1.63531 (-4)	-1.85999 (-6)
ω_{L_1}	-	-	-	-	-
ω_{L_2} (low)	26-50	-2.10360 (-1)	3.00290 (-2)	-5.59134 (-4)	4.96758 (-6)
ω_{L_2} (high)	42-90	1.70027 (-1)	2.98746 (-3)	8.70636 (-5)	-2.19916 (-7)
ω_{L_3} (low)	26-50	-2.15069 (-1)	3.86054 (-2)	-4.51841 (-4)	3.40731 (-6)
ω_{L_3} (high)	40-100	2.72447 (-1)	-9.47505 (-4)	1.37650 (-4)	-4.64780 (-7)
$\bar{\omega}_L$	60-92	2.98616 (-2)	6.18664 (-3)	8.09073 (-5)	-3.63728 (-7)
ν_{L_1} (low)	24-50	-3.60403 (-1)	4.08005 (-2)	-7.94763 (-4)	6.60345 (-6)
ν_{L_1} (high)	48-94	-6.14390 (-1)	-1.67030 (-2)	3.75467 (-4)	-1.61631 (-6)
ν_{L_2} (low)	27-47	3.52923 (-1)	-1.79312 (-2)	7.70240 (-4)	-6.85678 (-6)
ν_{L_2} (high)	45-110	5.67613 (-1)	-1.56443 (-2)	3.78921 (-4)	-1.65536 (-6)
$\bar{\omega}_M$	60-100	-3.25820 (-1)	9.10791 (-3)	3.80983 (-5)	-4.62897 (-7)

POLYNOMIAL COEFFICIENTS FOR PROTON BOMBARDMENT

	Fitted Range	a_0	a_1	a_2	a_3	a_4	a_5
K (ECPSSR)	10-58	1.099955 (1)	6.078148 (-1)	-4.564251 (-1)	3.312473 (-2)	1.373860 (-2)	1.481521 (-3)
L (ECPSSR)	50-93	1.236572 (1)	5.423245 (-1)	-5.570508 (-1)	-5.193862 (-2)	-7.355058 (-4)	1.612867 (-3)
M (PWBA)	66-92	6.317504 (0)	5.905036 (-1)	-4.082184 (-1)	1.783166 (-2)	4.868465 (-2)	4.958070 (-3)
M (CPWBA)	66-92	6.301553 (0)	6.173717 (-1)	-4.354831 (-1)	9.984461 (-3)	6.224392 (-2)	1.773666 (-2)

Table 8
Reference ionization cross sections for protons, in b, compared to analytical fits due to other authors. Errors are given below the values.

Target	Energy (MeV)	σ_{ref}	Johansson [1]	Lopes [32]	Khan [33]	Rosato [34]
Al	0.5	6050	6247		4849	
		600	60			
	1	17400	17800		13900	
		1700	180			
	2	29300	30000		21400	
		2900	300			
	5	30600	28000			
		3100	1400			
	10	22500	20900			
		2300	1040			
Cu	0.2	0.0332			0.023	
		0.0017				
	0.5	1.623	1.74		1.21	
		0.032	0.09			
	1	15.90	15.88	16.1	14.5	
		0.32	0.16			
	2	96.0	89.7	98.3	93.8	96.5
		1.9	0.9			0.8
	5	462.4	450		434	
		9.2	5			
	10	844	847		836	
		17	8			
Ag	0.5	3.77×10^{-3}	1.63×10^{-3}		4.96×10^{-3}	
		0.30	0.08			
	1	0.0829	0.055	0.077	0.087	
		0.0066	0.003			
	2	0.907	0.69	0.84	0.906	
		0.073	0.01			
	5	9.55	8.34		9.85	
		0.76	0.08			
	10	35.0	33.1		36.7	
		2.8	0.3			
Au	2	4.09×10^{-3}	0.62×10^{-3}			
		0.41	0.03			
	5	0.0860	0.0315			
		0.0086	0.0015			
	10	0.474	0.264			
		0.047	0.003			

Mass Attenuation Coefficients (μ/ρ cm^2 g^{-1})
E in keV

		$E > E_K$	$E_K > E > E_{L\,1}$	$E_{L\,2} > E > E_{L\,3}$	$E_{L\,3} > E > E_M$
$3 \leq Z \leq 10$	a b c %	8.41 2.92 3.07 2			
$11 \leq Z \leq 18$	a b c %	15.50 2.79 2.73 2	0.528 2.74 3.03 4		
$19 \leq Z \leq 36$	a b c %	25.26 2.66 2.47 2	0.859 2.70 2.90 1		$1.27.10^{-2}$ 2.44 3.47 3
$37 \leq Z \leq 54$	a b c %		0.992 2.70 2.88 1	0.588 2.62 2.82 6	
$55 \leq Z \leq 71$	a b c %		1.11 2.70 2.83 1		$8.55.10^{-2}$ 2.50 2.98 3
$72 \leq Z \leq 86$	a b c %		$5.58.10^{-2}$ 2.50 3.38 4		$5.76.10^{-2}$ 2.55 3.09 1
$87 \leq Z \leq 94$	a b c %				$4.32.10^{-4}$ 2.63 4.26 3

$$(\mu/\rho) = a\ E^{-b}\ Z^{c}$$

% is the three standard deviation percentage error on the fit

Operating Characteristic	WDS	EDS
Geometrical collection efficiency	Variable<0.2%	<2%
Overall quantum efficiency	Variable<30%	100% for2-16keV
	Detects Z ≥4	Detects Z ≥11
Resolution	Crystal dependent	Energy dependent
	5eV	140eV at 5.9keV
Count rate (maximum)	50kHz	5kHz
Minimum useful probe size	0.2μm	0.005μm
Typical data collection time	10min	5min
Spectral artifacts	Rare	Major ones are:
		Escape peaks
		Pulse pileup
		Peak overlap
Energy for electron-hole pair creation	28eV	3.8eV

Transition	Energy (keV)	Photons / Decay Campbell(1975)	Cohen(1980)	IAEA* (1985)
NpM(total)	3.3		0.0543±0.0032	0.0635
NpM(αβγ)	3.35		0.049±0.003	
L_1L_3	4.82		0.0017±0.0005	
Ll	11.89	0.0086±0.0008	0.0087±0.0003	0.0085
$L\alpha$	13.94	0.132±0.003	0.132±0.003	0.13
$L\eta$	15.87		0.0038±0.002	
$L\beta$	17.8	0.1925±0.006	0.194±0.004	0.193
$L\gamma$	20.8	0.0485±0.002	0.0496±0.002	0.0493
γ	26.345	0.024±0.001	0.0236±0.001	0.024
γ	33.119		0.0014±0.0001	0.00103
γ	43.463		0.00057±0.00018	0.00057
γ	59.537	0.359±0.006	0.355±0.009	0.357

* W. Bambynek, IAEA Technical Document, 335(1985)412.